

NORTHWESTERN UNIVERSITY

Self Assembly and Many-Body Effects at Surfaces of Biomedical  
Relevance

A DISSERTATION

SUBMITTED TO THE GRADUATE SCHOOL  
IN PARTIAL FULFILLMENT OF THE REQUIREMENTS

for the degree

DOCTOR OF PHILOSOPHY

Field of Materials Science and Engineering

By

Bernard M. Beckerman

EVANSTON, ILLINOIS

December 2016

© Copyright by Bernard M. Beckerman 2016

All Rights Reserved

## ABSTRACT

Self Assembly and Many-Body Effects at Surfaces of Biomedical Relevance

Bernard M. Beckerman

I present research in systems of biomedical relevance consisting of agents near or comprising surfaces using computational approaches. The research topics include formation of bacterial biofilms, behavior of charged species near stacked, like-charged lamellae, and the the conformational behavior of lamellae with strong self-attraction.

In chapter 2, I present agent-based simulations and experimental analysis of bacterial surface colonization behavior. Results show that the bacterial population exhibits polyphenic motility despite being genetically homogeneous, and that the deposition of a polysaccharide causes the emergence of distinct bacterial subpopulations that specialize separately in microcolony nucleation and surface exploration.

Chapter 3 considers aggregation behavior on a much smaller length scale, wherein an attraction between like-charged cellular lamellae is mediated by the antiviral molecule squalamine. Free-energy calculations along with structural analysis of the resulting compounds reveals that the squalamine molecules form bridging configurations that are

highly effective at condensing membranes, and that the strength of this condensation is sufficient to eject the viral protein Rac1 from the lamellae.

In chapter 4, I explore the ability of such condensed, charged lamellae to selectively exclude ions as a means to control ionic current. Simulations and theory of ion-selective graphene-oxide paper in series with a bulk salt solution under an applied field show how this exclusion leads to a nonlinear current–voltage relationship. Additionally, geometrical asymmetries are introduced into the system to achieve ionic current rectification.

Chapter 5 studies the behavior of dilute graphene oxide sheets in poor solvent. In such a case, the conformations taken by the sheet are determined by a competition between its intrinsic bending rigidity and effective self-attraction. I show how self-attraction of a finite range and sufficient strength can overcome bending energy barriers of  $\sim 100k_{\text{B}}T$  to allow sheets to spontaneously condense in solution.

## Acknowledgements

First and foremost I would like to thank my advisor, Prof. Erik Lijten, for the many opportunities he has provided me, for his continued mentorship, and for his enduring support. I am also thankful to my dissertation committee, Prof. John Marko, Prof. Monica Olvera de la Cruz, and Prof. Kenneth Shull, for being generous with their help and guidance throughout the course of my PhD.

This research would not have been possible without my hard-working, passionate, and inventive collaborators, Prof. Gerard Wong, Prof. Kun Zhao, Prof. Jiaxing Huang, Prof. Kalyan Raidongia, Andrew Koltonow, Dr. Jun Gao, and Dr. Niels Boon, who always brought valuable insight and invariably elevated the quality of my work.

Heartfelt thanks to those I spent by far the most time with throughout my tenure as a graduate student, my wonderful, supportive and hardworking labmates Daniel Sinkovits, Wei Qu, Jonathan Whitmer, Moses Bloom, Kipton Barros, Ming Han, Huanxin Wu, Zonghui Wei, Amir Maghsoodi, Ziwei Wang, and Amelia Plunk. It often felt that you were the only ones in the world I could approach with certain research problems (and often that was true!), and you were always helpful when I needed it. I have learned and changed so much in your presence and with your support. To those who came before me, thank you for paving a trail of success for me to follow and for being there to guide me, and to those who have yet to graduate, I know you have the intellectual, emotional, and spiritual capacity to be successful in anything you do.

Also, I would like to thank the immense graduate-student support system that has been built over the years here at Northwestern. Particular thanks goes out to Penelope Warren, Dr. Wei-Zen Huang and Dean Dwight McBride.

Lastly, it cannot be overstated how instrumental my family and friends were during this process. My parents provided a lifetime of motivation, pride and practical support, my siblings provided immense emotional support, and my friends were always available to listen to my troubles and to help me plan logistically. Special thanks goes to my girlfriend Hadallia who literally kept me alive through the last few months of my PhD, cooking meals for me and encouraging me to sleep when it felt like I had time for neither. I can't thank you all enough for your strength through this process and for giving me a reason to keep pushing no matter what. Your love and support is the reason I am here.

## **Dedication**

To my family

## Table of Contents

ABSTRACT	3
Acknowledgements	5
Dedication	7
List of Figures	11
Chapter 1. Introduction	14
Chapter 2. Positive feedback via haptotaxis in biofilm nucleation of <i>Pseudomonas aeruginosa</i>	19
2.1. Introduction	20
2.2. Materials and Methods	21
2.2.1. Experimental methods	21
2.2.2. Simulation methods	23
2.3. Results and Discussion	30
2.3.1. Persistent step sizes	30
2.3.2. Effect of step-size persistence on the visit histogram	33
2.3.3. Emergence of distinct subpopulations	35
2.3.4. Surface coverage of nucleators and explorers	39
2.4. Conclusion	45

Chapter 3. Antiviral activity of squalamine: Role of electrostatic membrane binding	48
3.1. Introduction	48
3.2. Methods	51
3.2.1. Coarse-graining	52
3.2.2. Bead interactions	54
3.2.3. Simulation setup	55
3.2.4. Pressure calculation and barostatting	56
3.2.5. Chemical potential calculation	56
3.2.6. Thermodynamic integration	58
3.2.7. Finite-size effects	62
3.3. Results and Discussion	63
3.3.1. Membrane condensation behavior of squalamine	63
3.3.2. Membrane condensation in the presence of bulk salt	66
3.3.3. Competition between Rac1 and squalamine	71
3.4. Conclusion	73
Chapter 4. Ionic current rectification in asymmetric graphene oxide nanochannel networks	74
4.1. Introduction	75
4.2. Results and Discussion	77
4.2.1. Theory	79
4.2.2. Simulation	86
4.2.3. Conclusion	93
4.3. Simulation methodology	95

	10
Appendix	97
Chapter 5. Conformational behavior of self-attractive sheets with large bending rigidity	100
5.1. Introduction	101
5.2. Methods	103
5.2.1. Simulation Model	103
5.2.2. Metadynamics	105
5.3. Results and Discussion	108
5.3.1. Effect of self-attraction on the kinetic barrier to collapse	108
5.3.2. Energy barriers to folding	110
5.3.3. Dynamics of sheet collapse	113
5.4. Conclusion	118
Appendix A: Choice of angle potential	119
Appendix B: Calculation of folding energy barrier for a sheet	123
Chapter 6. Conclusion	129
References	133

## List of Figures

2.1	Experimental data and fits used in calibration of bacterial simulations.	22
2.2	Persistent bacterial motilities and the resulting impact on the visit distribution.	32
2.3	Mean-squared displacements of bacteria as a function of Psl deposition rate.	36
2.4	Average step sizes of clustered bacteria and their spatial distribution according to step size.	38
2.5	Bacterial cluster size as a function of Psl deposition in simulation and experiment.	41
2.6	Surface exploration of bacteria as a function of Psl deposition rate.	42
2.7	Cluster diversity as a function of Psl deposition rate.	44
2.8	Radial and angular distribution functions of simulated bacterial populations.	46
3.1	Experimental and simulation results showing the ability of squalamine to displace Rac1 molecules.	50
3.2	Simulation setup and thermodynamic integration pathway.	52
3.3	Estimated Widom weight and relative error vs. number of insertions.	59

		12
3.4	Finite-size effects in simulated systems containing Rac1, squalamine, salt, and lipid bilayers.	63
3.5	Condensation of lipid bilayer membrane stacks around charged species in the absence of salt.	65
3.6	Condensation simulations employing a modified squalamine bead size.	66
3.7	Condensation of lipid bilayer membrane stacks around charged species in equilibrium with a bulk salt solution.	69
3.8	Bistability of constant-pressure simulations.	70
4.1	Illustration of the dependency of the ion concentration profile on the ion current.	78
4.2	Simulation setup and results for a rectangular Graphene Oxide Nanochannel Network.	87
4.3	Ratio of anion leakage current as a function of applied bias in a symmetric graphene oxide nanochannel network.	89
4.4	Simulation setup and results for a trapezoidal graphene oxide nanochannel network.	91
4.5	Simulation setup and results for a trapezoidal Nanochannel Network designed for optimal rectification ratios.	93
5.1	Setup of coarse-grained Graphene Oxide simulations.	103
5.2	Radial dependence of the coordination number $C$ .	107

5.3	Simplified model of spontaneous collapse of a self-attractive sheet with bending rigidity.	109
5.4	Free-energy map from metadynamics simulations and representative configurations.	112
5.5	Free-energy maps of highly attractive sheets from metadynamics simulations.	114
5.6	Waiting time before sheet collapse as a function of self-attraction.	115
5.7	Conformations of spontaneously collapsed self-attractive sheets.	117
5.8	Comparison of Normal–Normal bending energy to that of a continuum sheet.	120
5.9	Comparison of Cosine–Delta bending energy with that of a continuum sheet.	122
5.10	Schematics for the sheet–hinge bending calculation in Appendix 5.4.	124
5.11	Comparison between a simulated sheet–hinge system and analytical calculations.	127

## CHAPTER 1

**Introduction**

Soft condensed matter concerns systems of many interacting particles whose configurations are easily deformed, e.g., by thermal forces. This class of materials encompasses a wide array of essential goods including plastics, rubbers, gels, and creams, and is fundamentally important in explaining many biological phenomena. In these soft-matter systems, particles move in response to their environment, and their motion then influences the environments of all other particles leading to complicated many-body behavior. The complexity that results can yield a system whose behavior is unintuitively different from that of its parts, and is difficult to describe theoretically.

This is especially true for nanoscale systems in aqueous environments, in which interactions are often on the order of the thermal energy  $k_B T$ , and Brownian effects keep the system in constant motion. This motion is crucial for biological systems, as it allows proteins to fold and unfold, molecules to diffusively search for binding sites, and lipids to spontaneously assemble into cell membranes. However, it poses significant barriers to observation and understanding. Visualizing these systems can be difficult due to the constant motion of the species involved and the fact that they are often smaller than the wavelength of light. Additionally, theoretical calculations are difficult for such systems that are simultaneously small enough that continuum approximations are inadequate and complex enough that a detailed theory becomes highly nonlinear and is often intractable.

This is especially true in systems that exhibit significant coupling between individual particles. For instance, electrostatic correlations can lead to non-trivial phenomena such as like-charge attraction and many-body effects.

The desire to predict the behavior of such systems has driven theoretical work for many decades. If the component parts of a system interact with many neighbors either due to the system having high dimensionality or due to weak, long-range interactions, the system can be described by a mean-field theory, in which each particle interacts with a background that corresponds to the ensemble-averaged behavior [1]. On the other hand, if the system is dominated by very strong interactions among very few neighbors, a strong-coupling theory that disregards the many-body nature of the system can be successful [2]. For intermediate interaction strengths, correlations of fluctuations around the mean behavior preclude the use of mean-field theory, and many-body effects preclude the use of strong-coupling theory, so that particle-based simulations are a useful tool to understand system behavior.

In particle-based simulations, knowledge of particle interactions is exploited to evolve a system through a series of configurations, and information is extracted from these configurations via statistical sampling. Systems are commonly evolved either using molecular dynamics (MD), which moves a system forward in time using Newton's equations of motion, or Monte Carlo (MC), which continually proposes random changes in a system that are accepted or rejected based on their energetic cost. Both techniques have advantages. MD faithfully captures dynamical behavior and so can be useful for out-of-equilibrium systems, whereas MC can generate physically realistic configurations from unphysical particle rearrangements, leading to an increase in computational efficiency.

Intuitively, one might think that modeling a system in full atomistic detail would provide the most accurate description of its behavior. In reality, such a model incurs significant computational cost and imposes severe restrictions on the length and time scales accessible to study. Furthermore, it is often a challenge to distill salient observables from the large amount of detailed information provided by such simulations to yield useful conclusions. As an alternative to a fully detailed model, the system of interest can be coarse-grained such that individual atoms are grouped into sites that interact with one another through effective potentials. This allows a significant increase in both the length and time scales accessible at a given computational cost, and offers an efficient method to model experimentally relevant systems. Furthermore, in forming such a coarse-grained model one automatically incorporates various physical assumptions so that the simulation results provide a powerful method to test and interpret those assumptions, and to thereby understand what truly drives the system of interest.

This thesis addresses the behavior of several systems of biomedical relevance containing many interacting particles that comprise or are near 2-dimensional surfaces. Each system is coarse-grained at the length scale of interest, and particle- or agent-based simulations are used to gain insight into the system behavior, thereby informing theory and experiments. In the second chapter, we consider the formation of surface-bound bacterial colonies that simultaneously explore a surface and deposit a polysaccharide that affects future bacterial motion. Agent-based bacterial modeling and extensive analysis of experimental data illustrate how this polysaccharide mediates an effective attraction between bacteria, thereby correlating bacterial positions and leading to microcolony formation.

This is an essential step in biofilm growth and one that had not been understood previously. Particle correlations are also important for condensation in biological systems at much smaller length scales. In the third chapter, we consider the condensation of the antiviral drug squalamine onto charged surfaces, and the ability of squalamine to mediate like-charged attraction between cellular membranes due to correlations that arise from the valency and internal structure of the squalamine molecule. Specifically, this chapter elucidates how squalamine can condense membranes favorably enough to eject proteins of viral origin from the condensed bilayer stacks despite the protein having higher valency. Since these proteins assist the viral replication cycle, this activity is thought to confer a degree of antiviral immunity on the cell. Such competitive exclusion of ions from charged multi-lamellar structures, either due to size exclusion or due to the large Donnan potential inside the charged layers, can lead to interesting conductance effects in the presence of an electric field applied parallel to the surfaces. Chapter four elucidates how this ion-selectivity can be exploited to manipulate ionic current through condensed, charged layers of graphene oxide (GO). We show that devices made from such materials can serve as effective, low-cost ionic rectifiers that can function on widely varying length scales. While stacking of GO sheets is common in a poor solvent when the concentration is high enough, it is unclear whether sheets in the dilute limit can similarly reduce their solvent-accessible surface area by assuming condensed or crumpled conformations. In chapter five we explore how the intrinsic bending rigidity and effective self-attraction of thin, tethered materials such as GO compete to determine the sheet conformation. We show how, even when the bending energy of folding is  $\sim 100k_{\text{B}}T$ , as it is for GO, this

can be overcome by the finite-range self-attraction of the sheet, and that given sufficient self-attraction, a sheet of any bending modulus can collapse.

## CHAPTER 2

**Positive feedback via haptotaxis in biofilm nucleation of  
*Pseudomonas aeruginosa***

## ABSTRACT

Recent work has indicated that upon adhesion to a surface *Pseudomonas aeruginosa* tend to self-organize into microcolonies, using a positive-feedback mechanism mediated by haptotactic attraction to the exopolysaccharide Psl that they secrete. We elucidate this colony-nucleation process and explore how it is influenced by bacterial motility. A detailed analysis of the data presented in our earlier study, in combination with additional simulations, provides further insight into the exploratory strategy of *Pseudomonas aeruginosa*. Specifically, we find that the isogenic bacterial population exhibits polyphenic motility and, when depositing Psl, splits into two distinct populations—those that become trapped in their self-deposited Psl and those that move sufficiently quickly to escape their Psl beds and explore the surface. We perform computer simulations in which we adjust the relative prevalence of these subpopulations by varying the Psl deposition rate and find that there is a trade-off between surface exploration, microcolony diversity, and microcolony fortification.

## 2.1. Introduction

The survival of many organisms is dependent on their ability to navigate in response to their environment, e.g., toward areas of high nutrient density or low toxicity. Organisms commonly execute such motion by sensing and responding to chemical gradients, *chemotaxis*, or by moving along gradients of surface adhesion, *haptotaxis*. These behaviors play a crucial role in the survival, development, and organization of cellular populations ranging from bacteria to tissues in multicellular organisms [3, 4, 5, 6].

Among these, *P. aeruginosa* serves as a model organism for the study of bacterial biofilms that have significant medical and industrial impacts [7]. Moreover, *P. aeruginosa* is a cause of lethal nosocomial and opportunistic infections, including those in cystic fibrosis patients, and thus is important to understand on its own [8].

*P. aeruginosa* adheres to surfaces using type-IV pili (TFP) [9]. TFP adhesion to a bare surface is often weak, and the wild-type (WT) strain PAO1 deposits the exopolysaccharide Psl to strengthen TFP surface binding [10, 11]. Additionally, bacteria use TFP to crawl across the surface [9]. Since TFP bind more strongly to surfaces coated with Psl, bacteria are attracted to sites that have received Psl from previous bacterial visits. This type of motion, in which the attractant is produced by the organism itself, “auto-attraction,” has been shown to result in spatial pattern formation [4, 12, 13, 14, 15]. For *P. aeruginosa*, the interplay between positive feedback and surface motility results in a hierarchical distribution of site visits, ultimately inducing the nucleation of microcolonies that grow into bacterial biofilms [16].

Whereas experiments and simulations have shown that microcolony size and diversity depend on the rate at which bacteria deposit Psl [16], this dependence is neither well quantified nor mechanistically understood. Here we extend the experiments and simulations from Ref. [16] and show that the Psl deposition rate controls the relative prevalence of bacterial subpopulations distinguished by their surface motilities. This relative prevalence in turn determines a trade-off during biofilm development between surface exploration, microcolony diversity, and microcolony fortification.

## 2.2. Materials and Methods

### 2.2.1. Experimental methods

A comprehensive discussion of the experimental methods is available in Ref. [16] and its supplementary information. Here we recount them in brief for context. *P. aeruginosa* are seeded into a flow cell filled with nutrified solution and precipitate onto a glass substrate. Images of the surface are taken every  $\Delta t = 3$  seconds through a  $67 \times 67 \mu\text{m}^2$ , 1-megapixel viewing window, and the positions and orientations of all bacteria are recorded using a particle-tracking algorithm in the style of Ref. [17]. The spatial distribution of bacteria is monitored by registering, for each experimental frame, a “visit” in each pixel that contains a bacterium’s center. Visits are counted starting with the onset of exponential growth (see Fig. 2.1A, the visit history before this represents  $<10\%$  of the total visit history) and ending once 500,000 visits are recorded (roughly 7 hours). Pixels are then histogrammed by the number of visits they have received (the “visit histogram”).

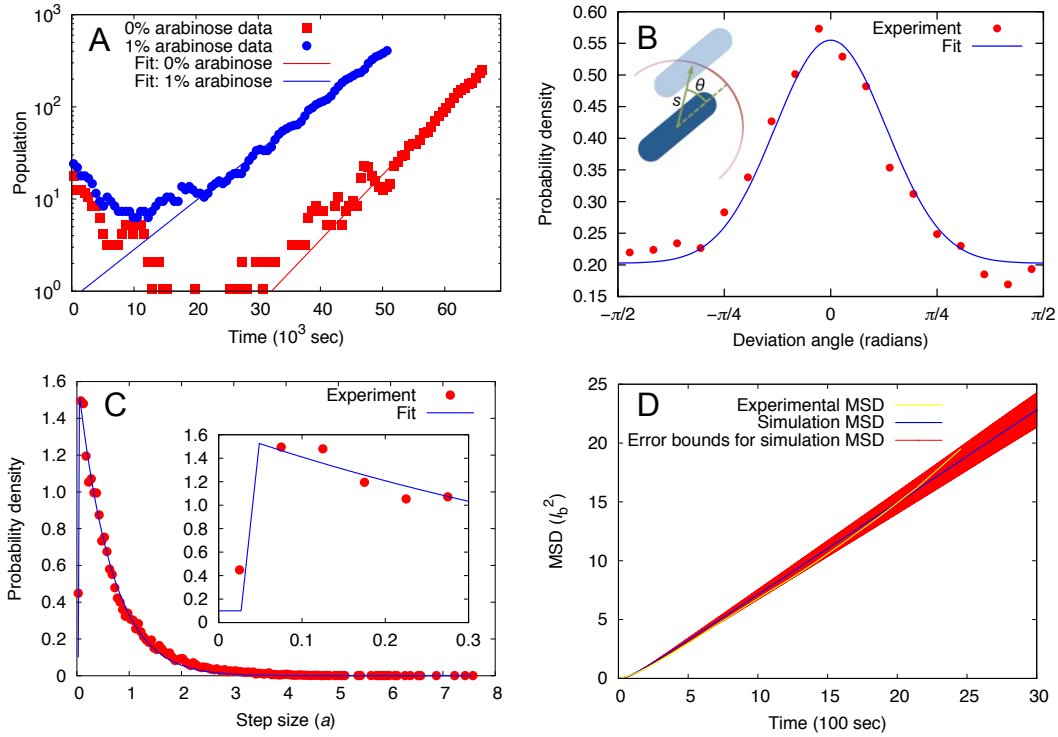


Figure 2.1. A) Experimental surface population size as a function of time, along with fitted growth rate for 0% and 1% (w/v) arabinose concentration. B) Experimentally observed deviation-angle distribution for  $\Delta P_{\text{Psl}}/P_{\text{BAD-Psl}}$  in the absence of Psl along with the fitted distribution  $P_{\text{angle}}(\theta)$  employed in the simulations. Inset shows schematic of a bacterium moving from its old position (dark spherocylinder) to a new position (light spherocylinder) over one time step. Figure is only schematic; notably, the typical step size  $s$  is only a fraction of the bacterial length  $l_b$ , see Fig. 2.1C, and the bacteria in simulation are represented by line segments instead of spherocylinders. C) Experimental step-size distribution for  $\Delta P_{\text{Psl}}/P_{\text{BAD-Psl}}$  in the absence of Psl, along with the fitted distribution  $P_{\text{step}}(s)$  employed in the simulations. Units are mesh size  $a = l_b/29$ . The inset shows the piecewise continuous nature of the assumed distribution for small step sizes. D) Bacterial mean square displacement and corresponding simulation results in the absence of Psl.

To determine the importance of Psl in mediating the distribution of surface-site visits, we use the arabinose-inducible mutant  $\Delta P_{\text{Psl}}/P_{\text{BAD-Psl}}$  [10], whose Psl production increases with the ambient concentration of arabinose in solution. This allows tuning of the

Psl deposition rate and thus of the strength of the positive-feedback mechanism, which in turn affects the aggregation behavior of the bacteria.

### 2.2.2. Simulation methods

To test the hypothesis that variations in Psl production affect the aggregation behavior observed in experiment, we employ a model in which surface-mobile agents deposit and respond to non-diffusing trails of Psl. An analytical treatment of this system is complex since the agents do not merely have instantaneous pairwise interactions but also are influenced by the motion history of all entities. To tackle this complexity, we devise a model in which bacteria move according to the *unbiased* bacterial motion observed experimentally in the absence of Psl. We then extend this model via Psl deposition, recording the deposited Psl at each surface location as the simulation progresses. The bacterial motion is then biased by the local Psl concentration. As bacteria traverse the surface, visits are collected and histogrammed as in experiment to allow a direct comparison. For each choice of parameters, results are obtained as averages over 100 independent runs, unless noted otherwise. Simulations take between 1.5 and 40 minutes per run, depending on the Psl deposition rate.

#### 2.2.2.1. Model and bacterial motion.

*System geometry and initial conditions.* We model the bacterial system using non-overlapping line segments of unit length that move across a square periodic domain of side length  $L = 35$ , which, given the mean experimental bacterium length  $l_b = 1.9 \mu\text{m}$  [16], is similar to the experimental viewing window. The no-overlap condition is imposed to avoid unrealistic dynamics, whereas ignoring excluded volume is reasonable given that the

bacteria cover less than 10% of the surface throughout all experiments. The simulations start with 10 bacteria on the surface in a random, non-overlapping configuration and advance in a series of time steps during which each bacterium can move, multiply, and deposit Psl. The run length is determined by the total visit number, which is set to 500,000 in accordance with the experiments. Due to the stochastic population growth, this corresponds to  $8300 \pm 800$  time steps per run. Each time step represents one experimental frame, so that a simulation represents approximately 7 hours, equal to the duration of the exponential growth phase in the experiments.

To avoid artifacts resulting from moving the bacteria in a set order, their selection is randomized. In Ref. [16] any of the  $n$  bacteria were selected at random and the time was incremented by  $\Delta t$  after  $n$  such selections. This, however, results in a significant fraction of bacteria ( $1/e$  for large  $n$ ) being skipped on a given time step. For those bacteria, a spurious additional visit is recorded in the pixel that they currently occupy, which reduces the number of single-visit pixels. To eliminate this artifact, all bacteria are selected once in each time step then their order is shuffled.

*Bacterial motion.* We start by modeling bacterial motion in the absence of Psl. Experimental bacterial displacements lie within a wedge emanating from the bacterium's current position [18]. In our model, bacteria move with step size  $s$  at an angle  $\theta$  from the cell's body axis (see Fig. 2.1B, inset), while maintaining director orientation. These parameters are reselected for each bacterial move from the distributions  $P_{\text{angle}}(\theta)$  (Fig. 2.1B) and  $P_{\text{step}}(s)$  (Fig. 2.1C). Since bacteria are observed to exhibit heterogeneous motility, we also consider a model in which  $s$  is selected once per bacterium and persists for the duration of the simulation (see Sec. 2.3.1).  $P_{\text{step}}(s)$  and  $P_{\text{angle}}(\theta)$  are obtained by monitoring

arabinose-inducible bacteria in the absence of arabinose and fitting functional forms to the measured histograms of  $s$  and  $\theta$ . Because the leading and trailing poles of the bacteria cannot be reliably distinguished in experiment, the pole closest to the direction of motion is taken as the leading pole. Thus, no backward moves are observed and  $P_{\text{angle}}(\theta) = 0$  for  $|\theta| > \pi/2$  both in the experimental histogram and in the fit used in simulation. For  $|\theta| < \pi/2$   $P_{\text{angle}}(\theta) = 0.202 + 0.352 \exp[-\theta^2/2\sigma^2]$ , where  $\sigma = 0.411$  radians (Fig. 2.1B). For  $P_{\text{step}}(s \geq 0.05)$ ,  $s$  in units of the pixel width  $a = l_b/29$ , the fit is a truncated Gaussian,  $P_{\text{step}}(s) = 3525 \times \exp[-(s + 10.0)^2/(2 \times (2.56)^2)]$  (in Ref. [16], Supplementary Figure 13, this expression contains an error and should read as the preceding). Since continuation of this function to  $s = 0$  overestimates the number of bacteria with very small step sizes, we model the distribution for  $0 \leq s < 0.05$  in a piecewise fashion,  $P_{\text{step}}(s) = 0.1$  for  $0 \leq s < 0.027$  and  $P_{\text{step}}(s) = 65.2s - 1.66$  for  $0.027 \leq s < 0.05$ . In this manner,  $P_{\text{step}}(s)$  is continuous and yields the same probability of a displacement in  $[0, 0.05)$  as the left-most bin in the experimental distribution (Fig. 2.1C).

The particle-tracking algorithm used in experiment is subject to errors on the order of  $\pm a$ , resulting in artificially large skips between time steps. To suppress the resulting error, bacterial trajectories are smoothed using a Savitzky–Golay filter [19] of degree 3, 5 left frames and 5 right frames, prior to accumulation of the histograms shown in Figs. 2.1B and 2.1C.

When crawling across the surface, bacteria reorient both gradually and via *tumbles* that are characterized by random body-axis rotations with zero displacement [20, 21]. Tumble-type reorientations alone are sufficient to recreate the observed random-walk behavior in the absence of Psl. For this reason and for the sake of simplicity, gradual

reorientations are omitted from the model. Since we set the tumbling rate by requiring the simulated mean square displacement (MSD) match that in experiment (see next paragraph), this rate is overestimated. As a result, simulated bacterial trajectories appear more angular than in experiment, although the long-time surface exploration behavior is thought to be adequately reproduced.

We determine the probability  $p_{\text{reorient}}$  of a reorientation by adjusting its value such that the MSD in simulation matches the experimental MSD, yielding  $p_{\text{reorient}} = 0.037$  (Fig. 2.1D). Here, the simulation MSD is obtained from 100 independent simulations of 10 bacteria monitored for  $10^5$  time steps each, and the experimental MSD is obtained by monitoring a population of arabinose-inducible bacteria at 0% w/v arabinose for more than 18 hours for a total of 520,433 bacterium-time steps. The joint probability of making a move with displacement  $\Delta\mathbf{r}$  and change of director  $\phi$  in the absence of Psl is referred to as  $P_0(\Delta\mathbf{r}, \phi)$ .

*Psl deposition and sensing.* To model the adjustable Psl deposition rate  $r_{\text{Psl}}$  of the  $\Delta P_{\text{Psl}}/P_{\text{BAD-Psl}}$  mutant, we start each bacterial move with the deposition of an amount of Psl  $r_{\text{Psl}}$ . Ref. [16] shows an approximately linear proportionality between visit frequency and Psl density maps, supporting the assumption that the deposition rate is constant over time. Accordingly,  $r_{\text{Psl}}$  is specified at the beginning of each simulation (and identical for all bacteria) and does not change. The deposited Psl is recorded in a grid cell (mesh size  $a$ , corresponding to the pixel size) containing the center of the bacterium. Experiments at variable arabinose concentrations are modeled in simulation by varying  $r_{\text{Psl}}$  from 0 up to  $10^{-3}$ , for which the histograms nearly reach their saturated form (see Fig. 2h of Ref. [16]).

Since neither  $r_{\text{Psl}}$  nor the bacterium–Psl coupling strength are known experimentally, we set the latter to 1 so that  $r_{\text{Psl}}$  is quoted in units of inverse coupling strength.

To model bacterial haptotaxis we multiply the unbiased motion  $P_0(\Delta\mathbf{r}, \phi)$  by a Psl-dependent factor

$$(2.1) \quad P_{\text{Psl}}(c_{\text{Psl}}(\mathbf{r})) \propto 1 - \exp[-(c_{\text{Psl}}(\mathbf{r}) + c_0)] ,$$

which depends on the amount of Psl  $c_{\text{Psl}}$  at the position  $\mathbf{r}$  of the leading pole of the bacterium after a translation  $\Delta\mathbf{r}$  or rotation  $\phi$ . The offset  $c_0 > 0$  is included to allow moves to regions free of Psl. Equation 2.1 was proposed in Ref. [16] and is conceptually similar to the response functional in Sec. 5 of Ref. [22], which also exhibits a saturating influence of local attractant density on bacterial motion. To reflect the ability of bacteria to sense Psl over a finite domain,  $c_{\text{Psl}}$  is the cumulatively deposited Psl in a domain centered around  $\mathbf{r}$ . For computational efficiency, we choose this as a square oriented with its sides parallel to the Cartesian axes,

$$(2.2) \quad c_{\text{Psl}} = \sum_{k=i-w}^{i+w} \sum_{l=j-w}^{j+w} \rho_{\text{Psl}}(k, l) ,$$

where  $(i, j)$  denotes the grid point containing  $\mathbf{r}$ ,  $\rho_{\text{Psl}}(k, l)$  is the amount of Psl previously deposited in cell  $(k, l)$ , and the width of the domain is  $2w+1$ . Assuming that the bacterium width ( $0.6 \mu\text{m}$ ) is representative of the size of the domain, we choose  $w = 4$ , or a domain of  $9 \times 9$  pixels. The shape of the sensor is somewhat arbitrary, however tests with a circular sensor region show no effect on the visit distribution (data not shown).

The amount of Psl deposited is  $\rho_{\text{Psl}}(k, l) = r_{\text{Psl}}n_{\text{vis}}(k, l)$ , where  $n_{\text{vis}}(k, l)$  is the total number of prior visits to pixel  $(k, l)$ . Since the parameter  $c_0$  controls moves to Psl-devoid regions, it can be interpreted as a measure for the TFP binding-strength to bare surface. We find empirically that  $c_0 \lesssim 0.001$  ensures that the simulated systems cover the range of visit histograms observed in experiment (see Ref. [16] and Sec. 2.3 below). Since the computational cost increases with decreasing  $c_0$ , we choose  $c_0 = 0.001$ , i.e., the largest value that adequately reproduces experimental behavior.

Rather than generating bacterial moves directly according to the joint distribution  $P_0(\Delta\mathbf{r}, \phi) \times P_{\text{Psl}}(c_{\text{Psl}}(\mathbf{r}))$ , we generate trial moves according to  $P_0$  and then accept these moves according to Eq. 2.1. If a move is rejected, a new move is proposed for the same bacterium. This continues until a move is accepted or until a limiting number of attempts  $N_{\text{max}}$  is reached, to avoid deadlock situations. The error introduced by this is limited by choosing  $N_{\text{max}}$  large enough that fewer than 1% of all moves are aborted for all deposition rates. Accordingly,  $[1 - P_{\text{Psl}}(c_{\text{Psl}} = 0)]^{N_{\text{max}}} = 0.01$  or  $N_{\text{max}} \approx 4.6/c_0$  for small  $c_0$ . The excluded volume of the bacteria is modeled by rejecting proposed moves that result in bacterial overlap, resulting in a higher rate of rejection. Empirically  $N_{\text{max}} \approx 5.7/c_0$  is large enough that less than 1% of all moves are aborted for all  $r_{\text{Psl}}$ .

*Bacterial growth.* During each time step we let each bacterium divide with probability  $p_{\text{growth}}$ , chosen to match the exponential population growth rate observed in the experiment. Figure 2.1A shows the bacterial population as a function of time for the lowest and highest arabinose concentrations (0% and 1% (w/v), respectively) along with fits to the exponential part of the data (times greater than 15,000 steps for 0% arabinose and greater than 6,000 steps for 1% arabinose). The growth rates obtained from the fits

are  $4.91(9) \times 10^{-4}$  per bacterium per time step (0% arabinose) and  $3.69(4) \times 10^{-4}$  per bacterium per time step (1% arabinose). In the simulations we find that variations in the growth rate of  $\sim 20\%$  do not significantly affect the form of the visit histogram, so the average of these two rates ( $4.30 \times 10^{-4}$  per bacterium per time step) is used for all  $r_{\text{Psl}}$ . Upon division, we place a new bacterium with its long axis collinear with that of its parent, either parallel or antiparallel with equal probability, and displaced  $\pm l_b$  from the parent, with equal probability.

In Ref. [16], a growth event was rejected if it led to overlapping bacteria, effectively resulting in locally suppressed growth rates for tightly clustered bacteria. To rectify this, here we implement a scheme that successfully places a bacterium for every growth event. If a daughter cell overlaps with an existing bacterium we first attempt to place it on the opposite pole of the parent (i.e., touching the head instead of the tail, or *vice versa*). If this again results in an overlap, the new bacterium is oriented either parallel or antiparallel to the bacterium with which it first overlapped (in case there are multiple overlaps on the first placement attempt, the bacterium with the smallest center-to-center distance from the parent is chosen), and placed at the midpoint of the center-to-center line connecting this bacterium and the parent. The distance between the daughter cell and the bacterium with which it is parallel is repeatedly halved until there is no overlap. Note that this always leads to successful placement, since the model assumes the bacteria to have zero width.

*Attachment and detachment.* In the initial phases of biofilm formation, bacteria are reversibly bound to the surface and thus can attach and detach [16]. The detachment rate is anti-correlated with the Psl concentration at the surface to which it adheres [16],

and most detachment events come from bacteria that have short residence times (data not shown) and therefore little overall effect on the visit distribution and Psl content of the system. For this reason, and to maintain the simplicity of the model, we forego modeling attachment and detachment.

*Comparison to previous models.* In theoretical models of auto-attractors [22, 23], agents were found to self-localize given fast enough deposition of the auto-attractant, as in ours. An essential difference is that these models used a diffusive attractant to obtain stable aggregation over long time scales. Without diffusion, the surface eventually becomes evenly covered with a saturating concentration of auto-attractant so that no sites are favored, leading to microcolony collapse. Another important difference is that the present simulation model is precisely calibrated to our experimental system per Fig. 2.1 to allow direct comparisons.

In addition, auto-attractive systems have been studied using a set of nonlinear Fokker–Planck equations known as the Patlak–Keller–Segel model (see Refs. [24] and [25] for a detailed review). Although such a treatment matching our system parameters may be useful, it is not undertaken in the present study.

## 2.3. Results and Discussion

### 2.3.1. Persistent step sizes

The supplementary movie of Ref. [16] shows that some bacteria move faster than others, even in the absence of Psl. This is in accord with recent research that suggests that an asymmetric distribution of cellular organelles during cell division can lead to motility polyphenism in isogenic populations of *P. aeruginosa* [26]. One would expect to observe

temporal correlations in the step sizes of individual bacteria with intrinsic motilities, however these are difficult to observe because the bacterial motion is twitchy and the bacterial positions are subject to observational noise on the order of a few pixel widths. However, we can identify statistically significant differences in the average step sizes  $\langle s \rangle$  of different bacteria that correlate with residence time on the surface (Fig. 2.2A).

Before inferring meaning from this correlation, we consider potential experimental artifacts that may cause it. First, measurement of true surface residence time can be disrupted by division events. However, this does not have a significant effect on the data, as the average time for a division (more than 6000 seconds) is much longer than most residence times. Next, we can expect trends resulting from the fact that faster bacteria may traverse the image window in fewer frames. However, this would result in  $s = 1/t^x$ , where  $t$  is the traversal time, with  $x \geq 1$  ( $x > 1$  can result from random attachment/detachment), whereas Fig. 2.2A shows  $x \lesssim 1/3$ . Lastly, motility behavior characteristic of attachment or detachment would proportionally have a larger effect on bacteria with short surface residence times thereby potentially generating the observed trend. To exclude the possibility that this correlation is due to behavior characteristic of bacteria immediately after attachment or immediately before detachment, we perform the same analysis as in Fig. 2.2A but with the first and last ten time steps of a bacterium's surface residence omitted. The results are similar to Fig. 2.2A (data not shown), supporting the conclusion that the correlation between  $\langle s \rangle$  and residence time is not merely due to artifacts. Because TFP are responsible for surface adhesion as well as motility, this correlation could imply that an asymmetric distribution of pili between daughter cells causes this difference in motility, similar to the results of Ref. [26].

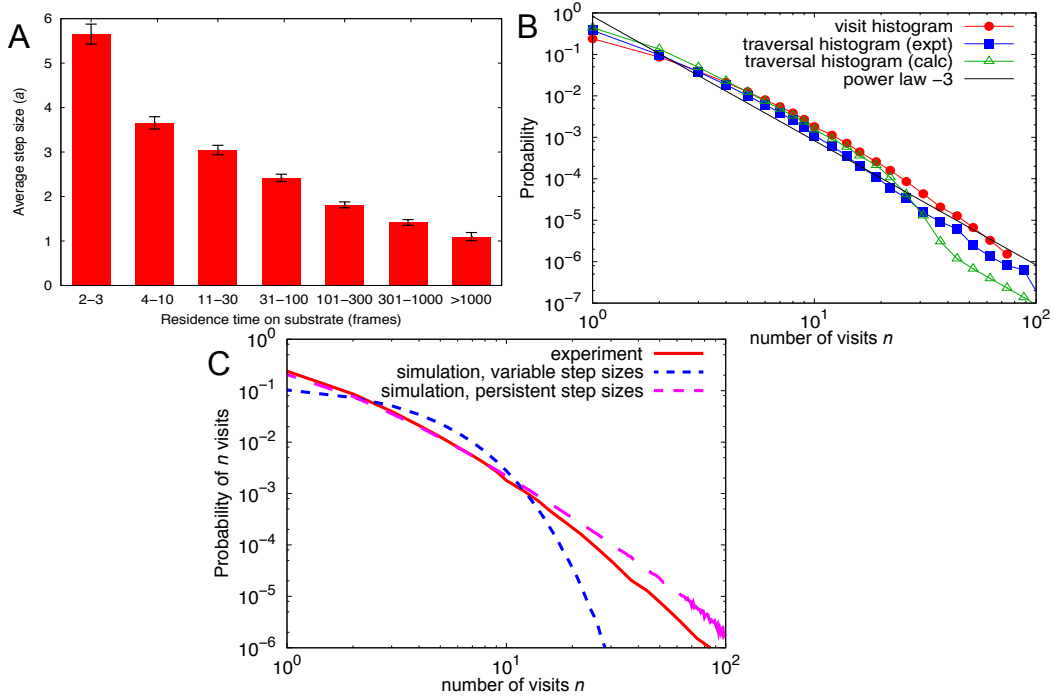


Figure 2.2. A) Average unsmoothed step size and standard deviation of the mean (in units of the mesh size  $a$ ) for the arabinose-inducible  $\Delta P_{Psl}/P_{BAD}$ - $Psl$  mutant with different residence times, in the absence of arabinose (so no Psl is deposited). Each bar represents an average over at least 1000 bacteria, except the rightmost which represents 299 bacteria. B) Visit histogram and traversal histogram from experiment, calculated traversal histogram, and power law  $-3$ . The similarity of the first two curves indicates that the visit histogram is dominated by the distribution of pixel traversal times rather than the distribution of revisited pixels. See Sec. 2.3.2 for the definition and calculation of the traversal histograms as well as a detailed comparison of the present curves. The calculated histogram agrees well with experiment, especially at low visit number. C) Visit histograms obtained in experiment and in two different simulations, all in the absence of Psl. “Variable step sizes” indicates that the step size  $s$  of each bacterium was reselected at each time step, whereas “persistent step sizes” indicates that each bacterium was assigned a fixed  $s$  at birth and retained that value for the course of the simulation. Experimental results lie between those of simulations with variable and persistent step sizes, however the latter agrees much better with experiment and captures the observed power-law behavior. This supports the conclusion that the power-law form of the visit distribution is a consequence of the persistent nature of bacterial motility (see discussion in main text).

Simply selecting the step size  $s$  from  $P_{\text{step}}(s)$  for each bacterium at each time step would result in average motility for all bacteria, disallowing the distinctive behaviors observed experimentally. To model heterogeneous motility, individual characteristics are assigned at “birth.” Because bacterial step sizes show no temporal correlation (data not shown), bacterial motion would be best represented by a distinct step-size distribution assigned to each bacterium, from which then a step size is chosen stochastically on a per time-step basis. However, since it is difficult to obtain statistical information on these individual distributions from the experiments, we approximate the individual behavior by randomly choosing  $s$  from  $P_{\text{step}}(s)$  once per bacterium and keeping it fixed for the duration of the simulation. This approximation leads to deviations at long times that manifest themselves, e.g., in the visit histogram at large visit number.

### 2.3.2. Effect of step-size persistence on the visit histogram

Bacterial surface exploration is quantified via the “visit histogram,” the probability that a pixel is visited  $n$  times (see Figs. 2.2B and 2.2C above, as well as Figs. 2d and 2e of Ref. [16]). In the absence of Psl, bacteria exhibit “exploratory” behavior, i.e., pixels are highly likely to be visited few times and highly unlikely to be visited many times. This manifests itself as a distribution of surface-site visits that can be approximated by a power law of roughly  $-3$  over roughly two decades (Fig. 2.2B).

The form of the visit histogram in simulation strongly depends on the algorithm employed for selecting the bacterial step sizes (Fig. 2.2C). Drawing the step size from the distribution  $P_{\text{step}}$  at each bacterial move results in amplified intermediate visit numbers at the expense of low and high visit numbers compared with experiment. Conversely, using

*persistent* step sizes as discussed above straightens the shoulder-type curve to a Pareto- or power-law-like curve (Fig. 2.2C). This indicates that the power-law signature may not be due to many-body behavior as claimed in Ref. [16], but instead is due to the distribution of pixel traversal times of individual bacteria.

Because the median step size  $\tilde{s}$  equals  $0.46a$ , with  $a$  the pixel size (see Fig. 2.1C), a pixel traversal typically requires multiple time steps and thus registers multiple visits to the same pixel. To quantify the resulting effect on the visit histogram, we construct a “traversal histogram”  $Q(n)$  from the experimental data, counting the number of visits per traversal, i.e., the number of visits to a pixel before that pixel is visited by a new bacterium or by a bacterium that has traveled at least  $5a$  from the pixel since its prior visit, measured radially. The latter condition is imposed to suppress spurious “revisits” that arise from inaccuracies in locating a bacterium’s center. Since the number of visits per pixel represents a sum over traversals, the difference between the traversal and the visit histogram provides a measure of collective behavior in the absence of Psl. The similarity between the two curves (Fig. 2.2B) suggests that the power-law-like behavior does not necessarily result from collective behavior as hypothesized in Ref. [16].

It is instructive to examine the effect of persistence of bacterial step sizes by computing a single-particle approximation to  $Q(n)$ . If we assume that bacteria have a persistent step size  $s$  given by the probability distribution  $P_{\text{step}}(s)$ , and traverse a path of length  $l$  through a pixel such that the number of steps  $n = l/s$ , then the traversal distribution satisfies

$$(2.3) \quad Q(n)|dn| \propto P_{\text{step}}(s)s|ds| \Rightarrow Q(n) \propto P_{\text{step}}(l/n) \frac{l^2}{n^3} .$$

The factor  $s$  on the right-hand side of the first relation reflects that faster bacteria traverse more pixels. If we assume the variation in  $P_{\text{step}}(s)$  to be small over the range considered, we find  $Q(t) \propto t^{-3}$ , matching experiment. Fig. 2.2B shows the traversal histogram computed from the step-size distribution and probability distribution of the path lengths  $l$ , matching the experiment quite well. The main deviations occur at high visit number, where the calculated traversal histogram depends on  $P_{\text{step}}(s)$  for small  $s$ , for which there is little data (see Fig. 2.1C).

### 2.3.3. Emergence of distinct subpopulations

Gibiansky *et al.* observed the division of crawling wild-type *P. aeruginosa* into super- and subdiffusive subpopulations [18]. A similar analysis of bacterial motilities with an added dependence on Psl deposition (Fig. 2.3A) shows that wild-type bacteria (moderate Psl deposition) divide into subpopulations of super- and subdiffusive bacteria [18], whereas Psl overproducers are indiscriminately slowed so that even the fastest bacterial subpopulations exhibit subdiffusive motility.

This can be understood by considering the interaction of bacteria with distinct motilities (Fig. 2.2A) with the Psl they deposit. Such bacteria can be divided into two subpopulations: those that move fast enough to escape the Psl that they deposit and those that do not. We show this in simulation by dividing the bacterial population into deciles of intrinsic step size and plotting their MSDs as a function of time (Fig. 2.3B–E). As expected, for  $r_{\text{Psl}} = 0$ , the MSDs of all bacteria are superlinear (ballistic) transitioning to linear (diffusive) on the time scale of  $1/p_{\text{reorient}}$  time steps, where  $p_{\text{reorient}} = 0.037$ . Note that this behavior differs from that of the short-time experimental MSDs because the model

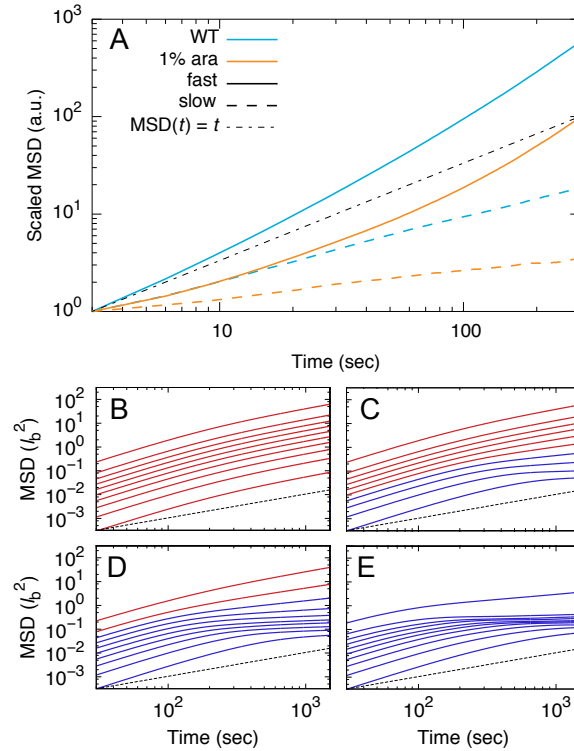


Figure 2.3. Mean-squared displacement of various subpopulations, as a function of Psl deposition rate. A) Experimental MSDs of the highest (solid) and lowest (dashed) step-size quartiles of bacteria are plotted for wild-type (blue) and Psl-overdepositing bacteria (orange). The results are normalized by their values at  $t = 3$  sec to facilitate comparison of slopes, and all bacteria with surface residence times less than 300 sec are omitted. All error bars are smaller than the line widths. B–E) Simulated bacterial MSDs are separated into deciles by intrinsic step size  $s$  for B)  $r_{\text{Psl}} = 0$ , C)  $r_{\text{Psl}} = 10^{-5}$ , D)  $r_{\text{Psl}} = 10^{-4}$ , and E)  $r_{\text{Psl}} = 10^{-3}$ . From bottom to top in each graph the dotted line represents diffusive behavior (i.e.  $\text{MSD}(t) \propto t$ ) followed by the MSDs of the step size deciles in order of increasing  $s$ . Red and blue curves correspond to diffusive and subdiffusive MSDs, respectively, for  $t > 1/p_{\text{reorient}}$ . In both experiment and simulation, moderate Psl deposition allows super- and subdiffusive groups to coexist, whereas Psl-overdeposition confers subdiffusivity on all bacterial subpopulations.

lacks gradual reorientations. As  $r_{\text{Psl}}$  increases, increasingly fast bacteria become corralled in their own Psl, indicated by sublinear MSDs, until all become corralled for  $r_{\text{Psl}} = 10^{-3}$ .

The Psl deposition rate therefore controls the relative prevalence of super- and subdiffusive bacteria and is therefore an essential parameter in determining the collective motility of the bacterial population.

We can see how distinct populations emerge over time by looking at the average of the intrinsic step sizes of all clustered bacteria  $\langle s \rangle_{\text{clust}}$ , where clusters are identified using the DBSCAN algorithm with  $MinPts = 5$  and  $Eps = 50$  pixels [27] (Fig. 2.4A). Since the intrinsic step size is unknown in experiments with Psl-depositing bacteria, we present simulation results exclusively. Clustering behavior is strongly dependent on the population density, so to suppress noise due to run-to-run variations in this density, we plot  $\langle s \rangle_{\text{clust}}$  as a function of total bacterial population instead of time. For  $r_{\text{Psl}} = 10^{-5}$ ,  $\langle s \rangle_{\text{clust}}$  is initially small compared to the average step size of the entire population and increases with time as the overall bacterial density grows and a larger fraction of bacteria join clusters, indicating that fast bacteria initially explore the surface and then join colonies. For large  $r_{\text{Psl}}$  both fast and slow bacteria join clusters indiscriminately from the beginning so that the average step size of bacteria in clusters is nearly equal to the overall average.

This effect can also be visualized by maps of bacterial speed, which is taken here as the average step size over the surface lifetime of a bacterium. To create these maps, we color-code each pixel by the speed of its slowest visitor (Figs. 2.4B and C). Recreating Fig. 2.4B using intrinsic step sizes instead of observed average step sizes produces qualitatively similar results (data not shown). Over distances smaller than a bacterium length, the shape of the bacterial trail differs between simulation and experiment due to the approximate nature of the reorientation in simulation (see Sec. 2.2.2.1) and because the simulated bacteria have zero width, allowing them to pack more closely. Despite this

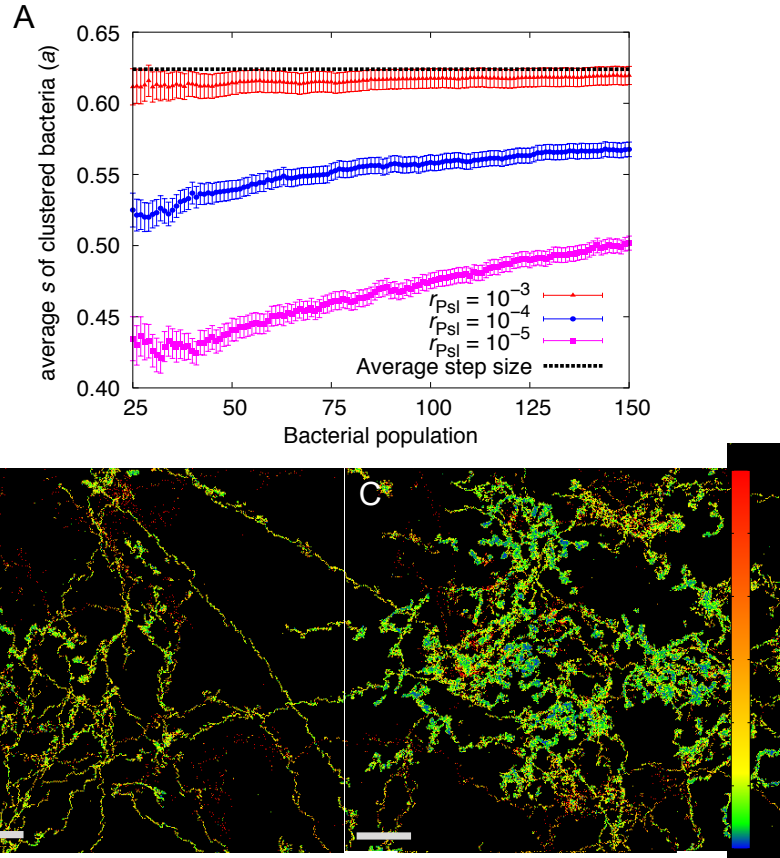


Figure 2.4. A) Average intrinsic step size  $s$  of clustered bacteria as a function of bacterial population for  $r_{\text{Psl}} = 10^{-5}$ ,  $10^{-4}$  and  $10^{-3}$ . The black dotted line at the top represents the average step size for the entire bacterial population. Bacteria at high  $r_{\text{Psl}}$  cluster more or less indiscriminately from the beginning, whereas for low  $r_{\text{Psl}}$  only the slowest bacteria cluster initially, followed by increasingly fast bacteria at later times (larger Psl content). B, C) Representative step-size maps obtained after 500,000 bacterium-time steps, in which pixels are color-coded according to the step size of their slowest visiting bacterium, from B) simulation with deposition rate  $r_{\text{Psl}} = 10^{-5}$  and C) experiment at 0.1% (w/v) arabinose. Scale bars are 2 bacterium lengths and  $4\mu\text{m}$ , respectively. Both images demonstrate the tendency of clusters to form around those bacteria with smallest step size. The differences between the images are discussed in Sec. 2.3.3.

we can see in both maps that densely visited patches have slow bacteria at their core, surrounded by a “corona” of faster bacteria. Supplementary Movie 1 shows that slow bacteria quickly become localized and start to nucleate small but rich Psl “beds” that become increasingly attractive to other bacteria. Faster bacteria don’t stay in one place long enough to initiate a Psl bed, but instead explore the entire surface, encountering the Psl beds created by other bacteria and possibly joining smaller patches together by traversing between them. For this reason we refer to the subdiffusive group as “nucleators” and the diffusive group as “explorers.”

#### 2.3.4. Surface coverage of nucleators and explorers

Since the relative proportion of nucleators and explorers can be tuned via the rate of Psl deposition in both experiment and simulation, we can evaluate how amplifying one subpopulation at the expense of the other affects salient observables in microcolony formation.

**2.3.4.1. Colony size.** An important function of a healthy biofilm is to fortify its constituent bacteria against their environment, e.g., antibiotic factors [7]. Experiments indicate that microcolony fortification is a time-consuming process during which *P. aeruginosa* colonies are vulnerable to eradication, and after which they are relatively impervious to such treatment [28]. Since Psl is a main component of the extracellular matrix [29], larger  $r_{\text{Psl}}$  can be considered to confer an advantage. Additionally, biofilms fortify themselves via changes in behavior such as reduced nutrient intake, decreased motility, and increased production of extracellular matrix, which are induced via quorum sensing when clusters

reach a certain size and density [7, 30, 31, 32]. Thus, even though we do not model quorum-induced changes, we can employ cluster size as a measure for biofilm fitness.

The average size of the largest cluster in simulation as a function of time elapsed shows a transition point around 6.5 hours and colony sizes  $\sim 100$ , below which high  $r_{\text{Psl}}$  yields larger colonies and above which the opposite is true (Fig. 2.5A). Depending on the microcolony size required to induce a change in phenotype, different deposition rates could confer an advantage here. In experiment, larger arabinose concentrations afford larger clusters over the entire range examined, although statistics limit this to below the transition point observed in simulation (Fig. 2.5B). Note that population is used as a proxy for time, because population-dependent clustering causes large variations between runs at a given elapsed time, which for the limited experimental data would lead to large error bars. For large Psl deposition rates, bacteria are less mobile and cluster growth happens mostly due to reproduction. At early times this decreased mobility aids cluster growth, but when the surface population grows large Psl deposition rates can hinder growth by preventing bacteria from joining larger clusters.

**2.3.4.2. Surface exploration.** It is useful for bacteria to explore a surface on which they land, either to forage or to find other bacteria already established on the surface [33]. The impact of Psl deposition on surface exploration can be quantified by the percentage of surface covered by at least one bacterium during a simulation or experiment (Fig. 2.6). A pixel is considered covered if it lies within 4 pixels of a visited pixel, corresponding to a bacterium half-width. Bacteria explore the majority of the surface for experimental arabinose concentrations  $< 0.1\%$ , and for simulated  $r_{\text{Psl}} \lesssim 10^{-5}$ . Additionally, the surface coverage of WT bacteria suggests that their deposition rate is less than that of the

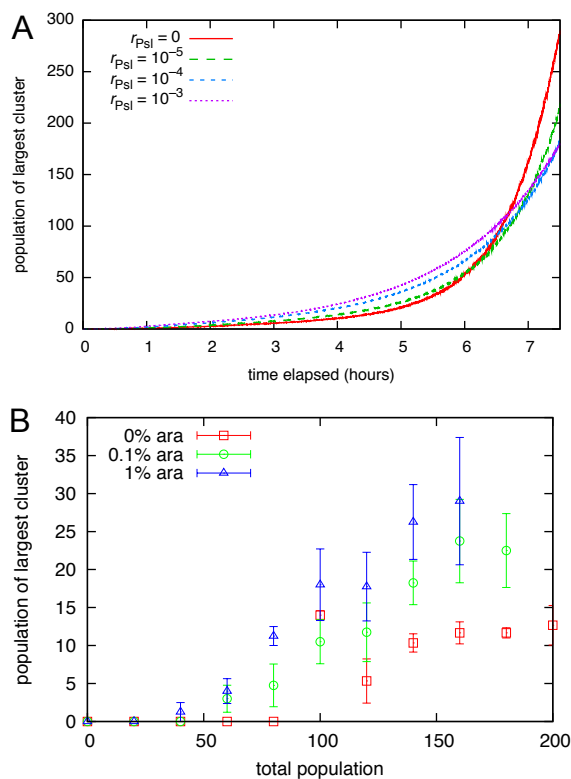


Figure 2.5. Evolution of largest cluster size in simulation and experiment, for various Psl deposition rates. A) Largest cluster size per simulation as a function of time, averaged over 1000 simulations. B) Largest cluster size per experiment as a function of total bacterial population, averaged over at least 3 experiments. At shorter times, higher Psl deposition rates promote clustering in both simulation and experiment. In addition, the simulations show that after  $\sim 6.5$  hours, higher  $r_{\text{Psl}}$  hinders clustering due to bacterial immobility. This transition is not observed in experiment, possibly due to lack of statistics.

arabinose-inducible mutant in the presence of 0.1% w/v arabinose. Large Psl deposition rates are observed to significantly impede surface exploration, indicating that the ability of a WT bacterial population to explore the majority of the surface is partly due to its limited Psl deposition.

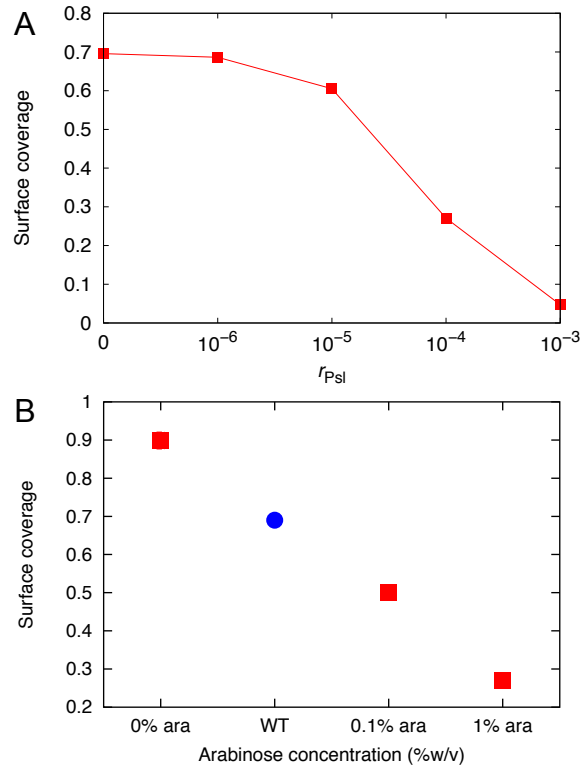


Figure 2.6. Surface exploration vs. Psl deposition. Percent of surface pixels covered in A) simulation as a function of the Psl deposition rate  $r_{\text{Psl}}$  and B) experiment as a function of the arabinose concentration, both after 500,000 bacterium-time steps. Red squares have error smaller than the symbol size. The blue circle (WT bacteria) represents a single experiment and has no error bounds, and its placement between 0% and 0.1% arabinose concentrations merely emphasizes that its behavior is consistent with an arabinose concentration between these values. Both panels show a monotonic decrease of surface exploration as a function of Psl deposition, although the coverage at 0% arabinose concentration is significantly higher than in the simulations for  $r_{\text{Psl}} = 0$ . This may be attributed to frequent attachment and detachment events not modeled in the simulations. The majority of the surface is unexplored for  $r_{\text{Psl}} \gtrsim 10^{-4}$  and for arabinose concentrations  $\gtrsim 0.1\%$ . Additionally, the WT deposition rate is low enough for the population to explore the majority of the surface.

**2.3.4.3. Diversity.** One characteristic of a healthy biofilm is microheterogeneity, the presence of genetic diversity within a cluster [34, 35]. To characterize this we track

bacterial lineage with a lineage number  $i$  ( $i = 1, \dots, 10$ ) that is passed from a parent to its offspring. For each cluster we compute the Gini–Simpson diversity index, i.e., the probability that two bacteria from the same cluster belong to different lineages,

$$(2.4) \quad G = \frac{M^2 - \sum_{i=1}^{10} n_i^2}{M(M-1)},$$

where  $M$  is the total number of bacteria in a cluster and  $n_i$  the number of bacteria from each lineage in that cluster [36].  $G$  decreases monotonically as a function of  $r_{\text{Psl}}$  (Fig. 2.7A), in accordance with the experimental results for the same system, where microcolonies of WT bacteria were found to exhibit much greater bacterial diversity than microcolonies of Psl overproducers [16]. Even though the present study involves isogenic bacteria and hence no cluster is genetically diverse, these results demonstrate that low Psl production enables bacteria to form polygenic clusters in polygenic environments, thus providing genetic diversity that can protect a cellular population in an unstable environment [35]. The similarity to Fig. 2.6A is not surprising, as bacteria that cover more ground will also mix better.

Since it is possible that the dependence of cluster size distribution on  $r_{\text{Psl}}$  affects the trend observed in Fig. 2.7A, we also consider diversity as a function of cluster size (Fig. 2.7B), separated per Psl deposition rate. Whereas there is an overall increase in diversity with cluster size, at fixed cluster size diversity decreases with increasing Psl deposition rate, consistent with Fig. 2.7A.

**2.3.4.4. Radial distribution function.** The effect of Psl can be viewed as mediating a time-delayed attraction between bacteria, resulting in positional correlations that can be observed in the center-to-center radial distribution function  $g(r)$  (RDF). Since clustering

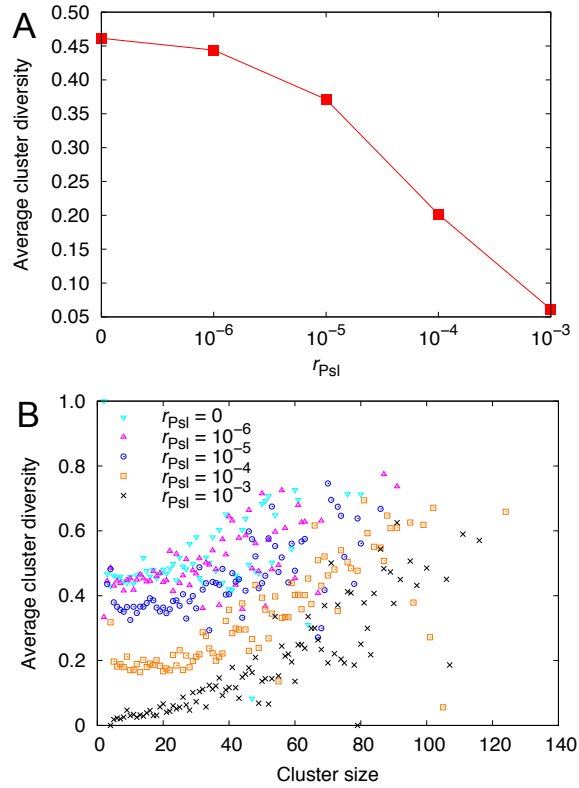


Figure 2.7. Cluster diversity and Psl deposition rate. Gini–Simpson diversity index of bacterial clusters, as a function of A) deposition rate  $r_{\text{Psl}}$  and B) cluster size for different  $r_{\text{Psl}}$ . Both graphs are taken from 100 independent simulations of 500,000 bacterium-time steps each. Large values for  $r_{\text{Psl}}$  suppress bacterial mobility, thus reducing clusters to a near-monoculture at the highest  $r_{\text{Psl}}$  examined. Diversity is also strongly dependent on cluster size (see panel B), but decreases monotonically with increasing  $r_{\text{Psl}}$  regardless of cluster size. See main text for further discussion.

can result from bacterial reproduction alone [37, 38], we isolate Psl-dependent clustering by simulating 50 non-multiplying bacteria (corresponding roughly to the time-averaged population size in experiment).

After 500,000 bacterium-time steps, the RDF (Fig. 2.8A) shows a peak for  $r < l_b$ , followed by a depletion zone near  $r \approx l_b$  that develops as the Psl deposition rate increases. To exclude the possibility that this depletion simply results from excluded-volume effects

we examine the joint radial and angular distribution function, i.e., the relative probability that two bacteria have center-to-center distance  $r$  and difference  $\alpha$  in director orientation, for  $r_{\text{Psl}} = 10^{-3}$  after 500,000 bacterium-time steps (Fig. 2.8B). Since the depletion extends beyond the excluded-volume region and is present for all  $\alpha$ , we conclude that it is driven by Psl. Whereas large  $r_{\text{Psl}}$  helps localize bacteria in tightly packed groups, the associated reduction in mobility (Fig. 2.3) prevents the formation of larger clusters, leading to the depletion minimum in Fig. 2.8A, and the crossover in Fig. 2.5A.

## 2.4. Conclusion

We have combined experiments with carefully calibrated simulations to show that Psl deposition significantly affects microcolony formation via bacterial surface motility. Experiments show that an isogenic population of *P. aeruginosa* exhibits polyphenic motility that correlates with surface residence time even in the absence of Psl, and associated simulations indicate that this polyphenism is responsible for the power-law form of the visit histograms observed in Ref. [16]. When bacteria deposit Psl, this step-size heterogeneity causes the bacterial population to split into “nucleators,” which travel slowly enough to become trapped in their own Psl beds, and “explorers,” which can escape their Psl beds and explore the surface. These distinct populations have been observed in experiment [18]. We have adjusted the relative prevalence of these subpopulations by tuning the simulated Psl deposition rate and observed that a higher prevalence of nucleators may decrease the microcolony fortification time, and a higher prevalence of explorers allows bacteria to cover more of the surface and to form clusters that are more heterogeneous

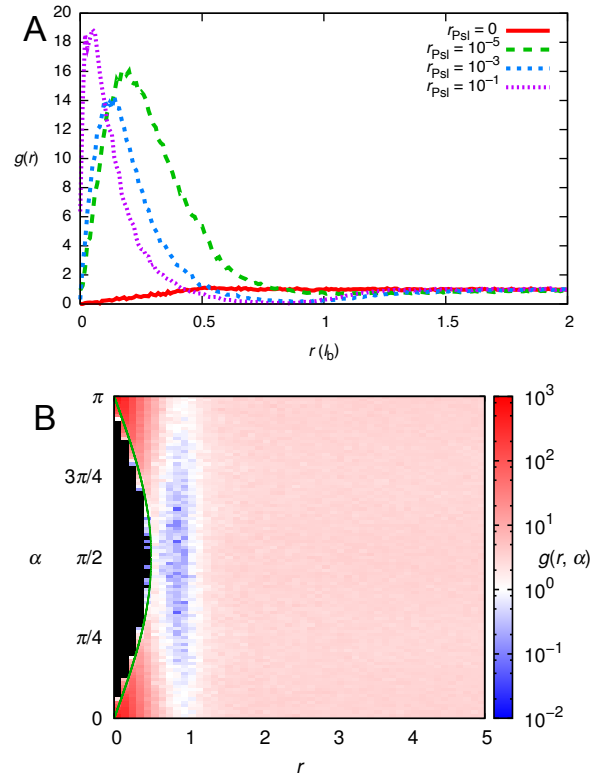


Figure 2.8. Spatial distribution of bacteria. A) Radial distribution function  $g(r)$  as a function of center-to-center distance  $r$ . B) Joint radial and angular distribution function  $g(r, \alpha)$  for  $r_{\text{Psl}} = 10^{-3}$ . The green line represents the distance of closest approach as a function of the difference  $\alpha$  in director orientation. Both graphs are obtained from 10,000 independent simulations (for each value of  $r_{\text{Psl}}$ ) of 50 non-multiplying bacteria after 500,000 bacterium-time steps.

in bacterial lineage. We find that a single deposition rate yields surface coverage, microcolony fortification, and microcolony diversity that are simultaneously all close to optimal. Interestingly, by comparing the experiments and simulations in Ref. [16] we see that the visit histogram of wild-type *P. aeruginosa* exhibits a power law close to the optimal simulations, which exhibit a large degree of heterogeneous motility. This may indicate that

the Psl deposition rate of wild-type *P. aeruginosa* is tuned to utilize their phenotypic diversity to their advantage.

## CHAPTER 3

**Antiviral activity of squalamine: Role of electrostatic  
membrane binding**

## ABSTRACT

Previous work has demonstrated that squalamine, a molecule found in the liver of sharks, exhibits broad-spectrum antiviral properties. It has been proposed that this activity results from the charge-density matching of squalamine and phospholipid membranes, causing squalamine to bind to membranes and displace proteins such as Rac1 that are crucial for the viral replication cycle. Here we investigate this hypothesis by numerical simulation of a coarse-grained model for the competition between Rac1 and squalamine in binding affinity to a flat lipid bilayer. We perform free-energy calculations to test the ability of squalamine to condense stacked bilayer membranes and thereby displace bulkier Rac1 molecules. We directly compare our findings to small-angle X-ray scattering results for the same setup and show that this coarse-grained model is sufficient to replicate the binding of membranes and exclusion of Rac1 by squalamine molecules.

**3.1. Introduction**

Squalamine, a bile salt originally derived from dogfish shark tissues, was established as an effective broad-spectrum antibiotic upon its discovery in 1993 [39, 40]. Recently, squalamine was discovered to be an effective antiviral medication as well [41]. It was

proposed this activity relates to the charge-density matching of squalamine and phospholipid membranes [41], which causes squalamine to bind to membranes and displace proteins such as Rac1 [42, 43, 44] that can be crucial for viral entry [45, 46], protein synthesis [47], virion assembly [48, 49], virion budding [50], and other steps in the viral replication cycle [51].

To test this hypothesis, small-angle X-ray scattering experiments were performed in which membrane-forming lipids of composition similar to that of membranes in mammalian cells (20:20:60 DOPS:DOPC:DOPE [52]) were incubated alone, with Rac1 only, with squalamine only, and with Rac1 and squalamine together (Fig. 3.1b) [41]. Results indicate that Rac1–membrane complexes are weakly associated lamellar stacks with a spatial periodicity broadly distributed around 29 nm, whereas squalamine–membrane complexes are tightly associated with spacing sharply distributed around 5.3 nm, which after subtracting the bilayer thickness  $d_{\text{bil}} \approx 4.5$  nm leaves 0.8 nm of separation between membranes indicating tightly formed stacks. Lipids incubated with both Rac1 and squalamine exhibit a diffraction pattern nearly identical to that of squalamine only (spacing  $\sim 5.4$  nm), indicating first that squalamine continues to bind lipid membranes into tight stacks regardless of the presence of the more highly charged Rac1 molecules, and second, since the shoulder corresponding to Rac1–lipid complexes is not present and the bilayer separation ( $\sim 0.9$  nm) is less than the minimum width of a Rac1 protein ( $\sim 4$  nm), that squalamine–lipid complexes are highly favored over Rac1–lipid complexes and that Rac1 has been ejected from the condensed bilayers.

Further testing involved coarse-grained (CG) molecular dynamics (MD) simulations in which squalamine and/or Rac1 molecules interacted with a single outer leaflet of a

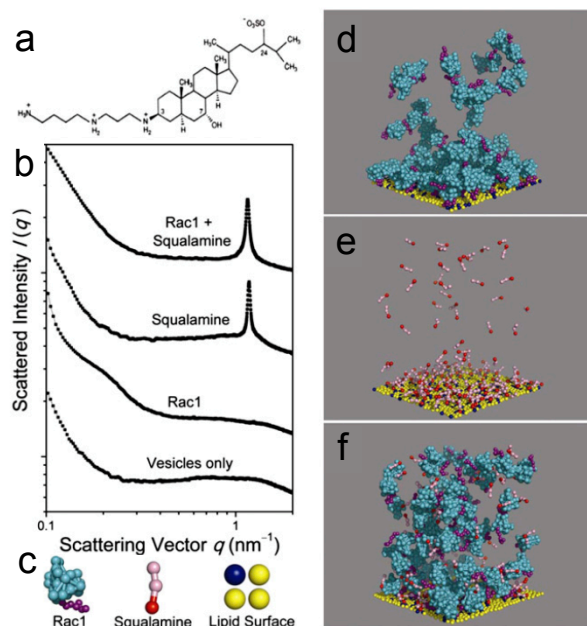


Figure 3.1. Squalamine strongly displaces Rac1 from model membranes in simulation and experiment (taken from Ref. [41]). (a) Squalamine chemical structure. (b) Diffraction patterns from lipid membrane vesicles, Rac1–membrane complexes, squalamine–membrane complexes, and membranes incubated with both Rac1 and squalamine (bottom to top). The diffraction pattern of the final case is nearly identical to the diffraction signature of squalamine–membrane complexes, indicating strong suppression of Rac1–membrane binding. (c) From left to right are the coarse-grained models of Rac1 with body beads in light blue and polycationic tail beads in purple, squalamine with the polycationic tail bead in red and the rest in pink, and lipids with uncharged beads in yellow and charged beads in blue. (d–f) Representative configurations from MD simulations of solutions of Rac1 (d), squalamine (e), and both Rac1 and squalamine (f), respectively, in the presence of a coarse-grained membrane in which 20% of the lipids are charged. Rac1 and squalamine are present at concentrations that yield the same net charge on all molecules, each higher than needed to neutralize the membrane. Squalamine was found to exhibit nearly two times stronger electrostatic binding than Rac1, and it displaced 56% of Rac1 from the membrane.

lipid bilayer membrane [41]. Squalamine was found to bind favorably to lipid membranes, displacing roughly 56% of the Rac1 proteins that adhered to the membrane in the absence

of squalamine (Fig. 3.1d–f). However, since the probability of membrane binding for a given molecule is related to the concentration of that molecule which is set by the simulation box height and so is somewhat arbitrary, these simulations fall short of fully explaining experimental observation, motivating the study of a system more closely related to experiment. Additionally, membrane–membrane like-charge attraction observed in the experimental system represents a breakdown in Poisson–Boltzmann (PB) theory due to factors that possibly violate its assumptions such as steric effects [53, 54], counterion correlations [55, 56], and internal molecular structure [57]. By using MD simulations to correlate system structure with thermodynamic variables we can identify which of these factors affects system behavior here, and by comparing the free energies of systems with different compositions we show that squalamine is a more effective counterion upon membrane condensation, and that squalamine can effectively eject Rac1 from lipid bilayer stacks.

### 3.2. Methods

All simulations were performed using a version of the LAMMPS package [58] that was modified as discussed below. To study the condensation of lipid bilayer membranes around squalamine molecules and Rac1 proteins, varying amounts of these species were placed in the interstitial region between stacked lipid membranes and the system was periodically replicated in all directions (Figs. 3.2a and c). Because the observed membrane-binding and protein-ejecting activity of squalamine is thought to be electrostatic in nature [41], it is relevant to determine if a model employing steric and electrostatic interactions alone will capture the observed behavior. Accordingly, species were represented by CG beads

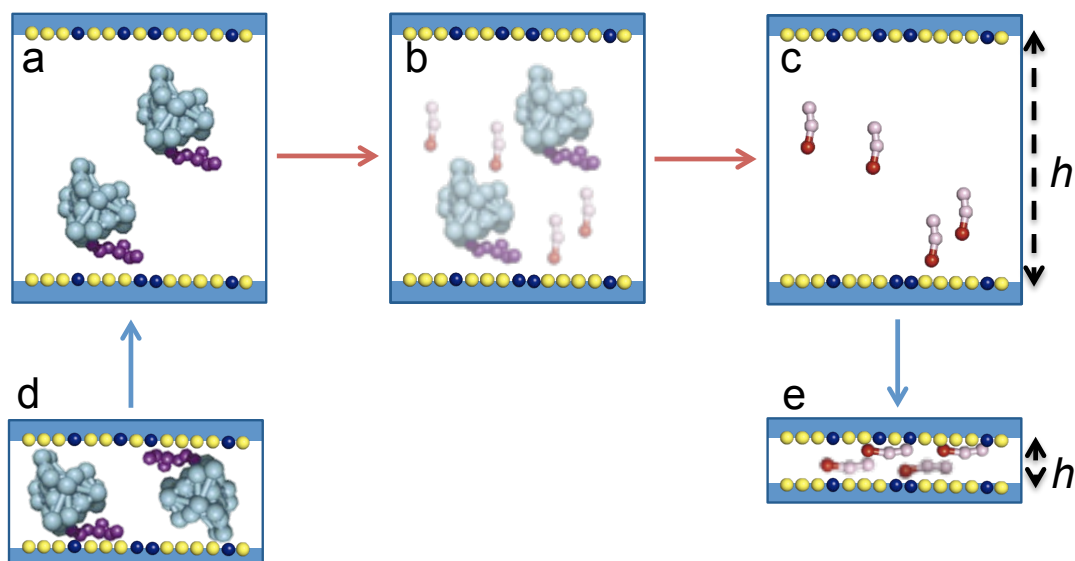


Figure 3.2. Simulated systems contain Rac1 (a and d) or squalamine (c and e) between charged bilayer membranes. The equilibrium configurations of these systems are determined by their free-energy minima, which are computed via thermodynamic integration (Sec. 3.2.6) during membrane condensation (blue arrows). The free energy required to exchange particles between systems is calculated using the Kirkwood integration scheme (red arrows, see Sec. 3.2.6). Which species most favorably condenses the membranes is determined via the total free-energy difference between the equilibrium separation of Rac1–membrane complexes (d) and that of squalamine–membrane complexes (e), minus the free energy required to replace Rac1 with squalamine in bulk (Sec. 3.3.3).

or assemblies of beads that interact with each other through generic short-range potentials. Additionally, long-range electrostatic interactions were calculated using the Ewald summation method. Polarization effects resulting from inhomogeneities in the dielectric constant were not taken into account.

### 3.2.1. Coarse-graining

The system was constructed to model the excluded-volume and electrostatic interactions of species placed between stacked membranes and the outer leaflets of the membranes.

Each membrane surface was represented by beads of uniform size  $7.57 \text{ \AA}$  at a fixed areal density  $(8.5 \text{ \AA})^{-2}$  per membrane, chosen to correspond to SAXS experiments [41]. Membrane ripples induced by polybasic species such as Rac1 tend to be on the order of microns [59, 60], much larger than the scale of these simulations, so the membrane was modeled as flat and the beads representing the lipid head groups were confined to move in the  $x$ - $y$  plane. To accurately model the lipid composition of mammalian membranes, 20% of the beads representing the lipid head groups carried a charge of  $-e$  and the rest were neutral [52]. To represent the excluded volume of the bilayer membrane, two membrane surfaces were separated by a void space of  $d_{\text{bil}} = 4.5 \text{ nm}$  in the  $z$ -direction that all species were forbidden from entering, represented as the solid blue regions at the top and bottom of the configurations in Fig. 3.2.

The Rac1 and squalamine molecules were coarse-grained using VMD’s Shape-Based Coarse-Graining (SBCG) tool [61, 62], which takes as input the protein data bank (PDB) file of a molecule and the number of beads desired to represent it. To accurately and efficiently represent the shape of a molecule, the SBCG tool uses a distribution of bead sizes, however since the bead size determines the minimum separation between two beads and therefore the strength of electrostatic binding, we used beads of uniform diameter equal to that of the  $7.57 \text{ \AA}$  lipid beads. For the squalamine molecule this required three beads with a separation of  $9.6 \text{ \AA}$  between the head and body bead, and a separation of  $12.4 \text{ \AA}$  between the body and tail beads (Fig. 3.1c). Bead charges were assigned manually based on the structure of the squalamine molecule, i.e.,  $-e$  for the head bead, 0 for the body bead, and  $+3e$  for the tail bead.

To coarse-grain the Rac1 protein, the protein was isolated from the PDB file 2RMK [63] and separated into a body region and a tail region. Since the polybasic tail region dominates Rac1–membrane binding [64], it was coarse-grained with 7.57 Å beads, consistent with that of squalamine and the lipid head groups. A total charge of +5e on the tail was divided into seven partial charges of  $-0.91e$ ,  $-0.04e$ ,  $+0.86e$ ,  $+1.09e$ ,  $+2.09e$ ,  $+1.53e$ , and  $+0.38e$ , starting with the bead representing the C-terminus and moving toward the body. For the weakly charged body region of the Rac1, steric interactions dominate, so beads with diameter 11.6 Å were used to increase efficiency while modeling the Rac1 excluded volume. For the body and the tail, the VMD SBCG tool was used to obtain the number of beads (37 total) as well as their equilibrium relative positions, bond lengths, and partial charges (see Fig. 3.1c).

### 3.2.2. Bead interactions

The interaction between bonded beads was described by a harmonic potential

$$(3.1) \quad U_{\text{bond}} = 200\epsilon (r - r_0)^2 ,$$

with  $r$  the bead–bead separation,  $r_0$  the equilibrium separation, and  $\epsilon = k_{\text{B}}T/1.2$  the Lennard-Jones (LJ) unit of energy. Additionally, the intrinsic stiffness of the squalamine molecule was modeled by a harmonic bond-angle potential

$$(3.2) \quad U_{\text{angle}} = 4\epsilon(\theta - \pi)^2 ,$$

where  $\theta$  is the angle between bonds and  $\pi$  the equilibrium bond angle. All nonbonded beads interacted through a purely repulsive shifted-truncated LJ (STLJ) potential, truncated at  $r_{\text{cut}} = 2^{1/6}\sigma$ , where  $\sigma$  is the bead size given by the coarse-graining procedure, and shifted by  $\epsilon$  so that the force and energy vanish at  $r_{\text{cut}}$ . Electrostatic energies, forces, and virial pressures were calculated using particle–particle particle–mesh Ewald summation with a relative accuracy of  $10^{-4}$  [65]. As is customary in coarse-grained simulations of electrostatic complexation phenomena [66], the Bjerrum length was set to  $3\sigma$ . The solvent was modeled as a homogeneous medium with Brownian effects represented by a Langevin thermostat with temperature  $T = 1.2\epsilon/k_{\text{B}}$  and damping time  $10\tau$ , with  $\tau = \sigma\sqrt{m/\epsilon}$  the LJ unit of time and  $m$  the LJ unit of mass.

### 3.2.3. Simulation setup

Simulations were performed at the membrane–Rac1 and membrane–squalamine isoelectric points, i.e., the numbers of Rac1 and squalamine molecules were chosen to exactly countercharge the membrane surfaces. For systems at small spacings corresponding to equilibrium conditions this is a valid approximation since entropic concerns favor counterion release and energetics favors the binding of higher-valency species. This approximation is also used for larger separations for which it does not necessarily hold, but which serve as a convenient integration pathway to obtain the free-energy difference between different states (see Sec. 3.2.6). Since the free energy is independent of the pathway used to obtain it, the results are unaffected by this assumption. Squalamine, Rac1, and salt molecules were excluded from entering the interior of the bilayer membranes by STLJ walls that were co-planar with the membrane beads, and interacted with all non-membrane beads

via an STLJ potential with  $\epsilon = k_B T / 1.2$  and  $\sigma = 3.79 \text{ \AA}$ . The MD time step was set to  $t = 0.002\tau$  to ensure energy conservation, and a typical simulation run took at least 50 million time steps, corresponding to  $10^5\tau$ , yielding at least  $\sim 100$  independent samples.

### 3.2.4. Pressure calculation and barostatting

Mechanical equilibrium requires the pressure in the bilayers equals that in the bulk. Since the lateral compressibility of the lipid membrane was assumed to be much higher than the longitudinal compressibility of the system, the system was taken to be incompressible in the  $x$ - $y$  plane. Accordingly, the cross-sectional area of the box was fixed and only the  $z$ -dimension of the box was allowed to vary. Mechanical equilibrium is then equivalent to setting  $P_{zz,\text{bilayer}} = P_{\text{bulk}}$ , where  $P_{zz}$  is the  $zz$ -component of the stress tensor and  $P_{\text{bulk}}$  is the pressure in bulk. This is imposed in Sec. 3.3.1 by performing a series of isochoric ( $NVT$ ) simulations of varying  $L_z$  and interpolating to  $P_{zz,\text{bilayer}} = P_{\text{bulk}}$ , and in Sec. 3.3.2 by simulating at a constant pressure, for which we use a Berendsen barostat with damping time  $0.2\tau$  [67]. The imposed incompressibility of the membrane requires adding to  $P_{zz}$  a rigid-body correction  $P'_{zz} = F_{ij,z} \times d_{\text{bil}} / 6V$  when a particle  $i$  exerts a force  $\mathbf{F}_{ij}$  on either a wall or bead  $j$  that composes the bilayer membrane, which required modification of LAMMPS.

### 3.2.5. Chemical potential calculation

When this system is in equilibrium with a bulk solution that contains salt, there will likely be a nonzero salt concentration in the bilayer stacks that screens the interactions between the Rac1, squalamine, and bilayers. We impose chemical equilibrium between the stacked

bilayers and an external bulk solution. Chemical potentials  $\mu$  were calculated using the Widom insertion technique [68], whereby “test” molecules  $k$  of the salt are inserted into equilibrium configurations  $S$  causing energy changes  $\Delta U_{\text{ins}}$ . To avoid systems with a net charge,  $k$  is taken to be a charge-neutral set of  $n$  ions ( $n = 2$  for a 1:1 salt). The chemical potential  $\mu_k$  of a 1:1 salt molecule of type  $k$  is given by,

$$(3.3) \quad \mu_k = -k_{\text{B}}T \log \left\langle \frac{V^2 \exp[-\beta \Delta U_{\text{ins}}]}{(N_k + 1)^2} \right\rangle ,$$

where  $V$  is the system volume,  $\beta = 1/k_{\text{B}}T$ ,  $N_k$  is the number of molecules of type  $k$  in configuration  $S$ , and  $\langle \dots \rangle$  denotes an ensemble average. Here we arbitrarily set the thermal de Broglie wavelength  $\Lambda = 1$  in our simulation units [69, 70], since its value does not affect free-energy differences. For single-particle insertions, a representative sample of  $S$  is obtained by performing a number of insertions  $M_{\text{ins}}$  that scales as the box volume divided by a typical correlation volume of the system  $\lambda_{\text{B}}^3$  (see Fig. 3.3). The largest systems in this study had a side length  $\sim 10\lambda_{\text{B}}$ , requiring  $10^3$  insertions per configuration for one particle to fully sample the configuration. For a salt molecule consisting of  $n$  particles, the phase-space volume to be sampled increases exponentially with  $n$ . Accordingly, a 1:1 salt requires up to  $10^6$  insertions to fully sample a configuration (Fig. 3.3). This can be quite costly given the expense of the Ewald algorithm, so is performed efficiently by, for each particle  $i$  in  $n$ , choosing  $M_{\text{ins}}$  random particle positions and computing their individual

Ewald interaction energy with the  $N_S$  particles in equilibrium configuration  $S$

$$(3.4) \quad \Delta U_{\text{ins},i} = \frac{4\pi q_i}{V} \sum_{\mathbf{k} \neq 0} \frac{\exp[-k^2/4\alpha^2 + i\mathbf{k} \cdot \mathbf{r}_i]}{k^2} \sum_{j=1}^{N_S} q_j \exp[-i\mathbf{k} \cdot \mathbf{r}_j] - \sqrt{\frac{\alpha^2}{\pi}} q_i^2 + q_i \sum_{j=1}^{N_S} \frac{q_j \text{erfc}(\alpha r_{ij})}{r_{ij}},$$

with  $q$  the charges,  $V$  the system volume,  $\alpha$  the Ewald parameter, particle positions  $\mathbf{r}$ , and interparticle distances  $r_{ij}$ , then separately computing the  $M_{\text{ins}}^n$  cross-terms between inserted particles  $i$  and  $j$

$$(3.5) \quad \Delta U_{\text{ins},ij} = \frac{2\pi q_i q_j}{V} \sum_{\mathbf{k} \neq 0} \frac{\exp[-k^2/4\alpha^2]}{k^2} \sum_{j=1}^{N_S} \exp[i\mathbf{k} \cdot (\mathbf{r}_i - \mathbf{r}_j)] + \frac{q_i q_j \text{erfc}(\alpha r_{ij})}{2r_{ij}}.$$

Chemical equilibrium is obtained by performing simulations with varying  $N_{\text{salt}}$  and interpolating  $\mu_{\text{salt,bilayer}}$  to the chemical potential of the bulk salt solution.

### 3.2.6. Thermodynamic integration

To evaluate whether squalamine or Rac1 will dominate the condensation of the lipid bilayers, we obtain the equilibrium separations of membranes countercharged with either Rac1 or squalamine and compare their free energies by constructing a reversible path between them and integrating the appropriate derivative of the free energy along that path (Fig. 3.2). For changes in system length  $L_z$  along a path of constant  $N$ ,  $T$ , and

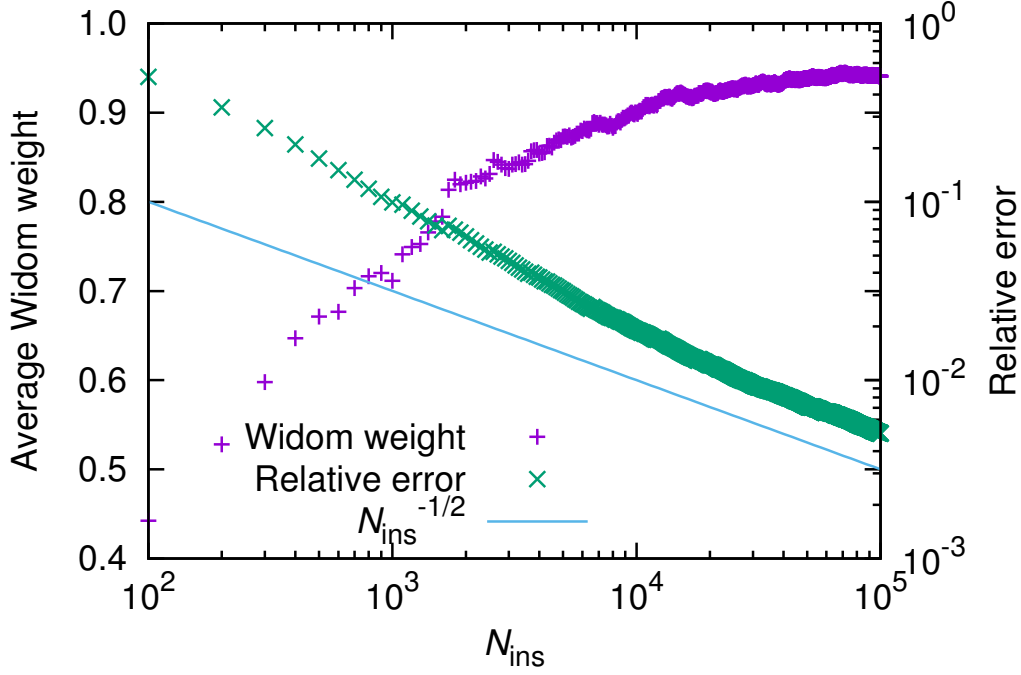


Figure 3.3. The average Widom weight  $\langle w_S \rangle \equiv \langle \exp[-\beta \Delta U_{\text{ins}}] \rangle$  converges slowly with respect to the number of insertions  $N_{\text{ins}}$  into a configuration  $S$  consisting of a 100 mM salt in a box of side length  $34\sigma$ . The relative error decreases as  $N_{\text{ins}}^{1/2}$  and is  $\sim 10^{-2}$  after  $10^5$  insertions, indicating the need for large  $N_{\text{ins}}$ . This can be done efficiently using Eqs. 3.4 and 3.5.

$A_{xy} = L_x L_y$ , we use the derivative of the Helmholtz free energy

$$(3.6) \quad \left( \frac{\partial F}{\partial L_z} \right)_{N,T} = -\Delta P_{zz} A_{xy}$$

where  $\Delta P_{zz} = P_{zz,\text{bilayer}} - P_{\text{bulk}}$ . For changes in the number of molecules  $N_k$  of type  $k$  along a path of constant  $P$ ,  $T$ , and  $N_{i \neq k}$ , the derivative of the Gibbs free energy is

$$(3.7) \quad \left( \frac{\partial G}{\partial N_k} \right)_{P,T,N_{i \neq k}} = \Delta \mu_k,$$

where the chemical potential difference  $\Delta\mu_k \equiv \mu_{k,\text{bilayer}} - \mu_{k,\text{bulk}}$  is used because these molecules are being exchanged with a bulk solvent.

Changes in the free energy due to the exchange of large species with the bulk cannot be quantified using the Widom insertion technique presented here because nearly all insertions result in particle overlap and therefore infinite  $\Delta U_{\text{ins}}$ . Instead we use the Kirkwood coupling parameter method [71], which tracks changes in free energy due to changes in the form of the interparticle potential  $U$ . To add or delete particles by this method,  $U$  is varied between  $U_{\text{I}}$  and  $U_{\text{II}}$ , corresponding to systems  $S_{\text{I}}$  and  $S_{\text{II}}$ , such that the particles we wish to delete are fully interacting in system  $S_{\text{I}}$  and do not interact with the other particles in  $S_{\text{II}}$ . Likewise, particles we wish to add are absent in  $S_{\text{I}}$  and present in  $S_{\text{II}}$ . Integrating between these two systems is usually accomplished by expressing  $U$  as a function of a coupling parameter  $\lambda$ , i.e.,

$$(3.8) \quad U(\lambda) = f_1(\lambda)U_{\text{I}} + f_2(\lambda)U_{\text{II}} ,$$

where  $\lambda$  varies from 0 to 1,  $f_1(1) = f_2(0) = 1$ , and  $f_1(0) = f_2(1) = 0$ . For the present study, all  $f_1(\lambda)$  have the form  $f_1(\lambda) = \lambda^{k_1}$  and all  $f_2(\lambda)$  have the form  $f_2(\lambda) = (1 - \lambda)^{k_2}$ . For simulations performed at constant  $NPT$ , changes in the free energy with respect to  $\lambda$  are given by

$$(3.9) \quad \Delta G \equiv \int_0^1 \left( \frac{\partial G(\lambda)}{\partial \lambda} \right)_{N,V,T} d\lambda = \int_0^1 \left\langle \frac{\partial W(\lambda)}{\partial \lambda} \right\rangle_{\lambda} d\lambda$$

$$(3.10) \quad = \int_0^1 \left\langle \frac{\partial f_1}{\partial \lambda} W_{\text{I}} + \frac{\partial f_2}{\partial \lambda} W_{\text{II}} \right\rangle_{\lambda} d\lambda ,$$

where  $W$  is the total potential energy of a system with interparticle potential  $U$  and  $\langle \dots \rangle_\lambda$  denotes an ensemble average of a system with a potential-energy function  $U(\lambda)$ . Values of  $\partial G/\partial \lambda$  were obtained directly from simulation and integrated via 5-point Gaussian quadrature, which was verified against ten-point Gaussian quadrature for small systems.

For the interparticle interactions in the present system, we use a multi-step Kirkwood integration scheme to connect each system to an ideal gas. We first use the Kirkwood method to discharge both systems with  $U(\lambda) = U_{\text{STLJ}} + U_{\text{wall}} + U_{\text{bond}} + (1 - \lambda)U_{\text{ES}}$ , where  $U_{\text{ES}}$  is the electrostatic potential. This is done for computational efficiency since the ensuing steps will not involve electrostatics, which incur most of the computational cost. After this, we decrease the STLJ interactions of both systems to zero using  $U(\lambda) = U_{\text{bond}} + U_{\text{wall}} + (1 - \lambda)^{k_2} U_{\text{STLJ}}$ . It has been noted that removal of a particle with a potential of the form  $r^{-n}$  in  $d$  dimensions can lead to a divergence in the integrand of Eq. 3.10 of the form  $\lambda^{(k_2 d/n)-1}$  [72]. This can lead to serious inaccuracies of the quadrature, so given  $d = 3$  in our system and  $n = 12$  for the STLJ potential, we eliminate this singularity using  $k_2 = 5$ .

To decouple the particles from the system walls representing the bilayers we use a truncated potential [72]

$$(3.11) \quad U_{\text{wall}} = \begin{cases} U_{\text{STLJ}}(r_0) - \frac{r_0}{2} \left( \frac{\partial U_{\text{STLJ}}}{\partial r} \right)_{r=r_0} \left[ 1 - \left( \frac{r}{r_0} \right)^2 \right] & \text{for } r < r_0 \\ U_{\text{STLJ}}(r) & \text{for } r \geq r_0, \end{cases}$$

chosen to be piecewise-continuous and differentiable, where  $r_0$  is chosen such that  $U_{\text{STLJ}}(r_0) = 10k_{\text{B}}T$ . To reduce the wall energy we choose  $f_2(\lambda) = (1 - \lambda)^2$  and use 10-point Gaussian quadrature.

This step yields an ideal-gas mixture with absolute free energy

$$(3.12) \quad G_{\text{ideal}} = Nk_{\text{B}}T \left[ \log \beta P - \sum_i \phi_i \log \phi_i \right],$$

where  $N$  is the total number of particles and  $\phi_i$  is the mole fraction of species  $i$ . The internal free energy  $\Delta G_{\text{int}}$  of bonded polyatomic molecules does not affect the final result, and so can be left as an unknown constant.

The excess free energy of each species in bulk solvent is computed by starting with an ideal gas of each molecule at its bulk concentration and performing Kirkwood integration with  $U(\lambda) = U_{\text{bond}} + \lambda^5 U_{\text{STLJ}}$  for the STLJ potential, and then with  $U(\lambda) = U_{\text{bond}} + U_{\text{STLJ}} + \lambda U_{\text{ES}}$  for the electrostatic potentials.

### 3.2.7. Finite-size effects

Differences between a finite, periodic system and an infinite, non-periodic system arise here due to a difference in boundary conditions in the electrostatics calculations. In an infinite, non-periodic system, the electric potential is constrained such that it vanishes at infinity. In a periodic system, the potential is instead constrained to average to zero over the box volume, which is a direct result of setting the zero-mode of the reciprocal-space Ewald sum to zero. This results in differences between the infinite and finite systems that go as the inverse system size [73]. These were accounted for by performing simulations of at least three separate system sizes and extrapolating to infinite system size as a function of  $1/N$  (Fig. 3.4).

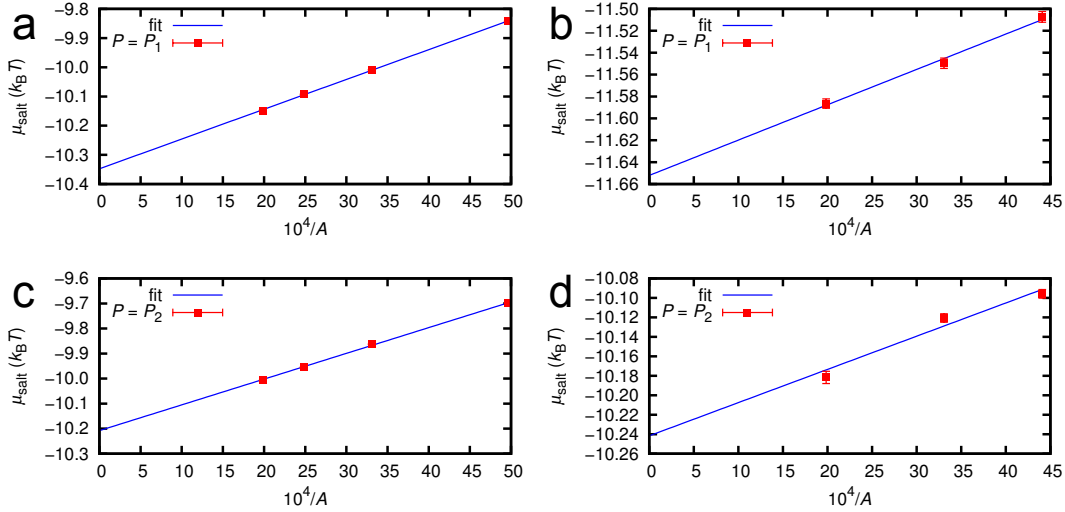


Figure 3.4. Finite-size effects are accounted for by a linear fit to the inverse system size [73]. Systems contain squalamine at a salt content  $\phi_{\text{squal}} = 0.3125$  (a and c) and Rac1 at a salt content  $\phi_{\text{rac}} = 3$ . Each system is held at constant cross-sectional area  $A$  and pressures  $P = P_1$  (a and b) and  $P = P_2$  (c and d), corresponding to systems in equilibrium with bulk salt concentrations of roughly 20 mM and 50 mM, respectively. Such fits are used to extrapolate all simulation results to infinite system size. The observed deviation from  $1/N$  dependence in the Rac1 data is slight and therefore neglected.

### 3.3. Results and Discussion

#### 3.3.1. Membrane condensation behavior of squalamine

It has been shown that dumbbell-like ions of the same net charge as squalamine can condense like-charged membranes even in the Poisson–Boltzmann limit due to their elongated internal structure [57]. While structurally similar to squalamine, these dumbbells have a different charge structure so that these results are not readily adaptable to squalamine. Accordingly, we first establish whether the coarse-grained model of squalamine used in this study can bind like-charged membranes at all, before the addition of salts that may hinder

condensation. Accordingly, isochoric simulations were performed for the case  $N_{\text{squal}} = 80$ ,  $N_{\text{Rac}} = 0$ , and  $N_{\text{salt}} = 0$  at varying bilayer separations  $h$ .  $P_{zz}$  exhibits significantly negative values down to an equilibrium membrane separation of 3 nm. Additionally, an orientational order parameter  $\mathcal{O}$ , defined as the fraction of condensed squalamine molecules that are upright with respect to the membrane (defined as  $\cos \theta > 0.8$ , where  $\theta$  is the angle between the squalamine molecule and the membrane normal for squalamine molecules with tail bead less than  $3\sigma$  from the membrane) shows strong correlation to  $P_{zz}$  as the membrane condenses (Fig. 3.5a). Notably,  $P_{zz}$  drops significantly when the membranes come close enough for oppositely bound squalamine molecules to interleaf, which was observed in the study of membrane–membrane like-charge attraction by dumbbell-like counterions mentioned above [57]. Integrating  $P_{zz}$  from the largest separation  $h = 10$  nm to the equilibrium separation  $h = 3$  nm yields  $\Delta F = -0.35k_{\text{B}}T$  per squalamine, indicating moderate attraction upon condensation. Notably, the observed equilibrium separation presented overestimates that in experiment by a factor of four. To test how this depends on the coarse-grained bead size, simulations were performed with bead of size  $\sigma = 2.5 \text{ \AA}$ , one third that of the larger beads. The squalamine model consisted of 9 beads connected in a linear chain by bond potentials Eq. 3.1 with  $r_0 = 2.7 \text{ \AA}$  and angle potentials Eq. 3.2 with  $\theta_0 = \pi$ . The tail (net charge  $+3e$ ) was modeled by three monovalent charges at one end, and the head (net charge  $-e$ ) was modeled with a monovalent bead at the opposite end, and all other beads were neutral. The electrostatic coupling was decreased so that the Bjerrum length was three times the reduced bead size [66]. The resulting equilibrium separation agrees well with experiment SAXS results (Fig. 3.6).

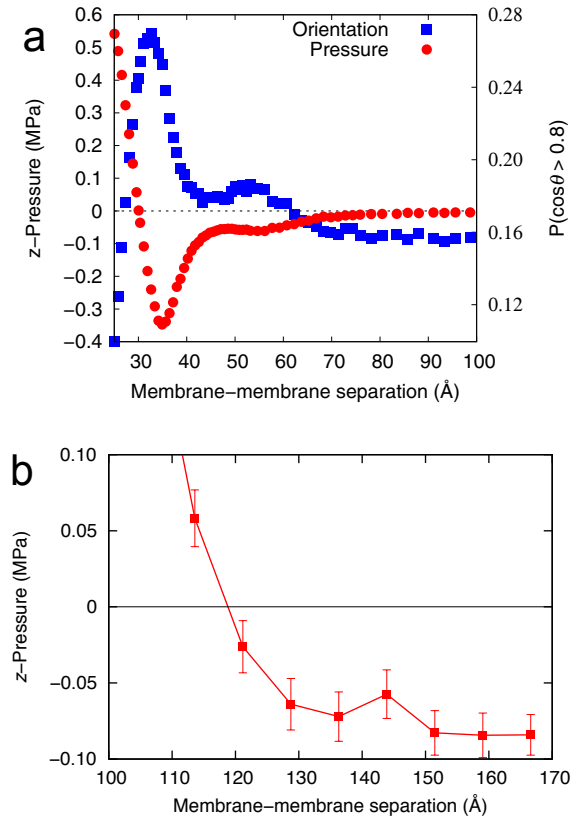


Figure 3.5. Condensation of lipid membranes mediated by squalamine or Rac1 in the absence of salt. (a) For the lipid membranes condensing around squalamine molecules, the  $zz$ -component of the stress tensor  $P_{zz}$  and the orientational order parameter  $\Theta$  of the squalamine molecules exhibit strong correlation. With decreasing bilayer separation, squalamine molecules begin to orient perpendicularly to the membrane, thereby inducing a strong membrane-membrane attraction, indicated by a negative  $P_{zz}$ . (b)  $P_{zz}$  is plotted as a function of membrane separation in a system where Rac1 counter-charges the membranes. The associated negative pressures are smaller and the equilibrium spacing is larger than in the squalamine case, however there is still a sharply defined equilibrium separation. The error bars are smaller than the point size unless otherwise indicated.

We perform a similar set of simulations for  $N_{\text{squal}} = 0$  and  $N_{\text{Rac}} = 40$ . Results show that Rac1 induces membrane-membrane attraction down to an equilibrium separation of

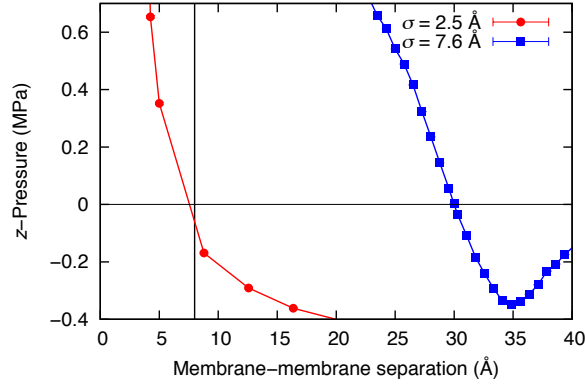


Figure 3.6. To test the dependence of the equilibrium membrane separation on bead size, squalamine molecules were modeled using a bead size one-third that of Fig. 3.5. The equilibrium separation is four times smaller than in previous simulations employing beads of size 7.6 Å, and is comparable to the SAXS results of Fig. 3.1b (black vertical line).

$h = 12$  nm (Fig. 3.5b). This is roughly two times smaller than that in experiment and corresponds to a system roughly three Rac1 molecules thick.

### 3.3.2. Membrane condensation in the presence of bulk salt

Because there is significant accessible solvent volume (i.e., volume not occupied by the Rac1 or membrane) in the condensed Rac1–membrane complexes observed above, it is likely that salts in an external bulk solution will penetrate the bilayer stacks, altering the interactions between charged species. When the bilayer stacks are in equilibrium with a bulk solution of salt concentration  $c_{\text{bulk}}$ , mechanical and chemical equilibrium must be maintained between the two phases. Accordingly, a constant pressure is maintained using a Berendsen barostat (Sec. 3.2.4) and chemical equilibrium is obtained by simulating a bilayer system at many salt concentrations and interpolating the chemical potential

$\Delta\mu = \mu_{\text{bilayer}} - \mu_{\text{bulk}}$  to zero. Additionally,  $\Delta\mu$  is integrated to obtain free-energy changes during condensation per Sec. 3.2.6.

The bulk phase contained salt and Rac1 at a molar ratio of 420:1 [41] and squalamine at a 2:1 molar ratio to Rac1 according to their charge ratio. Bulk solutions of two different concentrations were modeled by imposing pressures  $P_1 = 9.03 \times 10^{-3} k_B T / \sigma^3$  and  $P_2 = 2.26 \times 10^{-2} k_B T / \sigma^3$ , corresponding to salt-only solutions of 20 mM and 50 mM, respectively. The addition of Rac1, squalamine, and counterions at constant pressure increases the system volume so that the resulting salt concentrations are  $c_{\text{bulk},1} = 19.860(3)$  mM and  $c_{\text{bulk},2} = 49.58(5)$  mM. Widom insertion yields chemical potentials  $\mu_{\text{bulk},1} = -11.680(7)$  and  $\mu_{\text{bulk},2} = -10.084(2) k_B T$ . Finite size effects were accounted for by simulating three system sizes ( $N_{\text{salt}} = 420, 840, \text{ and } 1260$ ) and extrapolating to infinite system size as a function of  $1/N$  (Sec. 3.2.7).

These pressures were then imposed on bilayer stacks containing a number of squalamine molecules  $N_{\text{squal}}$  required to countercharge the membrane and a number of salt molecules  $N_{\text{salt}}$  that was systematically varied from run to run. The chemical potential in the stacks was obtained as a function of  $N_{\text{salt}}$  using Widom insertion (Sec. 3.2.5). For each set of parameters, finite-size effects were accounted for by simulating four different system cross-sectional areas ( $202\sigma^2, 302\sigma^2, 402\sigma^2, \text{ and } 504\sigma^2$ ) while keeping the areal density of all species constant, and extrapolating to infinite system size as a function of  $1/N$ . To compare systems of different size, the chemical potential of the salt is measured as a function of the salt-to-squalamine ratio  $\phi_{\text{squal}} = N_{\text{salt}}/N_{\text{squal}}$ .

At small concentrations, the system forms a tightly condensed stack corresponding to the equilibrium separation in the salt-free case (Sec. 3.3.1). In this regime, the rate of

increase of the system volume  $A\partial L_z/\partial N_{\text{salt}}$  is much smaller than  $1/c_{\text{bulk}}$  (Fig. 3.7a), so that the chemical potential increases monotonically with  $\phi_{\text{squal}}$  due to increasing crowding of the salt (Fig. 3.7b). The chemical potential crosses the bulk chemical potential at an equilibrium value  $\phi_{\text{squal,eq}} = 0.16$  for  $P_1$  and  $\phi_{\text{squal,eq}} = 0.34$  for  $P_2$ . Squalamine molecules therefore condense membranes to the point where they outnumber salt molecules by a factor  $\geq 3$ .

At a critical  $\phi_{\text{squal}} = \phi_{\text{squal,crit}}$ , the equilibrium separation begins increasing with a slope that corresponds to the bulk salt concentration and  $\mu_{\text{bilayer}}$  transitions from being above to being slightly below  $\mu_{\text{bulk}}$ . The sharpness of this transition is underscored by the observation of bistability in certain systems near the transition (Fig. 3.8). The value of  $\phi_{\text{squal,crit}}$  is between  $\phi_{\text{squal}} = 0.3125$  and  $0.4375$  for  $P = P_1$  and between  $0.5$  and  $0.625$  for  $P = P_2$ . To calculate the total free energy of condensation, we fit the chemical potential using  $a \log(b\phi_{\text{squal}})$ , where  $a$  and  $b$  are fit parameters, for  $\phi_{\text{squal}} < \phi_{\text{squal,crit}}$  and assume the contribution above  $\phi_{\text{squal,crit}}$  is negligible. Given the bounds of  $\phi_{\text{squal,crit}}$  above, the free energy of condensation is  $\Delta G_{\text{cond}} = 0.21(7)k_{\text{B}}T$  per squalamine for  $P = P_1$  and  $\Delta G_{\text{cond}} = 0.12(4)k_{\text{B}}T$  per squalamine for  $P = P_2$ , which are on the same order as the results for the salt-free case (Sec. 3.3.1), and show a moderate decrease with increasing bulk salt concentration.

Similar simulations were performed on systems containing a number of Rac1 molecules  $N_{\text{Rac}}$  required to countercharge the membrane, and  $N_{\text{salt}}$  was varied systematically as above. Finite-size effects were accounted for as above, using three different system cross-sectional areas ( $227\sigma^2$ ,  $302\sigma^2$ , and  $504\sigma^2$ ) instead of four due to computational cost. The bilayer separation (Fig. 3.7c) and salt chemical potential (Fig. 3.7d) were measured as a

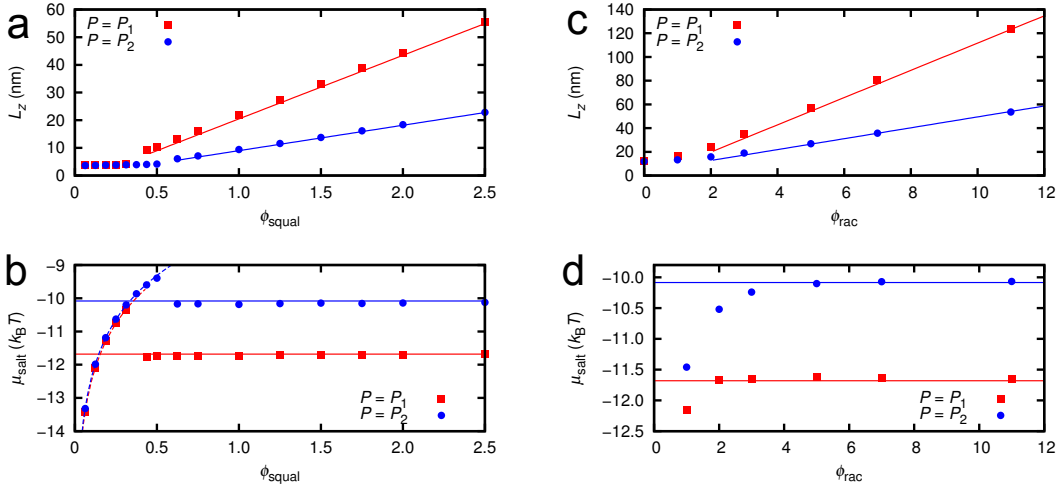


Figure 3.7. Condensation of lipid bilayers by squalamine and Rac1 at imposed pressures  $P_1$  (red) and  $P_2$  (blue) corresponding to bulk solutions with salt concentrations of roughly 20 mM and 50 mM, respectively. (a) At large bilayer separations, the rate of increase of the system height  $\partial L_z / \partial \phi_{\text{squal}}$  is roughly  $1 / (A_{\text{squal}} c_{\text{bulk}})$ , where  $A_{\text{squal}} = 6.3\sigma^2$  is the system area per squalamine molecule (solid lines). Below a critical salt-to-squalamine ratio  $\phi_{\text{squal,crit}}$ , the bilayers collapse to a condensed state similar to that in the salt-free case (Fig. 3.5a). (b) The chemical potential in squalamine–lipid stacks (points), bulk chemical potential (solid lines) and a fit to  $a \log b \phi_{\text{squal}}$  for  $\phi_{\text{squal}} < \phi_{\text{squal,crit}}$  (dotted lines) show strong condensation to a sharp minimum, in agreement with the experimental results in Fig. 3.1b. (c) When Rac1 counter-charges the membranes, the system height increases with a slope  $1 / (A_{\text{rac}} c_{\text{bulk}})$  for large  $\phi_{\text{rac}}$ , where  $A_{\text{rac}} = 12.6\sigma^2$  (solid lines). At small  $\phi_{\text{rac}}$ , the bilayer separation approaches the equilibrium separation of salt-free Rac1–membrane complexes (Fig. 3.5b). (d) The equilibrium Rac1 separations are represented by weak, shallow crossings of the bulk chemical potentials at  $\phi_{\text{rac,eq}} = 0.2$  and  $0.6$  for  $P = P_1$  and  $P = P_2$ , respectively, corresponding to equilibrium separations of 24 nm and 30 nm, respectively. This indicates that the addition of salt significantly weakens the condensation of Rac1–membrane complexes, and that the resulting lamellar stacks are very loosely bound, corresponding to the experimental results in Fig. 3.1b. All error bars are smaller than the point size.

function of the salt-to-Rac1 ratio  $\phi_{\text{rac}}$ , which at a given  $N_{\text{salt}}$  is twice the value of  $\phi_{\text{squal}}$  due to the Rac1:squalamine charge ratio of 2.

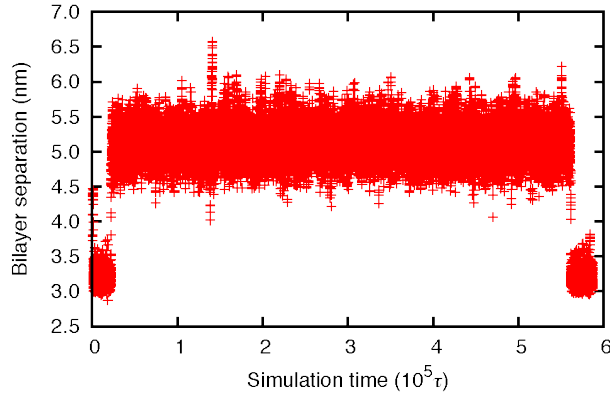


Figure 3.8. A simulated system consisting of squalamine and salts between bilayer membrane stacks held at constant pressure  $P = P_1$  is observed to undergo infrequent and sharp transitions between distinct separations indicating bistability. The pictured system has an area  $202\sigma^2$  and contains 32 squalamine molecules and salt-to-squalamine ratio  $\phi_{\text{squal}} = 0.375$ . Because the switching time is slow on the time scale of the simulations, ensemble averages taken from such systems are unreliable. Accordingly, the data point corresponding to  $P = P_1$  and  $\phi_{\text{squal}} = 0.375$  is not included in the final results (Fig. 3.7).

As in the squalamine case, small salt concentrations have little effect on the bilayer separation, and in this regime the chemical potential rises monotonically. However, this regime ends before  $\mu_{\text{bilayer}}(\phi_{\text{rac}})$  crosses  $\mu_{\text{bulk}}$  so that there is no tight binding as observed for squalamine and for Rac1 in the absence of salt. Instead, binding is represented by a weak, shallow crossing of  $\mu_{\text{bulk}}$  indicating loosely associated, weakly bound lamellae of spacing 24 nm for  $P = P_1$  and 30 nm for  $P = P_2$ , in agreement with the broad peak at large spacing observed in the experimental SAXS spectra (Fig. 3.1b). This indicates that the presence of a bulk salt plays a crucial role in determining the membrane binding behavior of Rac1.

### 3.3.3. Competition between Rac1 and squalamine

When both Rac1 and squalamine are present in solution, the two species compete to populate bilayer stacks. To determine which species will ultimately dominate membrane condensation, we calculated the free energy required to exchange two squalamine molecules in the bilayer with one Rac1 protein in the bulk

$$(3.13) \quad \Delta G_{\text{squal} \rightarrow \text{rac}} = \Delta G_{\text{squal} \rightarrow \text{rac}}^{\text{bil}} - \Delta G_{\text{squal} \rightarrow \text{rac}}^{\text{bulk}},$$

with  $\Delta G_{\text{squal} \rightarrow \text{rac}}^{\text{bil}}$  the free energy required to switch the squalamine molecules with Rac1 in the bilayer stacks and  $\Delta G_{\text{squal} \rightarrow \text{rac}}^{\text{bulk}}$  the free energy required to switch the squalamine with Rac1 in the bulk. These terms were calculated using thermodynamic integration and the Kirkwood coupling parameter method described in Sec. 3.2, and outlined as follows.

The free-energy change in the bilayer stacks is

$$(3.14) \quad \begin{aligned} \Delta G_{\text{squal} \rightarrow \text{rac}}^{\text{bil}} = & \Delta G_{\text{rac,cond}} + \Delta G_{\text{rac,kirk}} + G_{\text{rac,ideal}} \\ & - \Delta G_{\text{squal,cond}} - \Delta G_{\text{squal,kirk}} - G_{\text{squal,ideal}} + \Delta G_{\text{int}} \end{aligned}$$

with  $\Delta G_{\text{rac,cond}}$  and  $\Delta G_{\text{squal,cond}}$  the free energies of condensation obtained from thermodynamic integration of  $\Delta\mu$  from salt contents  $\phi_{\text{rac,eq}}$  and  $\phi_{\text{squal,eq}}$ , to salt contents  $\phi_{\text{rac,kirk}} = 3.0$  and  $\phi_{\text{squal,kirk}} = 0.75$ , chosen arbitrarily (Eq. 3.7);  $\Delta G_{\text{rac,kirk}}$  and  $\Delta G_{\text{squal,kirk}}$  the free-energy differences between fully interacting systems of compositions  $\phi_{\text{rac,kirk}}$  and  $\phi_{\text{squal,kirk}}$ , and ideal gas mixtures of the same compositions (Eq. 3.10);  $G_{\text{rac,ideal}}$  and  $G_{\text{squal,ideal}}$  the absolute free energies of ideal gas mixtures of compositions  $\phi_{\text{rac,kirk}}$  and  $\phi_{\text{squal,kirk}}$  (Eq. 3.12); and  $\Delta G_{\text{int}}$  accounting for the internal free energies of the Rac1 and squalamine molecules that arise due to their bond potentials.  $\Delta G_{\text{int}}$  will cancel when

computing  $\Delta G_{\text{squal} \rightarrow \text{rac}}$  (see below) and so can be taken as an unknown constant. Since  $\Delta\mu$  is small for the Rac1 systems above  $\phi_{\text{rac}} = \phi_{\text{rac,eq}}$  (see Fig. 3.7b), the free-energy change  $\Delta G_{\text{rac,cond}}$  is negligible. Squalamine exhibits significant  $\Delta\mu$  during condensation, and  $\Delta G_{\text{squal,cond}}$  is given in Sec. 3.3.2. The resulting free-energy differences were  $\Delta G_{\text{squal} \rightarrow \text{rac}}^{\text{bil}} = -6.13(13)k_{\text{B}}T + \Delta G_{\text{int}}$  for  $c_{\text{bulk},1}$  and  $\Delta G_{\text{squal} \rightarrow \text{rac}}^{\text{bil}} = -2.83(6)k_{\text{B}}T + \Delta G_{\text{int}}$  for  $c_{\text{bulk},2}$ .

The free-energy change in the bulk

$$(3.15) \quad \Delta G_{\text{squal} \rightarrow \text{rac}}^{\text{bulk}} = \Delta G_{\text{rac,kirk}} + G_{\text{rac,ideal}} - G_{\text{squal,ideal}} - \Delta G_{\text{squal,kirk}} + \Delta G_{\text{int}}$$

was calculated similarly to  $\Delta G_{\text{squal} \rightarrow \text{rac}}^{\text{bil}}$ . The condensation free energy is omitted because the Kirkwood integration is performed at the equilibrium salt content. The resulting changes in free energy are  $\Delta G_{\text{squal} \rightarrow \text{rac}}^{\text{bulk}} = -9.07(22) + \Delta G_{\text{int}}$  for  $P = P_1$  and  $\Delta G_{\text{squal} \rightarrow \text{rac}}^{\text{bulk}} = -4.42(13) + \Delta G_{\text{int}}$  for  $P = P_2$ . This calculation neglects interactions between the Rac1 and squalamine in the bulk according to the assumption that they are sufficiently dilute. This was tested using simulations in which varying dilute concentrations of squalamine were inserted into the bulk, which yielded a free-energy difference per squalamine of  $0.06(17)k_{\text{B}}T$ .

The total change in free energy  $\Delta G_{\text{squal} \rightarrow \text{rac}} = \Delta G_{\text{squal} \rightarrow \text{rac}}^{\text{bil}} - \Delta G_{\text{squal} \rightarrow \text{rac}}^{\text{bulk}} = 2.9(3)k_{\text{B}}T$  for  $P = P_1$  and  $1.58(18)k_{\text{B}}T$  for  $P = P_2$ , indicating that squalamine favorably condenses membranes over Rac1 in both systems, and that the squalamine molecule ejects Rac1 from these stacks in spite of its smaller valency.

### 3.4. Conclusion

Using coarse-grained simulations, I have demonstrated the effectiveness of the squalamine molecule in competitively binding membrane complexes and ejecting proteins of viral origin such as Rac1. Using free-energy perturbation and integration techniques, I have obtained free-energy differences between Rac1–membrane and squalamine–membrane complexes in equilibrium with external bulk solutions of two different salt concentrations, and shown that in both cases squalamine–membrane complexes are favored over Rac1–membrane complexes despite the higher valency of the latter. Additionally, I have elucidated how the elongated internal structure of the squalamine molecule aligns perpendicularly to phospholipid membranes to enhance membrane binding. The ability of the present model, which employed only electrostatics and steric interactions, to replicate this competitive binding indicates that electrostatics plays an important role in the ejection of Rac1 from membrane stacks. This expulsion of proteins of viral origin may be important to the antiviral properties of squalamine per Ref. [41].

## CHAPTER 4

**Ionic current rectification in asymmetric graphene oxide  
nanochannel networks**

This chapter represents a close comparison of theoretical research and computer simulations. To present a complete story, I have included theoretical calculations that were performed by Niels Boon.

## ABSTRACT

Recent studies have demonstrated that graphene oxide is an effective, cost-efficient material for ionic current manipulation. To provide mechanistic insight into ionic current rectification (ICR) in graphene oxide nanochannel networks (NNs), we perform theoretical calculations and computer simulations. We demonstrate that, in contrast to many other ICR devices where accretion/depletion occurs inside the nanochannels, ICR here is due to ion accretion/depletion *outside* the cation-permselective NN. Asymmetries between interfaces in a microchannel–nanochannel–microchannel system are shown here to be the origin of ICR. Under high voltages and low concentrations a large region of space charge develops near the NN edge, leading to overlimiting currents. An analytical expression for the full current–voltage relationship is derived and we provide potential methods to maximize ICR in current devices. We suggest new system geometries and devices that may exhibit strong ICR according to the mechanisms described herein.

## 4.1. Introduction

Manipulation of ion transport is crucial for applications in biomedical engineering [74, 75] as well as for living cells, where it plays an essential role in homeostasis and signal transmission [76]. Methods that facilitate the construction of cost-efficient, scalable devices to manipulate ionic current are of biomedical interest because they can promote development of integrated fluidic chips, and are of biological interest because they enable imitation of cellular processes that may bolster understanding of ion channels in cell membranes. ICR is particularly important as an effective means to selectively control the transport of charged species through a channel [77]. To this end, several microchannel–nanochannel–microchannel devices have been constructed [78, 79, 80, 81, 82] that enable current rectification due to asymmetries in the nanochannel shape, internal charge distribution, and/or electrolyte densities at either microchannel–nanochannel interface. These channels are, however, expensive to manufacture and can only act on small amounts of fluid due to their size, which is a shortcoming for certain applications involving bulk amounts of fluid [83]. This has prompted continued research into the fabrication of cheap, efficient ionic rectifiers.

One candidate material for devices that can rectify ionic current is graphene oxide (GO), a charged amphiphilic sheet of atomic thickness that can form water-stable multilayer NNs [84]. These channels can exhibit strong ion-permselectivity, providing a means for ionic current manipulation [85, 86, 87]. Furthermore, macroscopic quantities of these “restacked” GO layers are easily fabricated at low cost and can be adapted to a range of applications as they are easily cut into a variety of shapes and sizes and their surface charge is easily modified using additives [83].

ICR is often well described by considering only the species that countercharges the channel, here forward taken as the cationic species, and its depletion or accretion within charged nanochannels as a function of the applied bias [88, 82, 89, 87]. The application of this mechanism to GO-based rectifiers [87] is, however, inaccurate, as changes in ion concentration inside the NN are shown here to be insufficient to generate a rectifying effect. Instead, we will demonstrate that it is the ability of GO to exclude the minority species, here forward taken to be the anionic species, and block its associated current that allows manipulation of the cationic current [83]. Additionally, we will show how high voltages and low ion concentrations lead to a violation of local electroneutrality over distances that are orders of magnitude larger than the Debye length, which is the characteristic decay length of electroneutrality violations in equilibrium systems. This can have a significant effect on the system's total ionic resistance as well as its rectification behavior, as it allows cation transport even under complete anion depletion. The results presented compare well with molecular dynamics simulations of a straight nanochannel, and simulations and theory of asymmetric GO NNs demonstrate and explain the emergence of rectification. These results provide insight into optimizing the performance of ICR in these devices and the creation of new devices that may exhibit ICR.

ICR devices consisting of microchannels in series with a charged nanochannel have been studied using the Poisson–Nernst–Planck equations solved under various geometries and charge distributions [88, 90, 89, 82, 77, 91, 92, 93, 93, 94]. In particular, numerical and analytical studies by Green *et al.* [91] of a different but related system have shown that an asymmetric microchannel–nanochannel–microchannel geometry can yield rectification. The geometric asymmetry of the system studied by Green *et al.* results

from sharp discontinuities in the channel cross-sectional area. These discontinuities reduce the rectification ratios below those that we will report in the present work, in which the cross-sectional area changes gradually inside the nanochannel network. Furthermore, the system studied by Green *et al.* is assumed to be electroneutral everywhere, whereas the large electric fields in the nanoscale system studied here necessitate the treatment of space charge (SC), i.e., non-neutral, regions that heavily influence the current–voltage ( $I$ – $V$ ) relationship at high voltage. Lastly, the sharp jumps in cross-sectional area in the system studied by Green *et al.* necessitate a full three-dimensional solution to the Poisson–Nernst–Planck equations, whereas here a one-dimensional treatment describes the system fully and is favorable given that it yields simple analytic expressions. Both results reduce to the same expression in the simple (non-rectifying) case of a straight nanochannel below the limiting current. Additionally, Miansari *et al.* [86, 95] explained the rectification behavior of GO NNs via concentration polarization (CP), however these results were confounded by a so-called “ion trapping” effect that led to anomalous rectification even in symmetric GO NNs, which was not reproduced in independent experiments [83, 85].

## 4.2. Results and Discussion

Charged nanochannels such as GO can manipulate ionic current as long as the surface charge  $\sigma$  satisfies  $c_0 \lesssim \sigma/eh$  [96], with  $c_0$  the bulk salt concentration,  $\sigma \sim -10$  mC/m<sup>2</sup> for GO,  $e$  the elementary charge, and  $h$  the channel width, which is 1 nm for GO. Strong anion exclusion occurs only if  $h \lesssim \lambda_D$ , with the Debye length of a monovalent salt  $\lambda_D = \sqrt{\epsilon\epsilon_0 k_B T / 2e^2 c_0}$ , with the free space permittivity  $\epsilon_0$ , the relative permittivity  $\epsilon$ ,

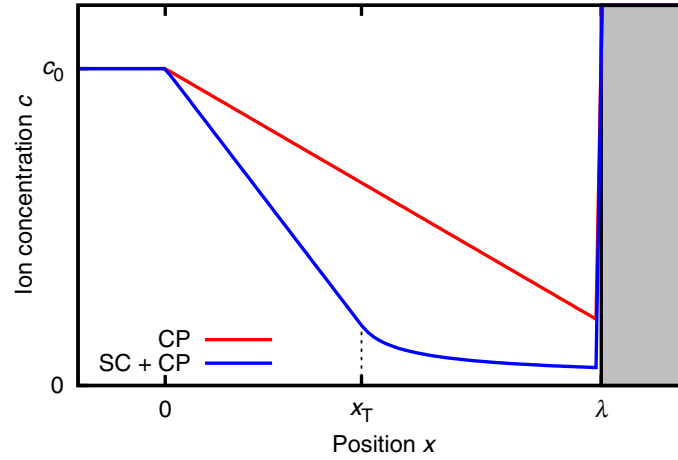


Figure 4.1. An illustration showing the dependency of the ion concentration profile on the ion current towards the cation-selective GO (gray). At small applied voltages, the solution can be approximated as locally electroneutral and the concentration decreases linearly from the bulk concentration  $c_0$  at  $x = 0$  to the GO–solution interface at  $x = \lambda$  (red curve). For large applied bias where CP gradients are steep, local electroneutrality holds until the ion concentration approaches small  $c$  at  $x = x_T$ , above which cations penetrate the depleted layer adjacent to the GO (blue). This allows currents larger than in the locally electroneutral case. The induced changes in ion concentration lead to variation in the conductivity and therefore produce a nonlinear relation between the current and the resistance of the system. Note that very close to the GO–solution interface, the concentrations may increase again due to the presence of a double layer.

the Boltzmann constant  $k_B$ , and the temperature  $T$ . Such selective ionic exclusion affects the transport properties of both species and can provide a dominant contribution to the resistance of the system [97, 98, 99]. In the following section we derive the nonlinear  $I$ – $V$  relationship for a symmetric system with a permselective component and then show how asymmetries can be introduced to induce ICR.

### 4.2.1. Theory

Because the present system consists of straight channels connected to a GO NN, we describe the ionic current using the one-dimensional Poisson–Nernst–Planck equations

$$(4.1) \quad -j_{\pm} = \frac{D_{\pm}c_{\pm}}{k_{\text{B}}T} \partial_x \mu_{\pm} ;$$

$$(4.2) \quad -j'_{\pm} = \partial_x c_{\pm} \pm c_{\pm} \partial_x \phi ;$$

$$(4.3) \quad -\partial_x^2 \phi = 4\pi\lambda_{\text{B}} (c_{+} - c_{-}) ,$$

with the (monovalent) cationic/anionic species specified + and –, respectively,  $j$  the flux density,  $D$  the diffusion coefficient,  $j' = j/D$  the scaled flux density,  $c$  the local concentration,  $\mu$  the chemical potential,  $e$  the elementary charge,  $\phi = e\Psi/k_{\text{B}}T$  the dimensionless electric potential, and  $\partial_x$  denoting partial derivation with respect to the position  $x$ . Note that the PNP equations assume the ions can be described by ideal point charges, such that the chemical potential is given by  $\mu_{\pm} = \mu_{\pm,0} + \log(c_{\pm}/c_{\pm,0}) \pm e\phi$ , where  $\mu_{\pm,0}$  is the chemical potential given  $c_{\pm} = c_{\pm,0}$  and  $\phi = 0$ . As presented, Eq. 4.2 disregards solvent flow, which is accurate if the solution is locally electroneutral such that the momentum imparted on the fluid by cationic and anionic drift cancels. Solvent flow can also be neglected in a stagnant layer close to the interfaces, as we will discuss below. Additionally, Eqs. 4.1 to 4.3 represent a mean-field theory that disregards correlations between ions. Molecular dynamics simulations (see below) show that this assumption is accurate for the present system.

To unify Eqs. 4.1 to 4.3 into a single expression that captures the CP and SC regimes, they are first re-expressed in terms of the electric field  $E \equiv -\partial_x \phi$ . The expressions for

the cation and anion currents (Eq. 4.2) are summed to obtain

$$(4.4) \quad j'_+ + j'_- = -\partial_x (c_+ + c_-) + E (c_+ - c_-) .$$

The anion concentration is replaced using Eq. 4.3

$$(4.5) \quad j'_+ + j'_- = -\partial_x \left( 2c_+ - \frac{\partial_x E}{4\pi\lambda_B} \right) + \frac{E\partial_x E}{4\pi\lambda_B} ,$$

which is integrated to obtain an expression for the cation concentration

$$(4.6) \quad c_+ = -\frac{j'_+ + j'_-}{2}x + \frac{\partial_x E}{8\pi\lambda_B} + \frac{E^2}{16\pi\lambda_B} + \text{const} .$$

Substituting this into the expression for cation current Eq. 4.2 and redefining the integration constant yields

$$(4.7) \quad (j'_+ - j'_-) + (j'_+ + j'_-)Ex + \frac{\partial_x^2 E}{4\pi\lambda_B} - \frac{E^3}{8\pi\lambda_B} + \text{const} \cdot E = 0 ,$$

which is the unified Poisson–Nernst–Planck equation, expressed in terms of the electric field [100]. This expression is in general not analytically solvable. We will therefore proceed by considering various physical assumptions corresponding to the different regimes of electric field and concentration in our system. The resulting field profiles and local osmotic pressure in the different regimes are connected to yield an accurate description of the current–voltage behavior of the system.

**4.2.1.1. Classical concentration polarization.** We consider a system with bulk concentration  $c_0$  at position  $x = 0$  and a permselective GO NN at position  $x = \lambda$  (Fig. 4.1).

To obtain a first approximation of the system behavior, we assume local electroneutrality so that Eq. 4.3 reduces to  $c_+ = c_- = c$  and Eq. 4.2 becomes

$$(4.8) \quad \partial_x c = -(j'_+ + j'_-)/2 ;$$

$$(4.9) \quad cE = (j'_+ - j'_-)/2 .$$

The concentration gradient given by Eq. 4.8 is nonzero as long as there is a difference in the magnitudes of scaled ionic fluxes, which is the case in a system with a permselective component. Solving Eq. 4.9 for  $c$  and substituting into Eq. 4.2 gives  $\partial_x E^{-1} = -(j'_+ + j'_-)/(j'_+ - j'_-)$  which is integrated and then multiplied by  $(j'_+ - j'_-)E$  to obtain

$$(4.10) \quad (j'_+ - j'_-) + (j'_+ + j'_-)Ex + \text{const} \cdot E = 0 ,$$

which is Eq. 4.7, neglecting the third and fourth terms.

The concentration profile in this regime is obtained by integrating Eq. 4.8, showing linear decay,

$$(4.11) \quad c = c_0 - \left( \frac{j'_+ + j'_-}{2} \right) x .$$

Therefore, assuming some degree of cation-permselectivity, a cation current directed from the bulk into the GO induces a concentration profile that decreases linearly from the system bulk to the interface, and an opposite current induces an opposite profile. At this point we assume perfect cation-permselectivity ( $j_- = 0$ ) and integrate Eq. 4.1 to obtain

the chemical-potential drop over the CP layer, i.e.,  $0 < x < \lambda$  for the CP curve in Fig. 4.1

$$(4.12) \quad \Delta\mu_{\text{CP}} = IR_{\text{CP}} = 2k_{\text{B}}T \log \left( 1 - \frac{\lambda j'_+}{2c_0} \right) .$$

While  $\lambda$  is imposed in theory, it emerges spontaneously in experiment and corresponds to the thickness of the stagnant layer [98]. This length could be controlled in experiment by damping hydrodynamics using a gel over the intended length  $\lambda$  [98].  $\Delta\mu_{\text{CP}}$  becomes infinite when the concentration at  $x = \lambda$  goes to 0, corresponding to the limiting current

$$(4.13) \quad I_{\text{max}} \equiv eAj_{+, \text{max}} = 2D_+eAc_0/\lambda ,$$

with  $A$  the channel cross-sectional area. An asymmetry in any factor on the right-hand side of Eq. 4.13 will therefore induce different  $I_{\text{max}}$  in the stagnant layers on either side of the GO NN. The total voltage drop in an asymmetric system is given by

$$(4.14) \quad V = IR_{\text{ex}} - \frac{2k_{\text{B}}T}{e} \log \left( \frac{1 - I/I_{\text{max,L}}}{1 + I/I_{\text{max,R}}} \right) ,$$

where  $I_{\text{max,L/R}}$  is the limiting current density on the right/left side of the GO and  $R_{\text{ex}}$  is the total resistance of the bulk solution on the right and left sides combined with the internal resistance of the GO, i.e.,  $R_{\text{ex}} = R_{\text{bulk,R}} + R_{\text{GO}} + R_{\text{bulk,L}}$ , here forward assumed to be negligible.

An asymmetry in any of the factors in Eq. 4.13 between the right and left side of the NN, e.g., a difference in channel width, will lead to ICR that approaches a maximum ratio

$$(4.15) \quad r_{\text{max}} = \frac{I_{\text{max,R}}}{I_{\text{max,L}}} = \frac{D_{+,R} A_{\text{R}} c_{0,R} \lambda_{\text{L}}}{D_{+,L} A_{\text{L}} c_{0,L} \lambda_{\text{R}}}$$

at high voltages, where we assume  $I_{\max,R} > I_{\max,L}$ , and has a rectification ratio  $r < r_{\max}$  at lower voltages. Under the local electroneutrality assumption, the current cannot be higher than  $I_{\max}$ . In reality, a number of factors including solvent flow and space charge can cause overlimiting currents, i.e.,  $I > I_{\max}$  [97, 98, 99, 101].

**4.2.1.2. Space charge.** The local electroneutrality assumption is useful on large scales though strictly violated for steady-state currents in systems with spatially varying resistance due to varying ion concentrations. Inducing a constant current in such a system requires a spatially varying electric field and thus a nonvanishing charge density. This charge density is usually negligible in comparison to the local ion concentration itself and can therefore be safely ignored in the CP regime. However, this space charge can have a significant effect, e.g., when currents  $I \sim I_{\max}$  cause strong depletion. In this case, Eq. 4.11 describes the concentration profile up to a transition point  $x = x_T$ , at which it gives way to a SC region in which  $c_+(x) \gg c_-(x)$  (see Fig. 4.2d). The presence of cations in an anion-depleted region can decrease the overall resistance of the system leading to overlimiting currents  $I > I_{\max}$ .

We can derive the approximate cation concentration  $c(x)$  for  $x > x_T$  by assuming that the anion concentration is negligible compared to the cation concentration and that the current in the SC region is dominated by the drift term i.e.,  $j' = cE$ . Here cations are the sole species present so we have dropped all subscripts. Using the Poisson equation to substitute for the cation concentration yields

$$(4.16) \quad j' = \frac{E\partial_x E}{4\pi\lambda_B} = \frac{\partial_x E^2}{8\pi\lambda_B},$$

which is integrated to obtain

$$(4.17) \quad E j' x - \frac{E^3}{8\pi\lambda_B} + \text{const} \cdot E = 0 ,$$

i.e., Eq. 4.7 assuming that the first and third terms are negligible. The electric field is given by

$$(4.18) \quad E(x) = \sqrt{8\pi\lambda_B j' x + \text{const}} ,$$

where the integration constant is set by the boundary condition  $c(x_T) = c_{0,SC}$ . The concentration is then

$$(4.19) \quad c(x) = \left( \frac{8\pi\lambda_B}{j'} (x - x_T) + \frac{1}{c_{0,SC}^2} \right)^{-1/2} .$$

**4.2.1.3. Combining the CP and SC regions.** We obtain a complete description of this system by connecting the CP and SC regimes to yield a single expression. We first re-express Eq. 4.7 assuming perfect permselectivity, i.e.,  $j_- = 0$

$$(4.20) \quad \xi^{-3} + E\xi^{-3}x + \partial_x^2 E - E^3/2 + \text{const} \cdot E = 0 ,$$

where  $\xi \equiv (4\pi\lambda_B j'_+)^{-1/3}$ . We choose  $x = 0$  at the point where the CP concentration Eq. 4.11 is zero so that the CP electric field is

$$(4.21) \quad E_{CP}(x) = -1/x .$$

The SC and CP regions are combined by imposing continuity of the electric field and its derivative. Accordingly, we substitute Eq. 4.21 into the SC result Eq. 4.16 to obtain the

$x$ -coordinate of the transition from SC to CP  $x_T = -\xi$ . Comparing Eqs. 4.18 and 4.21 yields the SC electric field

$$(4.22) \quad E_{\text{SC}}(x) = \xi^{-1} \sqrt{3 + 2x\xi^{-1}},$$

and the concentrations are then

$$(4.23) \quad c_{+, \text{CP}} = -\frac{x}{8\pi\lambda_B\xi^3};$$

$$(4.24) \quad c_{+, \text{SC}} = \frac{1}{4\pi\lambda_B\xi^2} \frac{1}{\sqrt{3 + 2x\xi^{-1}}}.$$

Note that although these are not continuous at the transition point  $x = -\xi$ , our choice of matching the electric field and its derivative ensures that the osmotic pressure is a continuous function, as the *total* ion concentration (cations and anions) is continuous. Our choice also enables extensions toward theories that involve both cations and anions in the space-charge regime (see Appendix).

The change in electric potential over the layers is

$$(4.25) \quad \Delta\phi_{\text{CP}} = \int_{-L_{\text{CP}}-\xi}^{-\xi} -E_{\text{CP}} dx = -\log\left(1 + \frac{L_{\text{CP}}}{\xi}\right)$$

$$(4.26) \quad \Delta\phi_{\text{SC}} = \int_{-\xi}^{-\xi+L_{\text{SC}}} -E_{\text{SC}} dx$$

$$(4.27) \quad = \frac{1}{3} \left[ 1 - \left(1 + \frac{2L_{\text{SC}}}{\xi}\right)^{3/2} \right]$$

and the change in chemical potential over the SC and CP layers together is

$$(4.28) \quad \frac{\Delta\mu_+}{k_B T} = \log c_+(L_{SC} - \xi) - \log c_+(-L_{CP} - \xi) + \Delta\phi_{SC} + \Delta\phi_{CP}$$

$$(4.29) \quad = -2 \log \left( 1 + \frac{L_{CP}}{\xi} \right) - \frac{1}{2} \log \left( 1 + \frac{2L_{SC}}{\xi} \right) + \frac{1}{3} \left[ 1 - \left( 1 + \frac{2L_{SC}}{\xi} \right)^{3/2} \right],$$

which is directly related to the resistance  $R_{CP+SC}$  of the CP + SC layer via  $\Delta\mu_+ = I_+ R_{CP+SC}$ . The CP and SC layer lengths are related via the total channel length  $\lambda = L_{CP} + L_{SC}$ , and  $L_{CP}$  is fixed by the bulk concentration  $c_0$  at the channel–bulk interface  $-L_{CP} - \xi$ , i.e.,  $L_{CP} = 8\pi\lambda_B\xi^3 c_0 - \xi$ . For systems constrained by a constant number of salt pairs  $N$  as opposed to those constrained to constant concentration at the bulk, the CP layer length is obtained by assuming the ion content outside the CP zone is negligible, yielding  $L_{CP} = \sqrt{16\pi\lambda_B\xi^3 N/A} - \xi$ .

As we will show, these expressions agree quantitatively with particle-based simulations without any fit parameters, supporting the validity of the assumptions taken in unifying the CP and SC regimes, and indicating that the present analysis can be directly applied to experiments.

#### 4.2.2. Simulation

To test our theoretical model, we first simulate a rectangular GO NN with identical inlet and outlet widths equal to the  $y$ -dimension of the simulation box and compare the observed ion distribution and  $I$ – $V$  relationship with theory (Fig. 4.2).

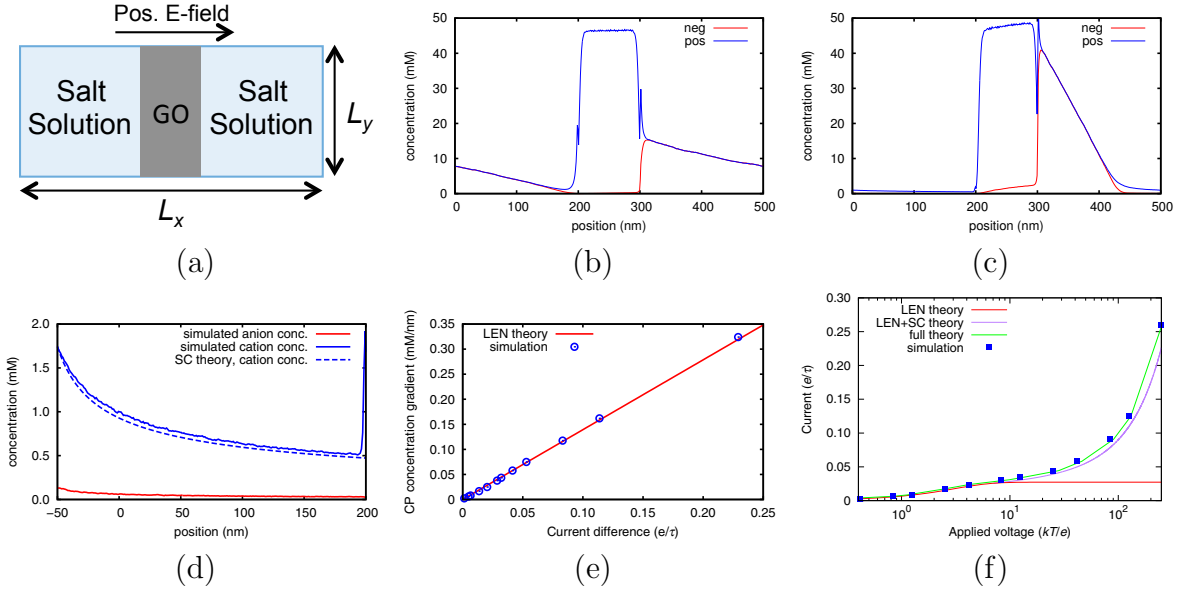


Figure 4.2. (a) System geometry: a symmetric rectangular GO NN with counterions is surrounded by 7.6 mM salt solution. (b), (c) Simulated anion (red) and cation (blue) concentrations for applied voltages of  $8.3k_B T/e$  (b) and  $250k_B T/e$  (c). Charge neutrality is obeyed over the linear CP region predicted by Eq. 4.11. A sharp downward jump is observed in the cation concentrations of (b) and (c) on entry into the nanochannel network due to the fact that the finite excluded volume of the GO sheets reduces the volume accessible to the ions. (c) exhibits a SC region whose form is dictated by Eq. 4.19. (d) The SC region of (c) is shown along with theoretical cation concentration given by Eq. 4.19, with  $c_0$  given by the measured cation concentration at  $-50$  nm (the same position as  $450$  nm in (c)). (e) The CP gradient versus the cation–anion current difference (blue) shows good agreement with Eq. 4.11 (red). Observed concentration gradients are obtained via a linear fit over the length of the CP region, which is at least  $100$  nm for all voltages. (f)  $I$ – $V$  relationship from simulation (blue) compared with Eq. 4.14 (red), Eq. 4.29 (purple), and Eqs. 4.40 and 4.39 (green), shown on a semilog plot for clarity. Equation 4.14 captures the behavior well up to  $V \sim 10k_B T/e$ , where the CP region approaches the length of the channel. Above this, Eq. 4.29 predicts the  $I$ – $V$  behavior qualitatively, however underestimates the current due to the assumption of perfect permselectivity. Equations 4.40 and 4.39 capture the behavior well in this case.

Capturing the nonlinear  $I$ - $V$  behavior observed in Eq. 4.14 requires currents  $I \sim I_{\max}$ .

The resistance of the CP layer is given by

$$(4.30) \quad R_{\text{CP}} = \int_0^\lambda [e\nu A(x)c(x)]^{-1} dx ,$$

where  $\lambda$  is the CP layer length,  $A(x)$  the cross-sectional area,  $c(x)$  the mobile ion concentration and  $\nu$  the mobility. This expression is by definition in agreement with the derivative with respect to the current  $I$  of Eq. 4.14. If  $A(x)$  is constant,  $R_{\text{CP}}$  is minimized when  $c(x)$  is constant, thus the voltage required to obtain  $I \sim I_{\max}$  has a lower bound at

$$(4.31) \quad V_{\min} = \frac{\lambda I_{\max}}{e\nu A c} = \frac{2k_{\text{B}}T}{e} ,$$

assuming that  $R_{\text{CP}}$  provides the dominant contribution to the total resistance. In actuality, the charge profile is far from constant for high voltages, so  $V_{\min}$  is chosen as our minimum simulated voltage. Since  $V_{\min}$  is independent of length, the small systems simulated require large electric fields, ranging from 0.3 kV/cm up to 200 kV/cm, far higher than in experiment [83] but below the breakdown field strength of water [102]. Additionally, since the total voltage drop over the electrodes is relatively small, we disregard water splitting at the electrodes.

Despite significant anion exclusion from the GO, an anion current roughly 20 times smaller than the cation current is observed (Fig. 4.3), which results in a small decrease in the CP slope per Eq. 4.11. The observed linear concentration profiles match Eq. 4.11, and the  $I$ - $V$  relationship is well modeled by Eq. 4.14 up to  $V \sim 10k_{\text{B}}T/e$ , which is the applied bias at which the concentration on the depleted side of the NN approaches zero (Fig. 4.2b). Strict electroneutrality is not required, so cations can penetrate the anion-depleted side of

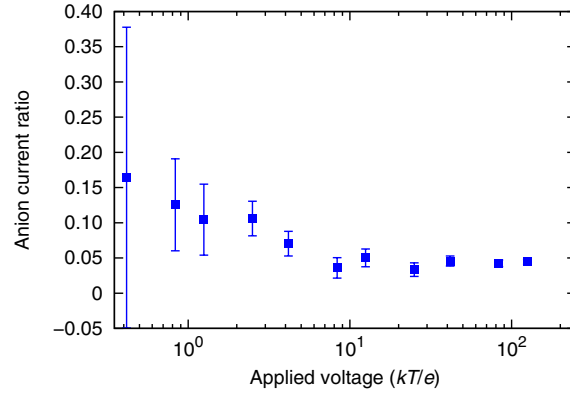


Figure 4.3. The ratio of the anion leakage current to the total current versus the applied bias. An anion leakage current roughly 20 times smaller than the total current is observed in a system with a rectangular GO NN (Fig. 4.2). This alters the CP slope per Eq. 4.11 (Fig. 4.2e) and has a small but noticeable effect on the  $I$ - $V$  relationship (Fig. 4.2f). For macroscopic filters at small ion concentrations, the GO NN provides much larger resistance to anion transport and this phenomenon can be neglected.

the NN creating a SC region that decreases the system's overall resistance (see Fig. 4.2d). Equation 4.29, which describes CP and SC regions in series, shows qualitative agreement with the simulation data but underestimates the observed currents. This is due to the nonzero anion current observed in simulation, which violates the approximations made in deriving Eq. 4.29. Going back to Eqs. 4.1 to 4.3 and repeating the steps outlined in the theory without the assumption of perfect cation permselectivity (see Appendix) yields expressions for the cation chemical potential drop and thus the resistance that ameliorate this discrepancy (Fig. 4.2f). These expressions have the disadvantage that they require both the cation and anion fluxes as inputs, and therefore do not yield a 1:1  $I$ - $V$  relation. In the limit of perfect cation permselectivity as in a macroscopic NN, these equations reduce to Eqs. 4.12 and 4.29, respectively, and a 1:1 relation is obtained.

Previous work suggests overlimiting currents can arise from either hydrodynamic turbulence or the development of SC [97, 98, 99, 101], however the implicit solvent used here disallows hydrodynamic effects. Accordingly, for a small system with damped hydrodynamics, i.e., that in a gel, overlimiting currents arise from the formation of SC regions [98].

To generate rectification, we simulate a NN with one narrow side and one wide side (Fig. 4.4a), with wide:narrow ratios  $\gamma = 1.8, 3, 5,$  and  $8$  according to experiment [83]. We impose the layer length  $\lambda$  via left and right channel lengths of  $100$  nm each and hold the concentration  $c_0 = 7.6$  mM at  $x = 0$  nm =  $350$  nm by inserting or deleting molecules during equilibration such that the concentration is correct at the beginning of production (see Sec. 5.2). This process is not deterministic, and the final number of ions in the system and thus the system conductance is subject to some randomness. Accordingly, for Figs. 4.4c and d, we obtain an error estimate by averaging over at least eight identical and independent simulations.

CP theory suggests the resulting rectification ratios  $r = \gamma$ , however systems with significant SC exhibit  $r < \gamma$  (Fig. 4.4d). We can calculate this reduction in rectification by repeating the analysis in Sec. 4.2.1.3 for the present system. We approximate the GO NNs as perfectly permselective and resistance-free, and account for the spatially varying width of the channels (bulk, left channel, and right channel) using a quasi-one-dimensional approach. Starting with  $c(0 \text{ nm}) = c(350 \text{ nm}) = c_0$ , we obtain the concentration throughout the bulk using equation Eq. 4.11. This assumes local electroneutrality in the bulk thereby constraining the validity of our calculations to  $8\pi\lambda_B c_0 \xi^3 - \xi > 25$  nm. The concentrations in the left and right channels are obtained by imposing continuity of  $c(x)$  at the bulk

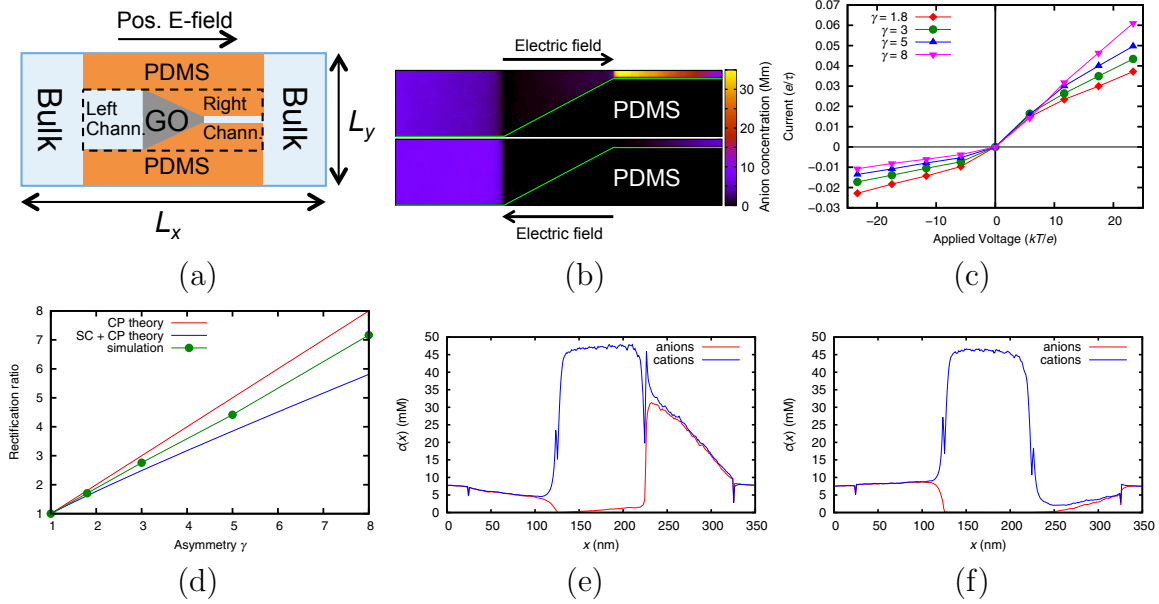


Figure 4.4. (a) System geometry: a trapezoidal GO NN is connected to 7.6 mM bulk salt solution by two channels. (b) Anion concentration around an asymmetric GO NN for  $\gamma = 8$  and applied voltages of  $4.2k_B T/e$  (top) and  $-4.2k_B T/e$  (bottom), from the dotted region in (a). (c)  $I-V$  curves for the four asymmetries used. (d) The ratio of the currents at applied voltages  $\pm 23.3k_B T/e$  as a function of the GO NN asymmetry  $\gamma$ , along with curves given by CP theory (see Sec. 4.2.1.1) and SC + CP theory (see Sec. 4.2.1.3).  $\gamma = 1$  corresponds to a symmetric system for which the rectification ratio is exactly 1. While the rectification ratio increases with increasing  $\gamma$ , it is below its ideal CP value due to SC effects. (e) and (f) show the cation and anion concentrations averaged per vertical slice of the systems depicted in (b), excluding the PDMS regions. The CP concentration gradient is greater in the right channel than the left, so that (f) exhibits significant depletion whereas (e) does not. This causes SC to develop at smaller reverse biases than forward biases, thereby decreasing the rectification ratio below its “ideal” CP value. Additionally, increased channel concentrations under forward bias (compare figures (e) and (f) at 225 nm and 125 nm, respectively) allow increased anion leakage current, which leads to an increased rectification ratio over the SC + CP value as discussed in the main text. In addition to the apparent jumps in concentration upon entry into the nanochannel network as discussed in Fig. 4.2, there are small downward peaks visible in (e) and (f) at 25 nm where the left channel begins and 325 nm where the right channel ends due to the finite extent of the soft LJ walls, which reduce the accessible volume of the ions.

boundaries ( $x = 25$  nm and 325 nm, respectively) and describing each channel separately using the one-dimensional solutions to the PNP equation given in Sec. 4.2.1.3. Allowing space charge accounts for the observed reduction of the simulated results below CP theory (Fig. 4.4d). How SC leads to a reduction in  $r$  is illustrated by  $c(x)$  for  $\gamma = 8$  and  $V = \pm 23.3k_B T/e$  (Fig. 4.4e and f). The CP gradient is directly related to channel width and is therefore larger in the right channel than the left, so SC develops in the former at lower bias. SC tends to decrease resistance and as a result, the rectification ratio will be lower than its “ideal” CP value.

Because the simulated GO is not perfectly permselective as assumed above, there will be a leakage flow of anions depending on the concentration at the filter inlet ( $x = 225$  nm in Fig. 4.4e and  $x = 125$  nm in Fig. 4.4f). Since this inlet concentration is higher under forward bias than reverse bias, there will be a more significant anion leakage current for forward biases, leading to a larger forward current and a larger rectification ratio than that expected from the SC + CP curve (Fig. 4.4d).

The discussion of CP above suggests that multiple factors in Eq. 4.13 can be manipulated simultaneously to affect the rectification ratio. For example, a system with  $\gamma = 10$  and  $\lambda_R/\lambda_L = 8$  would exhibit  $r_{\max} = 80$ . As such we simulate a system with a left channel of width 200 nm and length 25 nm, a right channel of width 20 nm and length 200 nm and a bulk region of width 200 nm and length 75 nm (Fig. 4.5). The CP channels and bulk were initially filled with uniform 7.6 mM salt solution, and the bulk concentration is kept constant as described in Sec. 5.2. Eleven independent simulations were performed at each electric field, yielding spatially averaged concentrations that range from 6.12(5) mM under a reverse bias of  $33k_B T/e$  to 32.6(4) mM under a forward bias of equal magnitude

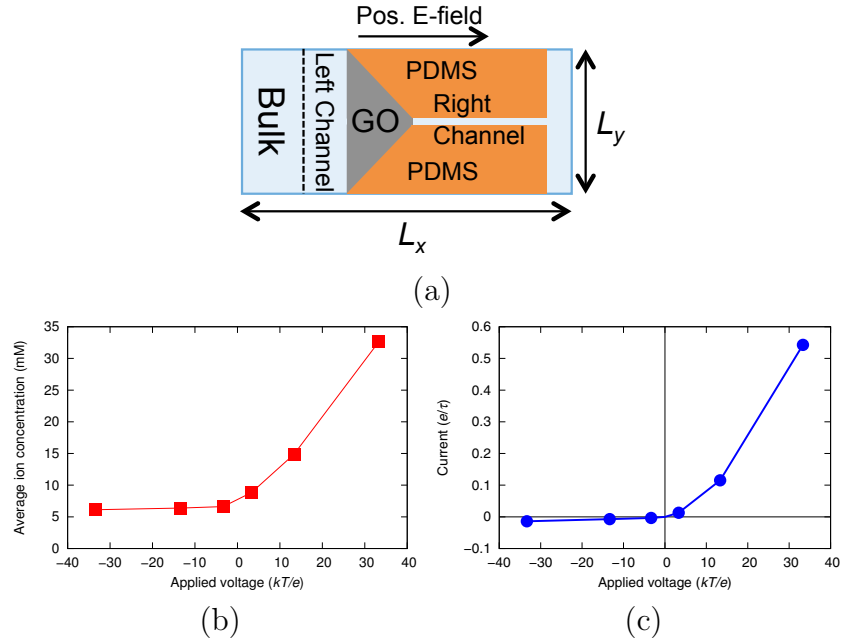


Figure 4.5. A long, narrow channel is introduced on one side of the permselective membrane to induce very high rectification ratios (a). (b) Average ion concentration over 11 independent simulations per voltage. The concentration is the total number of molecules of mobile salt in the system (not including those required to countercharge the GO) normalized by the non-GO, non-PDMS system volume. (c) Average current computed over 11 independent simulations per voltage. We observe a maximum rectification ratio of 60.

(Fig. 4.5b). The resulting systems yield rectification ratios up to 60, which is less than  $r_{\max}$  for reasons discussed above, yet it demonstrates that very high rectification ratios can be engineered by introducing multiple asymmetries into the system (Fig. 4.5c).

### 4.2.3. Conclusion

We have shown that ionic current rectification in a graphene oxide nanochannel network is due to the cation-permselectivity of the NNs and the resulting development of CP regions outside the network. In particular, we have shown that the degree of ICR is affected

by asymmetries in the length of the stagnant zone, the channel cross-sectional area, the diffusion coefficient of the solvent, and/or the bulk salt concentration at either end of the NN, all of which can be readily adjusted in experiment. In addition, the stagnant layer length can be disrupted by hydrodynamics when the system is not embedded in a gel [98], so selectively embedding one of the two NN inlets in a gel can increase ICR, and selective stirring of solvent near an NN inlet can disrupt CP allowing *in situ*-tunable ICR. Furthermore, having established that the ICR behavior of asymmetric GO NNs stems from their cation-permselectivity, it is plausible that other materials can induce ICR, including ion-selective electrodes such as Ag/AgCl, given the system is constructed asymmetrically at the anode and cathode.

The simulated and theoretical models herein agree well without any fit parameters and can be easily tested in experiments. These results are limited in that they do not account for hydrodynamic effects, which fix the length of the stagnant zone and thus the layer length  $\lambda$  [98]. In our model,  $\lambda$  does not emerge from hydrodynamics, but follows from the system geometry. Additionally, the system in this study is  $\sim 100$  nm in length, whereas the experimental systems are macroscopic. The fact that significant rectification is observed in systems of such different sizes shows this method of rectification is highly adaptable to applications across length scales. Advantages of the smaller systems studied here involve faster switching times and less use of reagent, and advantages of the macroscopic systems as in experiment include ease of manufacture and application to bulk solutes. One important note when comparing these systems is that SC has a proportionally larger effect in smaller systems, due to the large electric fields required for comparable CP depletion as in macroscopic systems. Because SC tends to decrease rectification ratios, it could be

advantageous to limit its occurrence by choosing longer channels, though this would also lead to smaller limiting currents.

### 4.3. Simulation methodology

All MD simulations were performed using a modified version of the LAMMPS package [58]. The GO NN and surrounding fluid were modeled by placing varying concentrations of mobile ions in periodically replicated simulation boxes of cross sections  $200 \text{ nm} \times 4.98 \text{ nm}$  and varying lengths, consisting of four lateral sections: a region representing the bulk salt solution of length  $l_{\text{bulk}}$ , a 100 nm GO NN region, and two 100 nm “channels” that are the widths of the GO NN openings and connect either end of the GO NN to the bulk (see, e.g., Fig. 4.4a). Without these channels, the bulk ionic concentration readily diffuses into the CP region from the sides of the NN inlet, greatly reducing the CP effect and effectively eliminating ICR (observed rectification ratios are  $\sim 1.1$ , data not shown). This diffusion does not have a significant effect across macroscopic length scales, and so in experiments [87, 83] rectification can be obtained without channels. For the system with a rectangular GO filter depicted in Fig. 4.2,  $l_{\text{bulk}} = 200 \text{ nm}$ , and the inlet and outlet widths of the GO were both 200 nm. For the systems with a trapezoidal GO filter depicted in Fig. 4.4,  $l_{\text{bulk}} = 50 \text{ nm}$  and the inlet and outlet widths summed to 110 nm so that the area of the GO was constant for different geometric asymmetries. For all systems with asymmetric GO NNs, the CP channels and bulk are initially filled with uniform 7.6 mM salt solution. As the system evolves, CP behavior can locally induce significant ion accretion/depletion, thereby changing the bulk concentration. Since the particle number is kept constant, the concentration in the bulk can vary significantly from

its initial value, resulting in an inaccurate comparison with experimental systems in which the bulk concentration stays constant regardless of bias. As such, a series of simulations were performed in which each system was allowed to reach steady state, then the bulk concentration was adjusted to its correct concentration by randomly inserting or deleting pairs of ions in the bulk region as necessary. This process continued in a loop until the bulk concentration maintained its appropriate value, at which point the particle number was kept at its current value and production began. It should be noted that the voltage required to produce CP that appreciably reduces ionic concentration near a NN inlet is independent of system size, therefore smaller systems require much stronger electric fields, which in turn produce proportionally more SC than in a macroscopic system. As a result, a microscopic system will cause overlimiting currents at lower voltages. A series of repulsive walls restricted the ionic motion, resembling the PDMS barricades in experiment. The interior of the GO NN consisted of 3 flat repulsive planes normal to the  $z$ -axis with a center-to-center distance of 1.66 nm. To model the surface charge of GO, immobile monovalent ions were embedded in the sheets at a surface density of  $0.046 e^-/\text{nm}^2$ , near the upper range for GO [85]. Ions were restricted from crossing the box boundaries in the  $y$ - and  $z$ -directions, but interactions across these boundaries were computed fully, thereby modeling a stack of GO sheets. Coulomb interactions were computed via Particle-Particle Particle-Mesh Ewald summation [65] with a dielectric constant of 80 and relative accuracy of  $10^{-4}$ , and the excluded volumes of the beads and walls were modeled via a purely repulsive shifted-truncated Lennard-Jones potential of diameter  $\sigma = 0.66$  nm, corresponding to the hydrated diameters of  $\text{K}^+$  and  $\text{Cl}^-$  ions, and strength  $\epsilon = 0.83k_{\text{B}}T$ , where the

temperature  $T = 300$  K and Boltzmann constant  $k_B = 1.2\epsilon/300$  K. The solvent was modeled implicitly using a Langevin thermostat with damping time  $0.5\tau$  where  $\tau = \text{nm}\sqrt{m/\epsilon}$  is the simulation unit of time, with  $m$  the average mass of  $\text{K}^+$  and  $\text{Cl}^-$ . The Langevin damping parameter is chosen for efficiency reasons and overestimates the diffusion coefficient  $D$  by a factor  $f = 125$ . The related increase in the mobility  $\nu$  leads to a decrease in the system resistance per Eq. 4.30 and an overestimation of the current  $j$ . However, modifying  $j$  and  $D$  by the same factor has no effect when solving Eqs. 4.1 and 4.2 for  $c$  so the concentration profiles and therefore the behavior of the system are unaffected by this choice other than scaling the current by the factor  $f$ . Simulations progressed with a time step of  $0.005\tau$  and involved roughly  $10^7$  time steps of equilibration and  $10^7$  time steps of production.

## Appendix

Here we derive the resistance across a CP layer only and across a CP and SC layer in series for a system with a nonzero anion leakage current. To do so we repeat the steps in Sec. 4.2.1 without assuming perfect permselectivity of the membrane. Equation 4.7 is

$$(4.32) \quad j'_D + j'_S E x + \partial_x^2 E/k - E^3/2k + \text{const} \cdot E = 0 ,$$

where  $j'_D \equiv j'_+ - j'_-$ ,  $j'_S \equiv j'_+ + j'_-$ , and  $k \equiv 4\pi\lambda_B$ . The third and fourth terms drop out in the CP regime, and we set the  $x$ -coordinate equal to zero at the point that the CP concentration vanishes such that

$$(4.33) \quad E = -j'_D/j'_S x .$$

The SC electric field is given to within a constant by

$$(4.34) \quad \partial_x E = k j'_S / E$$

and at the transition point  $x = x_T$  we assume continuity of the electric field and its derivative so that we can substitute Eq. 4.33 into Eq. 4.34 to yield

$$(4.35) \quad x_T = -(j'_D{}^2 / k j'_S{}^3)^{1/3} .$$

Integrating Eq. 4.34 and setting it equal to Eq. 4.33 at  $x = x_T$  yields the SC electric field

$$(4.36) \quad E = (k j'_D)^{1/3} \sqrt{3 - 2x/x_T} .$$

The CP concentration is given by Eq. 4.11

$$(4.37) \quad c_{\pm, \text{CP}} = -j'_S x / 2$$

and the SC concentration is obtained from Eq. 4.2 assuming the current depends solely on the drift term so that

$$(4.38) \quad c_{\pm, \text{SC}} = \frac{\pm j'_\pm}{(k j'_D)^{1/3} (3 - 2x/x_T)^{1/2}} .$$

The chemical potential drop for the cationic species is then given by Eq. 4.28 as

$$(4.39) \quad \begin{aligned} \beta \Delta \mu_+ = & -\log \left[ \frac{(k j'_D)^{1/3}}{j'_+} \sqrt{1 - 2 \frac{L - L_{\text{CP}}}{x_T}} \right] - \log \left[ \frac{L_{\text{CP}} - x_T}{2} j'_S \right] \\ & - \frac{j'_D}{j'_S} \log \left[ 1 - \frac{L_{\text{CP}}}{x_T} \right] + \frac{j'_D}{3 j'_S} \left[ 1 - \left( 1 - 2 \frac{L - L_{\text{CP}}}{x_T} \right)^{3/2} \right] . \end{aligned}$$

where  $L_{\text{CP}} = \sqrt{j'_S A/4N} + x_T$  for a system with constant  $N$ , as in Fig. 4.2. This is valid while the channel length  $L < L_{\text{CP}}$ . For systems with a CP layer only, we substitute Eq. 4.11 into Eq. 4.1 and integrate obtain

$$(4.40) \quad \beta\Delta\mu_+ = \frac{2j_+}{j'_S} \log \left[ \frac{1 - j'_S\lambda/2c_0}{1 + j'_S\lambda/2c_0} \right].$$

Note that these equations reduce to the results in the Theory section for  $j'_- = 0$ .

## CHAPTER 5

**Conformational behavior of self-attractive sheets with large bending rigidity**

## ABSTRACT

Self-attractive graphene oxide sheets have been observed to wrinkle or partially collapse in spite of their large bending modulus. Contrary to this observation, previous computational and theoretical work has indicated that there is a prohibitive barrier to sheet collapse when the bending modulus of the sheet is greater than the thermal energy, as is the case for graphene oxide. However, these studies neglect the effect of the self-attraction on this barrier. Here we demonstrate how self-attraction of a finite range decreases and even eliminates the barrier to sheet collapse. This is first demonstrated conceptually using a simple mechanical model, then full, self-attractive sheets via free-energy calculations using metadynamics simulations, a free-energy sampling technique. Further, the dynamical and conformational behavior of sheets with large self-attraction is studied using molecular dynamics simulations, which show that the time to collapse can be greatly decreased for modest increases in self-attraction, and that the resulting collapsed conformations exhibit large stochastic fluctuations. For self-attraction sufficient to induce spontaneous collapse, the compactness of the final sheet conformations as measured by the radius of gyration does not show significant dependence on self-attraction.

## 5.1. Introduction

Solution processing of graphite via Hummers' method [103], i.e., inducing significant sheet-sheet repulsion via oxidation, can yield atomically thin graphene oxide (GO) sheets. While cheap to produce, these sheets lack many favorable properties of graphene due to the high density of defects, such as epoxy bridges, hydroxyl groups, and carboxyl groups induced by the oxidation process [104]. These defects can be partially repaired via reduction, resulting in reduced GO and a partial recovery of the properties of pure graphene [105]. However, these defect-sparse, reduced GO sheets are self-attractive and aggregate into clusters [106, 107] that do not exhibit the properties of single sheets [108].

Luo *et al.* showed that GO sheets that are crumpled into fractal balls via capillary compression in evaporating droplets exhibit a reduction in exposed sheet area and thus a decreased propensity to aggregate, while maintaining a significant fraction of electrically active surface area due to their fractal structure [108] resulting in a higher specific capacitance than flat sheets [109]. These crumpled balls were found to have a wide range of applications, e.g., in water treatment [110], industrial lubrication [111], as a battery anode [112], and as a substrate and electron-exchange medium for microbial fuel cells [113].

Preceding this work by two decades were the observations of Wen *et al.* [114], who concluded from small-angle X-ray scattering measurements that graphite oxide, composed of several layers of GO, has the ability to passively crumple in solution without the need for compressive external forces. The accuracy of this statement has been the source of some controversy, as electron micrographs [115] show wrinkled conformations rather than crumpled conformations of the type described in Ref. [114]. Additionally,

theoretical work [116] suggests that a sheet with the bending rigidity of GO provides an insurmountable barrier to wrinkling or crumpling. Motivated by this, we perform simulations of tethered monolayer sheets with a bending modulus  $\kappa_B \gg k_B T$  and an attractive interaction of variable strength between surface sites.

Previous theoretical and computational work concentrating on the phase behavior of such sheets [117, 116] has not predicted sheet collapse when the bending modulus is much greater than  $k_B T$ . In particular, Tallinen *et al.* [116] estimated the barrier for collapse of a self-attractive, continuum sheet as the bending energy required to fold a corner of the sheet, which is roughly ten times the bending modulus. Approximating GO as a continuum sheet with bending modulus  $\kappa_b = 0.5 \text{ eV} = 19k_B T$  at room temperature (see Appendix A) yields an energy barrier of  $\sim 100k_B T$  at room temperature, essentially disallowing spontaneous crumpling or wrinkling in room-temperature solvents, contrary to experimental observations. However, these results do not describe highly self-attractive sheets, as they do not account for the fact that self-attraction of a finite range can reduce the barrier height. Here we illustrate the interplay of bending rigidity and sheet self-attraction first via a simple mechanical model, then present metadynamics simulation results that quantify the barrier to collapse for various degrees of self-attraction. Finally, using molecular dynamics (MD) simulations, we show the kinetic process of collapse for highly attractive sheets and how the self-attraction influences both the time for a sheet to spontaneously collapse and the conformations taken by the collapsed sheets.  $k_B T$ .

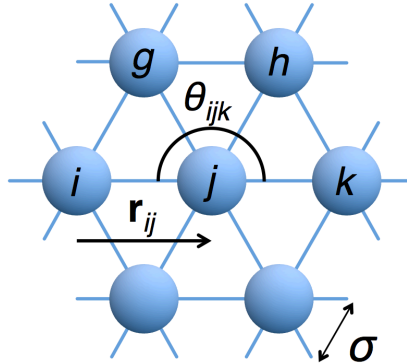


Figure 5.1. Simulation setup. The GO is represented by a triangulated sheet with beads of size  $\sigma$  connected to each nearest neighbor by a harmonic bond (Eq. 5.1). The bending rigidity of the sheet is imposed via angle potentials (Eq. 5.2) between all bonded triplets that form a straight line when the sheet is flat, e.g., between  $(i, j, k)$  but not  $(i, j, g)$  or  $(i, j, h)$  (see Appendix A).

## 5.2. Methods

### 5.2.1. Simulation Model

MD simulations were performed using the LAMMPS package [58]. The GO was modeled by a triangularly connected square sheet (Fig. 5.1) with a side length  $L = 19\sigma$ , with  $\sigma$  the bead size, consisting of  $N = 388$  particles for the metadynamics simulations (Sec. 5.3.2) and  $L = 70\sigma$  with  $N = 5710$  for the MD simulations (Sec. 5.3.3). Notably, the present length-to-thickness ratios (equal to  $L$  for each sheet) are much smaller than in experimental GO sheets, which are microns in length and nanometers thick. The sheet was placed in a periodically replicated simulation box with side lengths at least twice the sheet side length to prevent interaction between the sheet and its periodic images, thereby modeling a sheet in the dilute limit. The self-attraction and excluded volume of the sheet were modeled via Lennard-Jones interactions  $U_{LJ}$  of strength  $\epsilon_{LJ}$  between all non-bonded pairs of beads. For computational efficiency, this potential is truncated at  $r_{\text{cut}} = 2.5\sigma$  and then

shifted by  $U_{\text{LJ}}(r_{\text{cut}})$  to avoid discontinuities in the potential. The areal compressibility of the sheet was modeled with a harmonic bond potential between all nearest neighbors  $(i, j)$  of the form

$$(5.1) \quad U_{\text{bond}}(r_{ij}) = \epsilon_{\text{bond}} (r_{ij} - \sigma)^2 ,$$

where  $r_{ij}$  is the distance between two bonded particles (Fig. 5.1). The bond energy  $\epsilon_{\text{bond}} = 2000k_{\text{B}}T$  is chosen to be at least 100 times larger than both the bending modulus  $\kappa_{\text{b}} = 0.5 \text{ eV}$  (see Appendix A) and  $\epsilon_{\text{LJ}}$ , to ensure the sheet’s dynamics are mostly determined by bending and self-attraction. The bending rigidity was modeled by a “cosine–delta” angle potential of the form

$$(5.2) \quad U_{\text{CD}}(\theta_{ijk}) = \epsilon_{\text{CD}} [1 - \cos(\pi - \theta_{ijk})]$$

for all sets of three beads  $(i, j, k)$  such that  $i$  and  $k$  are nearest neighbors of  $j$ , and the vectors  $\mathbf{r}_{ij}$  and  $\mathbf{r}_{jk}$  are collinear when the sheet is flat (see Fig. 5.1). This form is chosen to approximate the bending properties of a continuum sheet, and the prefactor  $\epsilon_{\text{CD}}$  is set to  $14.8k_{\text{B}}T$  to approximate the bending rigidity of GO (see Appendix A for a discussion of the choice of angle potential). The solvent is modeled implicitly by a Langevin thermostat with damping time  $6.67\tau$  where  $\tau = \sigma\sqrt{m/k_{\text{B}}T}$  is the simulation unit of time, with the simulation mass  $m$  set to unity. This thermostat also controls the temperature  $T = \epsilon/k_{\text{B}}$  of the runs. Using an implicit solvent neglects hydrodynamics, which has no effect on the equilibrium metadynamics simulations of Sec. 5.3.2, but may affect the folding process of dynamically collapsing sheets and therefore the final conformations taken by such sheets. The onset of sheet collapse, however, should not be affected by hydrodynamic interactions

between sheet sites, because the sheet conformation is static prior to collapse, as shown in Sec. 5.3.3. This static period is followed by a rapid collapse to a compact state (see Sec. 5.3.3). To accurately integrate the equations of motion during the collapse, The MD simulations evolved with a maximum time step of  $0.00667\tau$  that was adjusted dynamically every 100 time steps so that no particle moved more than  $0.01\sigma$  on that time step. Time dependence of the dynamics was monitored by recording the simulation time  $t$  at each time step. The simulations evolved for a total of  $5 \times 10^7$  time steps.

### 5.2.2. Metadynamics

Whereas the potential-energy landscape is useful in determining the conformational behavior of a sheet, it does not take into account configurational entropy and so yields an incomplete description of the sheet's thermodynamic behavior. For this reason we map the free energy using metadynamics simulations [118], performed with the LAMMPS package using the Collective Variables module [119]. Metadynamics biases the motion along a set of  $N_{CV}$  degrees of freedom  $\boldsymbol{\xi} = (\xi_1, \xi_2, \dots, \xi_{N_{CV}})$ , known as collective variables (CVs), using a history-dependent potential that consists of  $N_{CV}$ -dimensional, repulsive Gaussians that are periodically deposited at the system's CV coordinates, i.e.,

$$(5.3) \quad V_{\text{meta}}(\boldsymbol{\xi}) = \sum_{t'=\delta t, 2\delta t, \dots}^t W \prod_{i=1}^{N_{CV}} \exp \left[ -\frac{(\xi_i(t) - \xi_i(t'))^2}{2\delta_{\xi_i}^2} \right],$$

where  $\delta t = 10$  time steps is the time between depositions,  $W$  is the height of the deposited Gaussian, which varies between simulations and is given in Sec. 5.3, and  $\delta_{\xi_i}$  is the width of the Gaussian in the direction of  $\xi_i$ . This bias is imposed by adding a force  $-\nabla_i V_{\text{meta}}$  to each particle  $i$  during each time step, where  $\nabla_i$  is the gradient with respect to the position

$\boldsymbol{\xi}$  of particle  $i$ . The simulation sequentially evolves toward configurations that minimize the *effective*, biased free energy  $\tilde{F}(\boldsymbol{\xi}) = F(\boldsymbol{\xi}) + V_{\text{meta}}(\boldsymbol{\xi})$ , where  $F(\boldsymbol{\xi})$  is the unbiased free energy, then adds a repulsive Gaussian potential at the resulting value of  $\boldsymbol{\xi}$  to bias the system away from  $\boldsymbol{\xi}$ . This process allows the system to sample configurations with large free energies compared to the free-energy minimum of the system and additionally yields  $F(\boldsymbol{\xi})$  to within an unknown constant

$$(5.4) \quad F(\boldsymbol{\xi}) = -V_{\text{meta}}(\boldsymbol{\xi}) + \text{const.}$$

The CVs were chosen to sample the free energy as both a function of sheet compactness and the number of sheet–sheet contacts. Accordingly, we used the radius of gyration  $R_G$ , defined as the second moment of the inertia tensor,

$$(5.5) \quad R_G^2 = \frac{1}{N} \sum_i^N \mathbf{r}_i^2 - \left( \frac{1}{N} \sum_i^N \mathbf{r}_i \right)^2,$$

where  $\mathbf{r}_i$  is the position of the  $i$ th particle, and the coordination number

$$(5.6) \quad C = \sum_{j>i}^N \frac{1 - (|\mathbf{r}_i - \mathbf{r}_j|/d_0)^n}{1 - (|\mathbf{r}_i - \mathbf{r}_j|/d_0)^m},$$

characterized by a cutoff value  $d_0$  and exponents  $m$  and  $n$  with  $m > n$ . Each particle pair contributes a value of 1 to the coordination number when the interparticle distance  $|\mathbf{r}_i - \mathbf{r}_j| \ll d_0$  and a value of 0 when  $|\mathbf{r}_i - \mathbf{r}_j| \gg d_0$ , with the smoothness of the transition between these values determined by the exponents  $m$  and  $n$  (Fig. 5.2). Together, the values of  $d_0$ ,  $m$ , and  $n$  determine a balance between the resolution of the resulting free-energy landscape and the smoothness of the CV, the latter of which is required so that

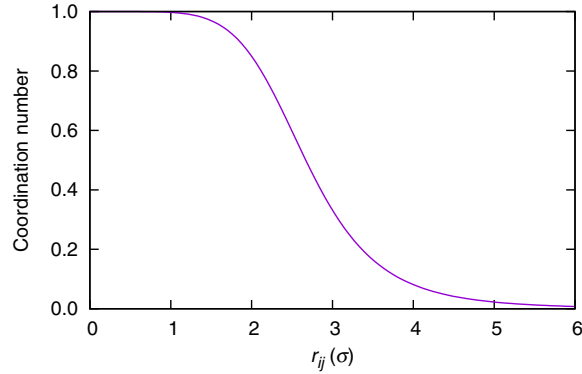


Figure 5.2. The coordination number  $C$  (Eq. 5.6) per particle pair transitions from 1 at interparticle separation  $r_{ij} \ll d_0$  to 0 at  $r_{ij} \gg d_0$ , and is 0.5 at the cutoff  $r_{ij} = d_0 = 2.67$ . The choice of exponents  $m = 12$  and  $n = 6$  ensures a smooth decay to zero, which is required so that metadynamics can compute gradients of  $C$  with respect to particle positions to impose biasing forces  $\phi$  on the particles.

metadynamics imposes a finite force  $\phi_i$  on particle  $i$  for all particle positions. For this system,  $d_0 = 2.67$ ,  $m = 12$ , and  $n = 6$  were empirically found to yield good definition of the resulting free-energy landscape. Data was collected in bins of  $0.0067\sigma$  along  $R_G$  and 10 along  $C$ , and the widths of the Gaussian metadynamics potentials were  $\delta_{R_G} = 0.025\sigma$  and  $\delta_C = 37.6$ . The error in relative values of the free energy was estimated by observing the reported free-energy difference between two spatially uncorrelated points as the metadynamics simulations progressed and measuring the size of the fluctuations over time.

### 5.3. Results and Discussion

#### 5.3.1. Effect of self-attraction on the kinetic barrier to collapse

The energy barrier to sheet collapse  $\approx 10\kappa_b$  obtained in Ref. [116], equal to the bending energy required to curl a sheet corner over until sheet-sheet contact is made, is independent of the size of the curl and thus provides an energetic barrier that depends only on the intrinsic bending stiffness of the sheet. The estimated bending modulus of GO  $\kappa_b = 0.5$  eV (see last paragraph of Appendix A) yields a barrier  $\sim 100k_B T$ , forbidding passive transitions between flat and collapsed states. This calculation disregards the energetic gain due to sheet self-attraction *during* the folding process by assuming this attraction is infinitely short ranged. Incorporating finite-ranged self-attraction leads to a significant reduction in the energetic barrier to collapse. This can be understood using a simple model consisting of three stiffly bonded beads in an initially linear configuration, with nonzero bending stiffness and an attractive interaction between the two end beads (Fig. 5.3a, inset). The bending stiffness  $U_{CD}(\theta_{abc})$  (Eq. 5.2) is associated with the angle  $\theta_{abc}$  between the three beads and favors a straight configuration. It is in competition with a bead-bead attraction, which here we approximate as only the attractive part of the Lennard-Jones interaction, i.e.,

$$(5.7) \quad U_{LJ}(r_{ij}) = -4\epsilon_{LJ} \left( \frac{\sigma}{r_{ij}} \right)^6 .$$

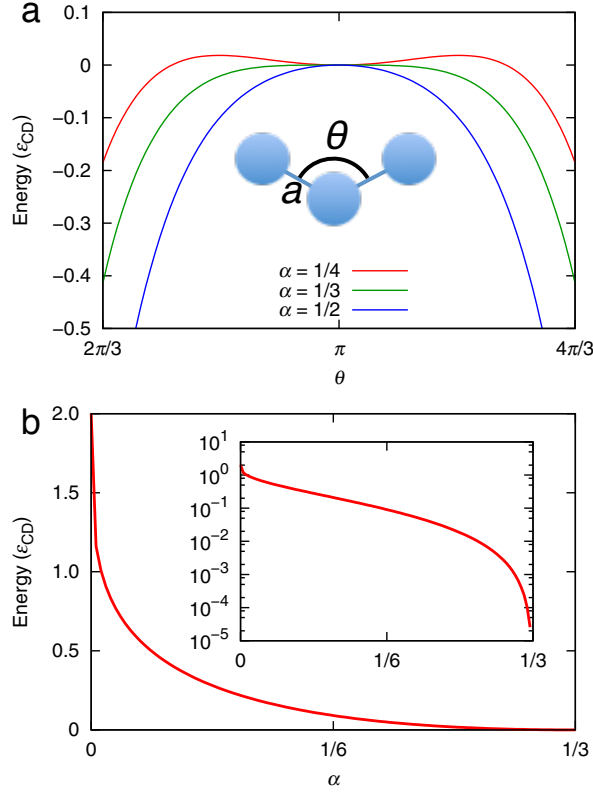


Figure 5.3. A simplified description of a folding sheet consists of ball-and-stick model with fixed bond lengths  $a$  and a variable angle  $\theta_{abc}$  (a, inset). The competition between self-attraction and bending is characterized by the parameter  $\alpha = k\epsilon_{LJ}/\epsilon_{CD}$  per Eq. 5.8. The straight configuration ( $\theta = \pi$ ) is metastable for  $\alpha = 1/4$  and unstable for  $\alpha \geq 1/3$  (a). Accordingly, the barrier energy to escape the metastable flat phase decreases sharply from  $U_0 = 2\epsilon_{CD}$  for  $\alpha = 0$  to half that value for  $\alpha \approx 0.007$ , and vanishes for  $\alpha = 1/3$  (b). The decay to zero can be seen more clearly on a semilog plot (b, inset).

This approximation simplifies the resulting expressions and is valid near the flat configuration when the end beads are far apart. The total energy of this system is

$$(5.8) \quad U_{\text{tot}} = \frac{1}{2}U_0 \left[ 1 - \cos(\pi - \theta_{abc}) - \frac{2\alpha}{\sin^6(\theta_{abc}/2)} \right],$$

where  $U_0 = 2\epsilon_{\text{CD}}$  is the barrier energy when there is no self-attraction (corresponding to the assumption of Ref. [116]), and  $\alpha \equiv k \frac{\epsilon_{\text{LJ}}}{\epsilon_{\text{CD}}}$  quantifies the competition between self-attraction and bending rigidity, with the parameter  $k = 2 \left(\frac{\sigma}{2a}\right)^6$  for the present system, where  $a$  is the lattice parameter. This expression for  $k$  shows a significant dependence on the range of the self attraction  $\sigma$ . Increasing  $\alpha$  illustrates the effect that large self-attractions have on the barrier energy (Fig. 5.3a). For  $\alpha = 1/4$ , the barrier has been reduced to 1% of the total folding energy, whereas for  $\alpha = 1/3$  and  $\alpha = 1/2$  there is no barrier to folding. The barrier energy can be calculated by extremizing Eq. 5.8, yielding the critical angle to folding  $\theta_{\text{C}} = 2 \sin^{-1} \sqrt[8]{3\alpha}$  and

$$(5.9) \quad U_{\text{barrier}} = U(\theta_{\text{C}}) - U(\pi) = U_0 \left[ 1 - \frac{4}{3} \sqrt[4]{3\alpha} + \alpha \right].$$

This is  $U_0$  at  $\alpha = 0$  and decreases with increasing  $\alpha$  until vanishing at  $\alpha = \frac{1}{3}$  (Fig. 5.3b), demonstrating how a finite-range attraction can reduce and even eliminate kinetic barriers to sheet collapse. Applying this model to a related system in which a sheet folds along fault lines as observed in Ref. [120] (Appendix B) shows how the parameter  $k$  increases from the present model to that of a folding sheet, and demonstrates that Eq. 5.9 can be used to describe larger, more complex systems despite the simplicity of the system for which it was derived.

### 5.3.2. Energy barriers to folding

To understand the folding process of a self-attractive sheet, metadynamics simulations were performed with  $\epsilon_{\text{LJ}} = k_{\text{B}}T$  and the collective variables described in Sec. 3.2. The system evolved for 30 million time steps with a weight  $W = 10k_{\text{B}}T$  and 20 million more

time steps with  $W = k_B T$ , yielding a final observed uncertainty of  $20k_B T$  in energy differences between uncorrelated points on the free-energy map. The simulations show a rich free-energy landscape (Fig. 5.4a) with points b–i corresponding to the conformations pictured in Figs. 5.4b–i. The two points with lowest free-energy, points b and f in Fig. 5.4a, correspond to a flat sheet and a sheet folded once lengthwise, respectively (Figs. 5.4b and f). At this  $\epsilon_{LJ}$ , the free-energy difference between states b = (4980, 7.4 $\sigma$ ) and f = (8700, 5.9 $\sigma$ ), located to within an accuracy of (10, 0.1 $\sigma$ ), is  $\Delta V_{bf} = V_f - V_b = 260k_B T$ , so the flat phase is heavily thermodynamically favored. Further, the lowest-energy transition between these states is set by the saddle-point energy at point d = (6080, 6.1 $\sigma$ ) giving  $\Delta V_{db} = 390k_B T$  and  $\Delta V_{df} = 140k_B T$ . Since the barrier in both directions is much larger than  $k_B T$ , the final conformations taken by the sheet are determined by the initial state of the system so that a crumpled sheet will not spontaneously uncrumple and *vice versa*.

Weak self-attraction requires sheet–sheet contact before the self-attraction becomes significant, as shown by the saddle-point configuration Fig. 5.4d. In the simple mechanical model above, strong self-attraction can have an effect well before sheet–sheet contact is made. Accordingly, metadynamics simulations were performed for  $\epsilon_{LJ} = 5k_B T$ ,  $10k_B T$ ,  $15k_B T$ , and  $20k_B T$ . Because such strong self-attractions can condense the system to very low free-energy minima, and because the cost of a metadynamics simulation is related to the volume of the phase space that must be filled with repulsive Gaussians (Sec. 5.3.2), which is much larger here than for  $\epsilon_{LJ} = k_B T$ , exploring the landscape fully as in Fig. 5.4a can be computationally costly. To study how  $\epsilon_{LJ}$  affects the energetic barrier to collapse without incurring the cost of these deep energetic wells, we bias the simulation toward its

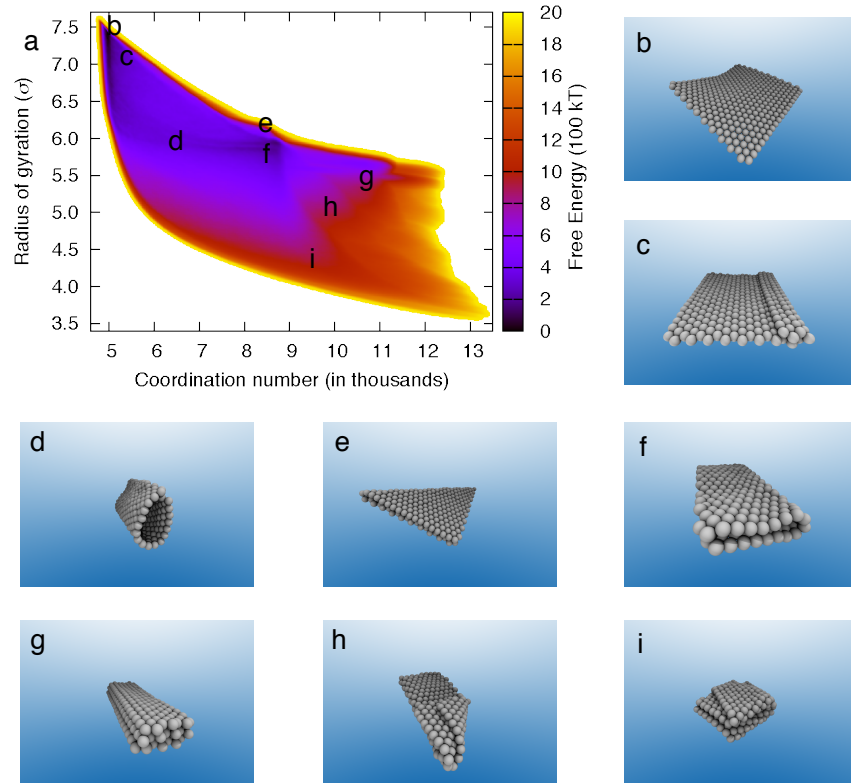


Figure 5.4. Free-energy map and associated configurations for  $\epsilon_{LJ} = k_B T$ . Metadynamics simulations yield the free energy as a function of the radius of gyration (Eq. 5.5) and coordination number (Eq. 5.6) (a). Points on the map indicated in black lettering correspond to the configurations (b)–(i). Flat sheets exhibit a large radius of gyration and small coordination number (b). At this value of  $\epsilon_{LJ}$ , the sheet can condense either by curling over one edge (c) or more favorably by bending evenly across the middle of the sheet (d). As a result, the sheet can fold along its diagonal (e) or more favorably along its center line (f). The sheet can further compact itself by folding in thirds (g), folding configuration f at its corner (h), or folding configuration f along its short axis (i). For  $\epsilon_{LJ} = k_B T$ , the energy minimum (b) is the ground state, and the barrier between (b) and the local minimum (f) is  $260 \pm 20 k_B T$ . Configurations to the left or right of point d (a) will move toward points b or f, respectively. The value of  $\epsilon_{LJ}$  does not affect the correspondence between points (b)–(i) in (a) and the pictured configurations (b)–(i), but it may affect the relative free energies of those points.

flat configuration with a harmonic potential

$$(5.10) \quad V_{\text{harm}}(R_G, C) = \frac{1}{2} [k_1 (R_G - R_{G,0})^2 + k_2 (C - C_0)^2] ,$$

where  $k_1 = 4444k_B T/\sigma^{-2}$  and  $k_2 = 10^{-2}k_B T$  are spring constants and the potential minimum is at  $R_{G,0} = 7.3\sigma$  and  $C_0 = 5000$ . The free-energy landscape of the system is then obtained from the metadynamics results by subtracting  $V_{\text{harm}}$  from the bias potential  $V_{\text{meta}}$ , Eq. 5.3 (Fig. 5.5). These simulations progressed for 5 million time steps with weight  $W = k_B T$  and then one million more time steps with  $W = 0.1k_B T$ , giving a final uncertainty of  $10k_B T$ . The preferred folding mode indicated by the saddle points of Figs. 5.5a and b is seen to shift from an even fold across the middle (Fig. 5.4d) to a sharp fold of an edge or corner (Fig. 5.4c) as the self-attraction is now strong enough that small amounts of sheet-sheet contact can offset large bending energies. As in the simplistic mechanical ball-and-stick model above, there is a clear decrease in the energetic barrier as  $\epsilon_{\text{LJ}}$  increases, until the barrier is comparable to or smaller than the statistical uncertainty for  $\epsilon_{\text{LJ}} \geq 15k_B T$ . This decreasing barrier to collapse has a direct effect on the dynamics and conformations of the collapsed sheets that result.

### 5.3.3. Dynamics of sheet collapse

For sheets with self-attraction sufficient to induce spontaneous collapse, the final conformations taken will not necessarily resemble any of the the local free-energy minima in Fig. 5.4a. Instead, local *potential*-energy minima can trap the system so that the final morphology depends on the dynamical time-evolution of the sheet rather than the location of free-energy minima. As such, we perform MD simulations of a system similar to

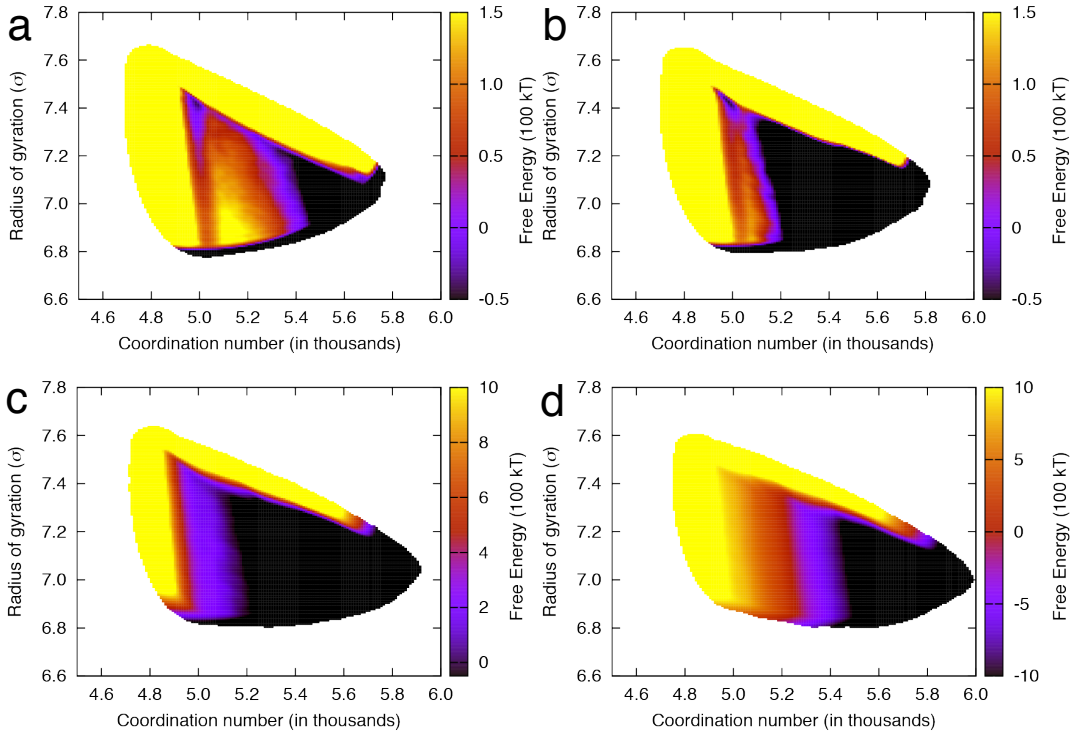


Figure 5.5. Free-energy maps illustrate how increasing self-attraction affects the free-energy landscape. For  $\epsilon_{\text{LJ}} = 5k_{\text{B}}T$  (a) and  $\epsilon_{\text{LJ}} = 10k_{\text{B}}T$  (b), an energetic barrier on the order of  $100k_{\text{B}}T$  is observed. For higher self-attractions  $\epsilon_{\text{LJ}} = 15k_{\text{B}}T$  (c) and  $\epsilon_{\text{LJ}} = 20k_{\text{B}}T$  (d) the barriers are comparable to or below the uncertainty  $10k_{\text{B}}T$  of the metadynamics simulations and cannot be observed. The simulations are constrained using a harmonic potential (Eq. 5.10) so that they do not explore the areas in white. Note that the values of the color bar have been shifted between plots for visual clarity.

but larger than that in the previous section ( $L = 70\sigma$ ) and monitor the sheet morphology as a function of time and the degree of self-attraction. In experiment, the latter of these can be altered by changing the solvent in which the GO is dispersed [115].

The flat phase persists for a finite duration  $t_{\text{coll}}$  before collapse, which depends on the self-attraction. This is followed by a sharp transition to a compact conformation (Fig. 5.6a). The process of collapse is stochastic in nature, so average behavior and

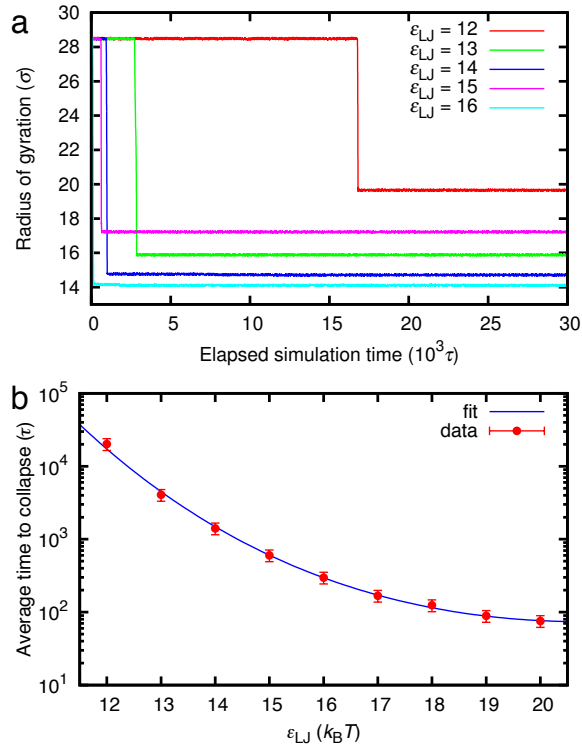


Figure 5.6. The metastability of the flat phase at the self-attractions  $\epsilon_{LJ}$  examined manifests itself as a finite time  $t_{\text{coll}}$  during which the system remains at its initial  $R_G$  followed by a relatively quick collapse to a more compact conformation (a). Averages over 30 simulations show that the time to collapse decreases slower than exponentially with respect to  $\epsilon_{LJ}$ , indicating the associated energy barrier decreases more slowly than a linear function. This is in agreement with Eq. 5.9 obtained for a simplified ball-and-stick model (b). Fitting the average of  $t_{\text{coll}}$  to an Arrhenius function of the form Eq. 5.11 yields inferences about the preferred folding mode, the competition between bending stiffness and self-attraction during a fold, and the attempted frequency of a fold (see text).

associated statistical uncertainties are obtained from 30 identical simulations per  $\epsilon_{LJ}$ , each with different random-number seeds. The time to collapse is observed to be a smoothly decreasing function of  $\epsilon_{LJ}$  (Fig. 5.6b). This corroborates the findings in Sec. 5.3.1 in which increasing sheet self-attraction decreases the barrier to collapse. Additionally, this

decrease is slower than exponential in  $\epsilon_{\text{LJ}}$ , indicating that the associated energy barrier decreases more slowly than a linear function of  $\epsilon_{\text{LJ}}$ , in agreement with Eq. 5.9 for the ball-and-stick model (Fig. 5.3b). Because the simplistic ball-and-stick model can describe hinge-like folding of a large sheet with reasonable success (see Appendix B), we attempt to use it here as an approximate model of the sheet barrier energy. Accordingly, we describe the barrier energy to collapse,  $U_{\text{barrier}}$ , by Eq. 5.9 and relate this energy to  $t_{\text{coll}}$  via an Arrhenius function

$$(5.11) \quad t_{\text{coll}} = A^{-1} \exp(U_{\text{barrier}}/k_{\text{B}}T) ,$$

where  $A$  represents the attempt frequency and  $U_{\text{barrier}}$  is characterized by a bending energy  $U_0$  and the parameter  $k$ , both of which are used here as fitting parameters. A nonlinear least-squares fit yields  $A = 1.35(5) \times 10^{-2} \tau^{-1}$ ,  $U_0 = 180(8)k_{\text{B}}T$ , and  $k = 0.237(3)$ , with reduced  $\chi^2 = 0.35$  indicating a good fit. The value obtained for  $U_0$ , which represents the folding energy in the absence of attractive interactions, is roughly twice smaller than the energy barrier obtained from metadynamics simulations of Fig. 5.3.2 (Sec. 5.3.2). This is consistent with the fact that, in contrast with the case where  $\epsilon_{\text{LJ}} = k_{\text{B}}T$  in which the sheet folds along its center line (Fig. 5.4d), the preferred folding mode for  $\epsilon_{\text{LJ}} \gg k_{\text{B}}T$  is along sheet edges or corners (Fig. 5.4c), in agreement with the results of Fig. 5.5 and configurations observed in simulations at the onset of folding (data not shown). This value of  $U_0 \approx 10\kappa_{\text{b}}$  is consistent with the energy calculated for folding of sheet corners in Ref. [116]. The value of  $k$  suggests a critical self-attraction  $\epsilon_{\text{LJ,crit}} = 1.58\epsilon_{\text{CD}}$ . This is smaller than that of both the simplified ball-and-stick (Sec. 5.3.1) and sheet–hinge models (Appendix B), indicating that the preferred folding mode has a smaller bending energy

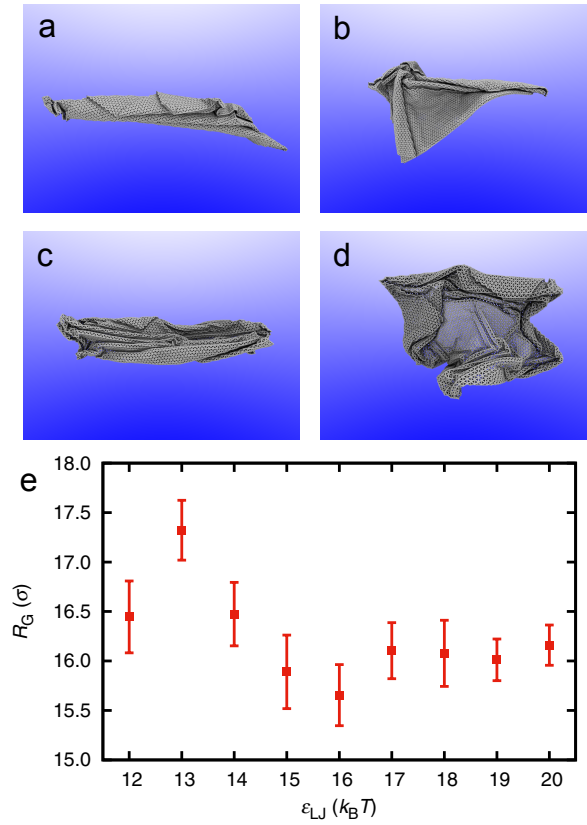


Figure 5.7. Collapsed conformations for various degrees of self-attraction. Two main modes of collapse are depicted at  $\epsilon_{LJ} = 12k_B T$  (a and b), and  $\epsilon_{LJ} = 20k_B T$  (c and d), corresponding to the lowest  $\epsilon_{LJ}$  for which spontaneous sheet collapse is observed and the highest  $\epsilon_{LJ}$  simulated, respectively. Sheet collapse along multiple directions stabilizes a flat phase that resists further collapse (a and c), and a sheet collapse along one main direction leads to rod-like conformations (b and d). These are both common across the various  $\epsilon_{LJ}$  observed here, so that the radius of gyration averaged across 30 independent simulation per  $\epsilon_{LJ}$  varies weakly with  $\epsilon_{LJ}$  (e).

than the sharp folds considered in the simplified models. Lastly, the value of the attempt frequency  $A$  suggests there is a fluctuation of order  $k_B T$  in this preferred mode roughly once every  $70\tau$ .

The conformations assumed after “collapse” (Fig. 5.7a–d) do not correspond to the

single folds represented by the free-energy minima in Fig. 5.4a (e.g., Figs. 5.4b and f), but instead correspond to “trapped” states that the sheets remain in. Additionally, the average  $R_G$  of the sheets depends only very weakly on their self-attraction (Fig. 5.7e). Instead, there is large stochastic variation for each  $\epsilon_{LJ}$  that depends on whether folding occurs along one direction as in Figs. 5.7a and c, leading to straight, rod-like collapsed states, or multiple directions as in Figs. 5.7b and d, leading to states that exhibit some degree of flatness like the conformations observed in experiment [115, 121, 122, 123]. The probability of folding along multiple axes is likely influenced by the sheet size, and given that experimental GO sheets can exhibit length:thickness ratios roughly two orders of magnitude larger than that simulated here, further study may require a systematic investigation of finite-size effects in this system. Additionally, this model does not incorporate sites of reduced bending rigidity observed in Ref. [120] that may increase the probability of folding along multiple lines.

#### 5.4. Conclusion

Analysis of a coarse-grained model of graphene-oxide sheets has shown that sheet self-attraction competes with bending stiffness to reduce the energy barrier to collapse. This was quantified first using a simplified mechanical model, which showed that the barrier energy is reduced to zero for sufficient self-attraction of the sheet, and was elucidated further using metadynamics simulations that showed that an energetic barrier to collapse of  $\sim 100k_B T$  is reduced or eliminated when the self-attraction is  $\sim 10k_B T$ . Further, the average waiting time to observe spontaneous sheet collapse in molecular dynamics simulations was related to the expression for the energy barrier obtained from the simple

ball-and-stick model via an Arrhenius equation. The final sheet conformations showed large run-to-run variation due to the stochastic nature of the collapse. Sheets collapsed either along one axis, forming rod-like conformations, or along multiple axes, stabilizing a wrinkled sheet-like structure. Because multiple folding modes may become more likely for larger sheets, and because GO sheets in experiment are roughly 2 orders of magnitude larger than in simulation, a possible extension to this work includes quantifying how collapsed conformations depend on sheet size. Further, experimental evidence [120] indicates that defect lines may play an important role in the folding behavior of GO, and further work that incorporates such defects may more faithfully capture the wrinkled conformations observed in experiment.

### Appendix A: Choice of angle potential

Continuum elasticity theory gives the bending energy of a sheet via the Helfrich Hamiltonian [124]

$$(5.12) \quad E_{\text{bend}} = \int_A dA \left( \frac{1}{2} \kappa_b K^2 + \kappa_G K_G \right) ,$$

where the integral is taken over an area  $A$ , with  $\kappa_b$  the bending modulus,  $K$  the curvature,  $\kappa_G$  the Gaussian bending rigidity, and  $K_G$  the Gaussian curvature.

Since the curvature of a surface is given by the rate of change of the surface normal vector, the first term in Eq. 5.12 is often described in discrete models by

$$(5.13) \quad U_{\text{NN}} = \epsilon_{\text{NN}} \sum_{\text{pairs}} [1 - \mathbf{n}_a \cdot \mathbf{n}_b] ,$$

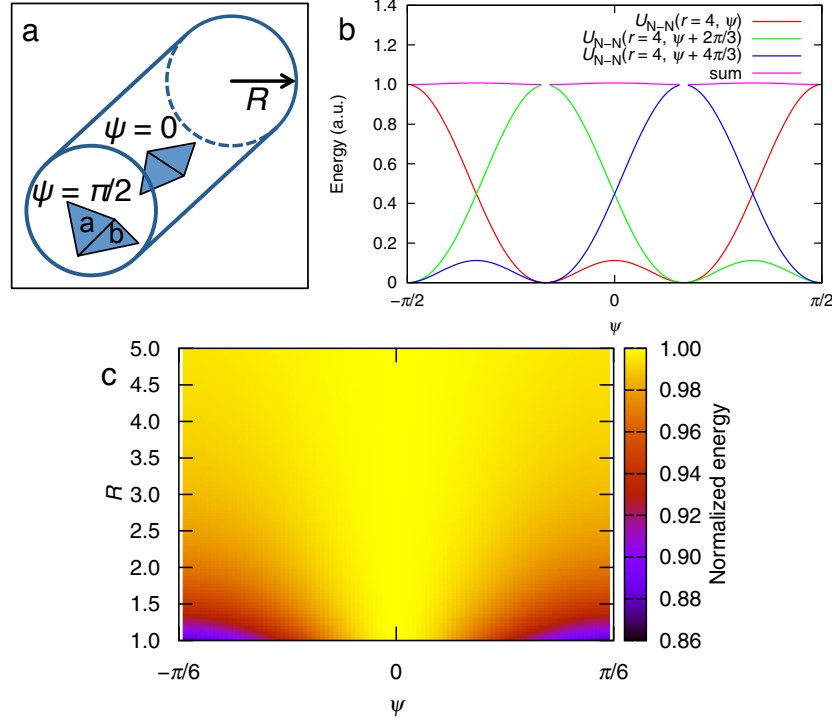


Figure 5.8. To compare the “Normal–Normal” bending rigidity  $\epsilon_{\text{NN}}$  of a coarse-grained, triangulated sheet (Eq. 5.13) with the bending modulus  $\kappa_b$  of a continuum sheet (Eq. 5.12), we compute the bending energy of a triangulated sheet curled into a cylinder of radius  $R$ , given that the vertices of the triangles (corresponding to coarse-grained beads) are constrained to the surface of the cylinder (a). This energy varies with the angle  $\psi$  that the center-to-center vector of the triangles makes with the cylinder axis (b, red curve). Each triangle is bonded to three nearest neighbors (b, red, green and blue curves) so that the total energy per triangle is given by their sum (b, purple curve), which varies as a function of  $\psi$ . This variation increases as the radius of curvature decreases, and is  $\sim 10\%$  of the total bending energy for  $R = \sigma$ , which can be sufficient to impose directional bias upon folding (c).

where  $\mathbf{n}_a$  and  $\mathbf{n}_b$  are the unit normals of surfaces a and b that share an edge (see Fig. 5.8a) and  $\epsilon_{\text{NN}}$  is related to the bending modulus  $\kappa_b$ . The relation of  $\epsilon_{\text{NN}}$  to  $\kappa_b$  is obtained by calculating the bending energy of a triangulated surface curled into a cylinder. Since a cylinder has constant  $K = 1/R$  where  $R$  is the radius of the cylinder, and constant

$K_G = 0$ , the bending energy of the cylinder per unit area is simply  $\frac{1}{2}\kappa_b/R^2$ . For two adjacent triangles whose vertices lie on the surface of a cylinder of radius  $R$ , the bending energy per triangle is a function of  $R$  as well as the angle of rotation on the cylinder surface  $\psi$  (see Fig. 5.8a)

$$(5.14) \quad U_{\text{NN}}(R, \psi) = \frac{1}{2} - \frac{\sqrt{(16R^2/\sigma^2 - 4c^2)(3c^2 - s^2)s^2 - c^2 + (8R^2/\sigma^2 - 1)^2 - 128R^2/\sigma^2 + 25}}{3c^4},$$

where  $c \equiv \cos \psi$  and  $s \equiv \sin \psi$ , and we have assumed the lattice vector is  $\sigma$ . The bending energy changes with  $\psi$  (red curve in Fig. 5.8b) from a maximum value at  $\psi = \pm\pi/2$  to zero at  $\psi = \pm\pi/6$ . Since each triangle has three nearest neighbors, with angles  $\psi$  offset by  $2\pi/3$  from one another (green and blue curves, Fig. 5.8b), the total energy of a single triangle will be the sum of the associated energies (purple curve, Fig. 5.8b). While variations in this energy as a function of  $\psi$  are small compared to the total bending energy, they can be sufficient to impose a directional preference for folding. Additionally, these variations grow with decreasing  $R$ , such that for  $R \sim \sigma$ , which is roughly the radius of curvature of a sharp fold in a sheet of unit thickness, the fluctuations are  $\sim 10\%$  of the total energy (Fig. 5.8c).

An alternative is to use the bond-angle potential  $U_{\text{CD}}$  (Eq. 5.2). Placing the vertices of a triangulated sheet on the surface of a cylinder and calculating the bending energy as above yields

$$(5.15) \quad U_{\text{CD}}(R, \psi) = \epsilon_{\text{CD}} \frac{\cos^4 \psi}{2R^2/\sigma^2},$$

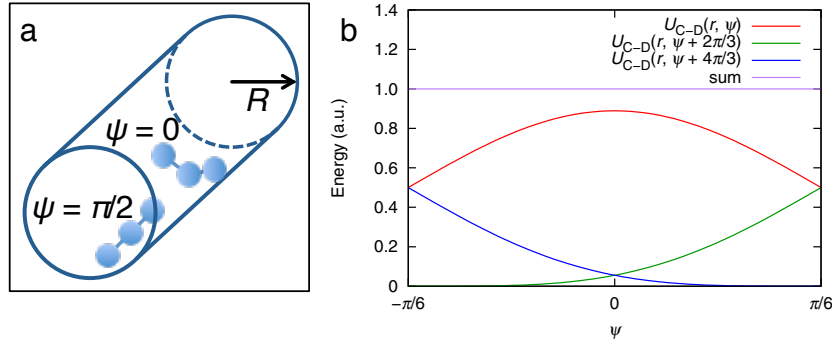


Figure 5.9. Similarly to Fig. 5.8, we compare the “cosine–delta” bending rigidity  $\epsilon_{\text{CD}}$  of a coarse-grained, triangulated sheet (Eq. 5.2) with the bending modulus  $\kappa_{\text{b}}$  of a continuum sheet. The total bending energy of the triangulated sheet is obtained by constraining each vertex (corresponding to a coarse-grained bead) to the surface of a cylinder of radius  $R$ , then calculating the bending energy between three vertices  $i$ ,  $j$ , and  $k$  (see Fig. 5.1) using Eq. 5.2 (a). This energy varies with the angle  $\psi$  that the vertex-to-vertex vector makes with the cylinder cross-section (b, red curve). Each vertex is the center of three such bonds  $i$ ,  $j$ ,  $k$  (b, red, green and blue curves) so that the total energy per vertex is given by the sum of the associated bending energies (b, purple curve). There is no variation in the total bending energy with respect to  $\psi$ , such that Eq. 5.2 adequately reproduces the bending energy of a continuum sheet in this regard.

with  $R$  and  $\psi$  as above (Fig. 5.9a). Again, the total bending energy per vertex is composed of the bending energy of three bonds with  $\psi$  offset by  $2\pi/3$  from one another (red, blue and green curves, Fig. 5.9b)

$$(5.16) \quad U_{\text{CD,tot}}(R, \psi) = \frac{9}{16} \frac{\epsilon_{\text{CD}}}{R^2/\sigma^2},$$

which is constant with respect to  $\psi$  (purple curve, Fig. 5.9b), and only depends on  $1/R^2$ , in direct analogy to a continuum sheet. We are unaware of evidence of a directional preference for the folding of graphene or GO, so we opt for  $U_{\text{CD}}$  as opposed to  $U_{\text{NN}}$ .

To calibrate  $\epsilon_{\text{CD}}$  we compare the energy per vertex Eq. 5.16 with the Helfrich bending energy (Eq. 5.12) integrated over the area occupied by a vertex,  $\sqrt{3}\sigma^2/2$ , yielding

$$(5.17) \quad \epsilon_{\text{CD}} = \frac{4}{\sqrt{27}} \kappa_{\text{b}} .$$

There is no reliable measure of the bending rigidity of monolayer GO that we are aware of, so to estimate  $\kappa_{\text{b}}$  we start with that for pure graphene  $\kappa_{\text{b,graph}} = 1.2 \text{ eV}$  [125] and multiply this by the ratio of the 2D Young's Modulus of GO,  $E_{\text{GO}}^{2\text{D}} = 140 \text{ N/m}$  [126], to that of graphene,  $E_{\text{graph}}^{2\text{D}} = 340 \text{ N/m}$  [125], i.e.,  $\kappa_{\text{b}} = \kappa_{\text{b,graph}} E_{\text{GO}}^{2\text{D}} / E_{\text{graph}}^{2\text{D}} = 0.5 \text{ eV}$ . This yields  $\epsilon_{\text{CD}} = 14.8 k_{\text{B}} T$ . The approximate nature of this value is deemed acceptable as it is much larger than  $k_{\text{B}} T$ , and so only in competition with the sheet self-attraction  $\epsilon_{\text{LJ}}$ , which is taken as an unknown variable here. This model neglects the existence of kinks observed by Ref. [120]. Such sites of reduced bending energy, which can form lines of defects in GO, could very well induce preferential folding along these lines and contribute to an increased propensity for sheets to wrinkle instead of crumple.

### Appendix B: Calculation of folding energy barrier for a sheet

Here we calculate the energy required to fold a coarse-grained sheet similar to the one described in Sec. 3.2 along a sharp crease. The sheet has bead size  $\sigma$  and basis vectors  $\mathbf{e}_1 = (a, 0)$  (rows) and  $\mathbf{e}_2 = (0, \sqrt{3}a/2)$  (columns), where  $a = \sigma$  is the lattice vector of the sheet (Fig. 5.10a). If we fold along a row of particles, the bending energy per unit length along the crease is given by the cosine–delta potential

$$(5.18) \quad U_{\text{bend}} = \frac{3}{2a} \epsilon_{\text{CD}} [1 - \cos(\phi)] = \frac{3}{a} \epsilon_{\text{CD}} \sin^2(\phi/2) ,$$

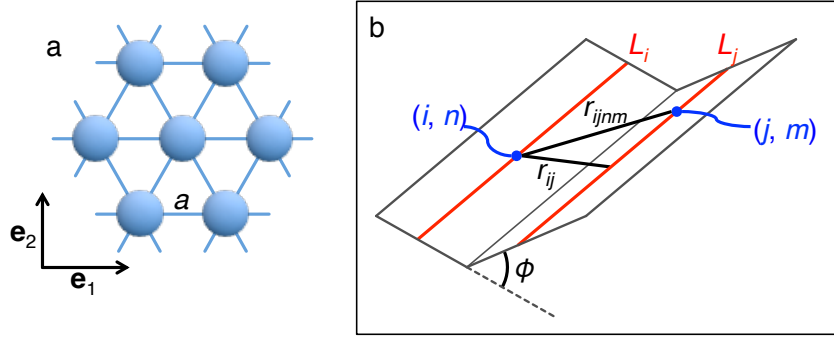


Figure 5.10. Schematics for the sheet–hinge bending calculation in Appendix B. (a) Sheet orientation with respect to lattice vectors  $\mathbf{e}_1$  and  $\mathbf{e}_2$ . Note that for simplicity, the calculation of the attractive LJ interactions are performed on a rectangular lattice with  $\mathbf{e}_1$  and  $\mathbf{e}_2$  as pictured. The sheet is folded along  $\mathbf{e}_1$ , and  $\mathbf{e}_2$  is perpendicular to the fold (b). Two particles  $(i, n)$  and  $(j, m)$  (blue dots) lie on lines  $L_i$  and  $L_j$  (red) that are a distance  $i|\mathbf{e}_2|$  and  $j|\mathbf{e}_2|$  away from the crease, respectively. The distance of closest approach of these two lines is  $r_{ij}$ , given by Eq. 5.20, and the distance between the two particles is  $r_{ijnm}$ , given by Eq. 5.19.

where  $\phi$  is the angle between surface normals on either side of the crease (see Fig. 5.10b), and a factor  $3/2$  has been included to account for the ratio between the bending energy of a single bond and that of the multiple bonds that straddle the crease along  $\mathbf{e}_1$  (see Fig. 5.10a). For mathematical simplicity, we calculate the LJ energy using a rectangular array of particles rather than a triangular array, and use basis vectors  $\mathbf{e}_1$  and  $\mathbf{e}_2$  as above to approximate the basis vectors of a triangulated sheet. We index each particle by the number of rows  $i$  it is from the crease and its column index  $n$  in the lateral direction (Fig. 5.10b). The distance between two atoms of index  $(i, n)$  and  $(j, m)$  that are on opposite sides of the crease is given by the folding angle  $\phi$  as

$$(5.19) \quad r_{ijnm}^2 = r_{ij}(\phi)^2 + a^2(n - m)^2 ,$$

where the angle-dependent distance of closest approach between two rows is given by

$$(5.20) \quad \left(\frac{r_{ij}}{a}\right)^2 = \frac{3}{4} [(i+j)^2 - 4ij \sin^2(\phi/2)] \equiv \left(\frac{x_{ij}}{\pi}\right)^2,$$

where  $x_{ij} \equiv \pi r_{ij}/a$  is introduced for convenience. For simplicity, we include only the attractive part of the LJ energy as in Eq. 5.7. The total LJ energy per unit length for two interacting rows  $i$  and  $j$  on opposite sides of the crease is

$$(5.21) \quad \frac{U_{ij}}{a} = \frac{1}{a} \sum_{n=-\infty}^{\infty} -\frac{4\epsilon_{\text{LJ}}\sigma^6}{r_{ijnm}^6} = -\frac{1}{a} \sum_{n=-\infty}^{\infty} \frac{4\epsilon_{\text{LJ}}\sigma^6/a^6}{[(x_{ij}/\pi)^2 + n^2]^3}$$

$$(5.22) \quad = \frac{2x_{ij}^3 \coth(x_{ij}) \operatorname{csch}^2(x_{ij}) + 3x_{ij}^2 \operatorname{csch}(x_{ij}) + 3x \coth(x_{ij}) 4\epsilon_{\text{LJ}}\pi^6\sigma^6}{8x_{ij}^6} \frac{1}{a^7}.$$

Since the minimum value taken by  $x_{ij}$ , given by  $i = j = 1$ , is  $x_{\min} = \pi\sqrt{3}$ , we can use to a high degree of precision the approximations  $\coth(x) \approx 1$  and  $\operatorname{csch}(x) \approx 0$  such that

$$(5.23) \quad \frac{U_{ij}}{a} \approx \kappa [(i+j)^2 - 4ij \sin^2(\phi/2)]^{-5/2}$$

$$(5.24) \quad = \frac{\kappa}{(i+j)^5} \left[ 1 + 10ij \left(\frac{\sin(\phi/2)}{i+j}\right)^2 + 70i^2j^2 \left(\frac{\sin(\phi/2)}{i+j}\right)^4 + \mathcal{O}(\phi^6) \right],$$

where  $\kappa \equiv -\frac{16\epsilon_{\text{LJ}}\pi a^6}{3^{3/2}a^7}$ , and we have expanded Eq. 5.23 around small  $\phi$  in to obtain Eq. 5.24.

The total attractive energy is obtained by summing over all pairs of rows  $(i, j)$

$$\begin{aligned}
 (5.25) \quad U_{\text{LJ}} &= \sum_{i,j=1}^{\infty} U_{ij} \\
 (5.26) \quad &\approx \kappa \left\{ \sum_{i,j=1}^{\infty} (i+j)^{-5} + 10 \sin^2(\phi/2) \sum_{i,j=1}^{\infty} ij(i+j)^{-7} \right. \\
 &\quad \left. + 70 \sin^4(\phi/2) \sum_{i,j=1}^{\infty} i^2 j^2 (i+j)^{-9} + \mathcal{O}(\phi^6) \right\} \\
 (5.27) \quad &\equiv \kappa [S_1 + 10S_2 \sin^2(\phi/2) + 70S_3 \sin^4(\phi/2) + \mathcal{O}(\phi^6)] ,
 \end{aligned}$$

where  $S_1 = -\zeta(5) + \pi^4/90 \approx 0.045$ ,  $S_2 = (21\pi^4 - 2\pi^6)/11340 \approx 0.011$ , and  $S_3 = (105\pi^4 - \pi^8)/283500 \approx 0.0026$ .

To fourth order in  $\phi$ , the total sheet-hinge energy  $U_{\text{SH}} = U_{\text{LJ}} + U_{\text{bend}}$  can be divided into three terms. The first order term,  $\kappa S_1$ , is independent of  $\phi$  and so has no effect on folding and can be disregarded. The second order term,  $(10\kappa S_2 + 3\epsilon_{\text{CD}}/a) \sin^2(\phi/2)$ , determines via its sign whether the flat phase is metastable or unstable, so that the critical self-attraction at which there is no kinetic barrier to sheet collapse is determined by setting this term to zero, yielding

$$(5.28) \quad \epsilon_{\text{LJ,crit}} = 2.8\epsilon_{\text{CD}} .$$

The third order term,  $70\kappa S_3 \sin^4(\phi/2)$ , competes with the second order term to determine the energetic barrier to folding when  $\epsilon_{\text{LJ}}$  is just below its critical value. Determining the energetic barrier to folding for small  $\epsilon_{\text{LJ}}$  requires taking Eq. 5.27 to higher order.

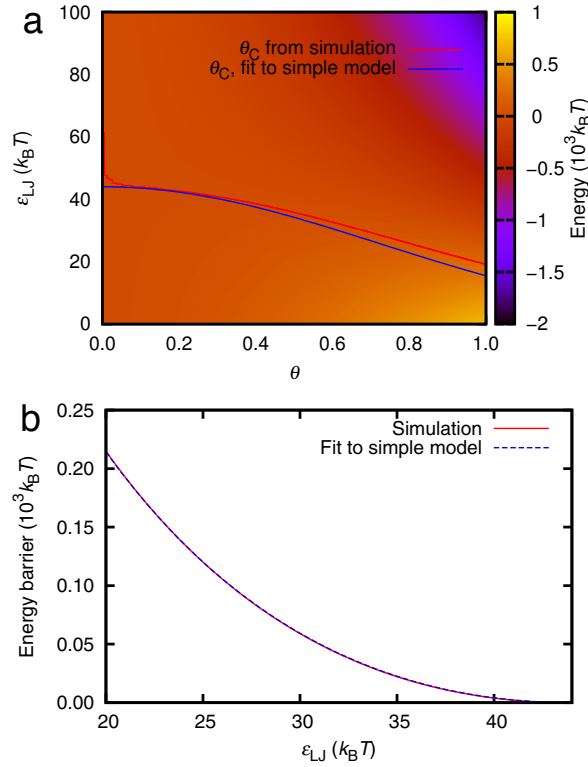


Figure 5.11. A simulated sheet is compared directly to the infinite sheet–hinge system. The energy landscape of a stiff sheet as a function of the bending angle and the self attraction shows how the critical bending angle  $\theta_C$  depends on the self-attraction  $\epsilon_{LJ}$  (a). The energy difference from a flat configuration at  $\theta_C$  is shown as a function of  $\epsilon_{LJ}$ , along with a fit to Eq. 5.9 via the parameters  $U_0$  and  $k$  (b). The simulation and fit show reasonable overlap, and the parameters obtained from the fit agree moderately well with those expected for the infinite sheet–hinge system (see text).

Because Eq. 5.27 is complicated, we seek to approximate it with a simplified expression. The similarity of the sheet–hinge and ball-and-stick models both in construction and behavior suggests the use of Eqs. 5.8 and 5.9. To test the fidelity of this approximation, we use LAMMPS to calculate  $U_{SH}$  for a finite sheet of  $L = 70\sigma$  and  $N = 5710$ , folded along  $\mathbf{e}_1$  at the middle of the sheet, with a Lennard-Jones potential potential of variable strength  $\epsilon_{LJ}$  and  $r_{cut} = \infty$ , and bending potential given by Eq. 5.2 (Fig. 5.11). A nonlinear least-

squares fit to the energetic barrier Eq. 5.9 as a function of the self-attraction yields  $U_0 = 3777k_B T$  and  $k = 0.112$ . Comparison with the bending energy of a fully folded sheet  $U_0 = 3108k_B T$  and the parameter  $k$  as calculated from Eq. 5.28,  $k = 0.118$ , shows reasonable agreement, with some difference resulting from the finite nature of the simulated sheet and the repulsive part of the LJ potential.

## CHAPTER 6

**Conclusion**

In this dissertation, I use particle-based simulations to understand system behavior, and in some cases to optimize system performance, primarily at surfaces of biomedical relevance. In these studies, systems are coarse-grained at the length-scale of interest, and the known rules governing individual particle motion are integrated numerically to obtain unexpected properties that can emerge on the population level due to nonlinear many-body effects. In all cases, the results are compared directly to theory and/or experiment to learn how subtle changes in particle properties can lead to larger changes in population behavior. Examples of this include the aggregation of bacteria on surfaces (Ch. 2) and aggregation of like-charged interfaces due to complex, multivalent counterions (Ch. 3). The latter study led to an exploration of ion current through such condensed, charged lamellae (Ch. 4), and inspired the study of the condensation of single self-attractive sheets in poor solvent (Ch. 5). Here I present a summary of the major findings and future outlook of each chapter of the dissertation.

In Chapter 2, I investigated the aggregation behavior of nascent bacterial colonies of surface-adhered *Pseudomonas aeruginosa*. By analyzing experimental data and comparing to an agent-based model, I found that individual bacteria can exhibit motilities that are distinct from one another even when these bacteria are genetically identical. These differences in motility correlated with the amount of time the bacteria remained fixed to the surface, suggesting that they may arise from heterogeneities in the number of type-IV

pili attached to a bacterium. This heterogeneity was then used to explain the power-law form of the surface-site visit distribution, which was previously suggested to be a hallmark of many-body behavior [16]. Bacterial aggregation was explored by allowing bacteria to deposit and interact with the polysaccharide Psl, which is a main component of the biofilm extracellular matrix and to which the bacteria are haptotactically attracted. Because of this attraction, Psl mediates a so-called self-attractive interaction, which I showed allows the population to divide into two distinct groups: “nucleators” that remain mostly stationary and nucleate Psl-rich surface regions, and “explorers” that are highly mobile, traveling between and linking the Psl beds created by the nucleators before settling into a sessile state. This division was observed in previous experiments [18]. Changing the relative prevalence of each subpopulation via the Psl deposition rate led to a trade-off between surface coverage, microcolony fortification, and microcolony heterogeneity, and suggested an all-around optimal Psl deposition rate in simulation, for which the surface coverage behavior, e.g., the visit histogram, mimicked experimental wild-type bacteria. Future work includes testing the hypothesis that the observed motility heterogeneity is related to the number of pili per bacterium, and developing methods to manipulate this bacterial economy as it develops to treat or control biofilms.

Another crucial interface for the transmission of infectious disease is the cell membrane. Certain proteins such as Rac1 are known to mediate the transport of viral agents into the cell to the detriment of the host, and their ejection from the cell membrane by the antiviral agent squalamine correlates with increased resistance to a range of important viral infections [41]. In chapter three, I used coarse-grained molecular dynamics simulations and free-energy perturbation and integration techniques to study how squalamine can displace

more highly charged proteins such as Rac1, thereby protecting the host cell. The ejection process was shown to arise from a combination of charge-density matching between squalamine and mammalian phospholipid membranes, the ability of multivalent, elongated counterions like squalamine to mediate an effective attraction between like-charged cellular membranes, and large differences in steric size between squalamine and Rac1. Specifically, the condensation of the membrane stacks by squalamine was sufficiently strong and tight to effectively squeeze the bulky Rac1 protein out of the condensed membrane stacks. This competitive interaction was recreated using a coarse-grained model employing only electrostatics and steric interactions, indicating that electrostatics are crucial to the ejection of Rac1 from membrane stacks. Future work may include hierarchical simulations that capture the squalamine–membrane and Rac1–membrane interactions in atomic or near-atomic detail.

Such condensed, charged layers exhibit many interesting properties. I use Poisson–Nernst–Planck theory (in collaboration with Dr. Niels Boon) and molecular dynamics simulations in chapter four to explore the ability of stacked graphene-oxide sheets to manipulate ionic current parallel to the sheet surfaces, in particular to enable ionic current rectification. I show that these negatively charged graphene-oxide stacks preferentially allow the passage of cations under an applied voltage. This leads to the development of concentration-polarization zones directly outside the stacked layers that can have extremely low local ion concentrations and so can dominate the total resistance of the system. Since the characteristics of these concentration-polarization zones are determined by system geometry, simple alterations of the geometry of the graphene-oxide stacks and the surrounding ion channels can generate a number of interesting transport effects including

current rectification. I used this understanding of system dynamics to suggest device optimization and a new device that may yield rectification without the use of graphene oxide, both of which require experimental testing as a next step.

The interactions that mediate attraction between sheets also mediate a self-attraction between different sites on the same sheet. In chapter five I use molecular dynamics and metadynamics simulations to elucidate the competition between sheet self-attraction and bending rigidity, and to determine how the final conformation of a graphene-oxide sheet depends on these parameters. In particular, the finite-range self-attraction of a coarse-grained sheet is shown to be able to overcome very large folding energy barriers. Additionally, the time-to-collapse of the sheets was shown to be well described by an Arrhenius relation to the barrier energy. Finally, large run-to-run variations of the final sheet conformations underscore the stochastic nature of the collapse. Sheets of all self-attractions formed either rod-like conformations after folding along a single axis, or wrinkled sheet-like structures after collapsing along multiple lines. Since larger sheets like that in experiment may be more likely to form multiple folds simultaneously, future work may include an analysis of the finite-size dependence of the final conformations of the sheets. Further, a model that incorporates defect lines that have been observed in real graphene-oxide sheets [120] may more provide a more faithful representation of experimental sheets.

## References

- [1] L. P. Kadanoff. More is the same; Phase transitions and mean field theories. *J. Stat. Phys.*, 137:777–797, 2009.
- [2] A. G. Moreira and R. R. Netz. Strong-coupling theory for counter-ion distributions. *Europhys. Lett.*, 52(6):705–711, 2000.
- [3] S. B. Carter. Principles of cell motility: The direction of cell movement and cancer invasion. *Nature*, 208(5016):1183–1187, 1965.
- [4] J. Adler. Chemotaxis in bacteria. *Science*, 153(3737):708–716, 1966.
- [5] M. Eisenbach, J. W. Lengeler, M. Varon, D. Gutnick, R. Meili, R. A. Firtel, J. E. Segall, G. E. Omann, A. Tamada, and F. Murakami. *Chemotaxis*. Imperial College Press, London, 2004.
- [6] J. Condeelis, R. H. Singer, and J. E. Segall. The great escape: When cancer cells hijack the genes for chemotaxis and motility. *Ann. Rev. Cell Dev. Bio.*, 21:695–718, 2005.
- [7] J. W. Costerton, P. S. Stewart, and E. P. Greenberg. Bacterial biofilms: A common cause of persistent infections. *Science*, 284(5418):1318–1322, May 21 1999.

- [8] T. Tolker-Nielsen, U. C. Brinch, P. C. Ragas, J. B. Andersen, C. S. Jacobsen, and S. Molin. Development and dynamics of *Pseudomonas* sp. biofilms. *J. Bact.*, 182(22):6482–6489, Nov 2000.
- [9] J. S. Mattick. Type IV pili and twitching motility. *Ann. Rev. Micro.*, 56(1):289–314, 2002.
- [10] L. Ma, Kara D. Jackson, R. M. Landry, M. R. Parsek, and D. J. Wozniak. Analysis of *Pseudomonas aeruginosa* conditional Psl variants reveals roles for the Psl polysaccharide in adhesion and maintaining biofilm structure postattachment. *J. Bact.*, 188(23):8213–8221, 2006.
- [11] M. S. Byrd, B. Pang, M. Mishra, W. E. Swords, and D. J. Wozniak. The *Pseudomonas aeruginosa* exopolysaccharide Psl facilitates surface adherence and NF- $\kappa$ B activation in A549 cells. *mBio*, 1(3):e00140–10, 2010.
- [12] D. E. Woodward, R. Tyson, M. R. Myerscough, J. D. Murray, E. O. Budrene, and H. C. Berg. Spatio-temporal patterns generated by *Salmonella typhimurium*. *Biophys. J.*, 68(5):2181–2189, May 1995.
- [13] E. O. Budrene and H. C. Berg. Dynamics of formation of symmetrical patterns by chemotactic bacteria. *Nature*, 376(6535):49–53, Jul 6 1995.
- [14] H. G. Othmer, K. J. Painter, D. Umulis, and C. Xue. The intersection of theory and application in elucidating pattern formation in developmental biology. *Math. Mod. Nat. Phen.*, 4(4):3–82, 2009.

- [15] C. Xie, H. Zhang, L. J. Shimkets, and O. A. Igoshin. Statistical image analysis reveals features affecting fates of *Myxococcus xanthus* developmental aggregates. *Proc. Natl. Acad. Sci. U.S.A.*, 108(14):5915–5920, Apr 5 2011.
- [16] K. Zhao, B. S. Tseng, B. Beckerman, F. Jin, M. L. Gibiansky, J. J. Harrison, E. Luijten, M. R. Parsek, and G. C. L. Wong. Psl trails guide exploration and microcolony formation in *Pseudomonas aeruginosa* biofilms. *Nature*, 497(7449):388–391, May 2013.
- [17] J. C. Crocker and D. G. Grier. Methods of digital video microscopy for colloidal studies. *J. Colloid Interface Sci.*, 179(1):298–310, Apr 15 1996.
- [18] M. L. Gibiansky, J. C. Conrad, F. Jin, V. D. Gordon, D. A. Motto, M. A. Mathewson, W. G. Stopka, D. C. Zelasko, J. D. Shrout, and G. C. L. Wong. Bacteria use type IV pili to walk upright and detach from surfaces. *Science*, 330(6001):197, 2010.
- [19] W. H. Press, S. A. Teukolsky, W. T. Vetterling, and B. P. Flannery. *Numerical Recipes in C: The Art of Scientific Computing*. Cambridge University Press, Cambridge, 2nd edition, 1992.
- [20] J. C. Conrad, M. L. Gibiansky, F. Jin, V. D. Gordon, D. A. Motto, M. A. Mathewson, W. G. Stopka, D. C. Zelasko, J. D. Shrout, and G. C. L. Wong. Flagella and pili-mediated near-surface single-cell motility mechanisms in *P. aeruginosa*. *Biophys. J.*, 100(7):1608–1616, APR 6 2011.

- [21] F. Jin, J. C. Conrad, M. L. Gibiansky, and G. C. L. Wong. Bacteria use type-IV pili to slingshot on surfaces. *Proc. Natl. Acad. Sci. U.S.A.*, 108(31):12617–12622, AUG 2 2011.
- [22] H. G. Othmer and A. Stevens. Aggregation, blowup, and collapse: The ABC’s of taxis in reinforced random walks. *SIAM J. Appl. Math.*, 57(4):1044–1081, Aug 1997.
- [23] B. Davis. Reinforced random walk. *Prob. Theor. Rel. Fields*, 84(2):203–229, 1990.
- [24] D. Horstmann. From 1970 until present: The Keller-Segel model in chemotaxis and its consequences. I. *Jahr. Deutschen Math. Ver.*, 105(3):103–165, 2003.
- [25] T. Hillen and K. J. Painter. A user’s guide to PDE models for chemotaxis. *J. Math. Biol.*, 58(1-2):183–217, Jan 2009.
- [26] B. R. Kulasekara, C. Kamischke, H. D. Kulasekara, M. Christen, P. A. Wiggins, and S. I. Miller. c-di-GMP heterogeneity is generated by the chemotaxis machinery to regulate flagellar motility. *eLife*, 2:e01402, 2013.
- [27] J. Sander, M. Ester, H. P. Kriegel, and X.W. Xu. Density-based clustering in spatial databases: The algorithm GDBSCAN and its applications. *Data Min. Knowl. Disc.*, 2(2):169–194, Jun 1998.
- [28] C. B. Whitchurch, T. Tolker-Nielsen, P. C. Ragas, and J. S. Mattick. Extracellular DNA required for bacterial biofilm formation. *Science*, 295(5559):1487, 2002.

- [29] L. Ma, H. Lu, A. Sprinkle, M. R. Parsek, and D. J. Wozniak. Pseudomonas aeruginosa Psl is a galactose- and mannose-rich exopolysaccharide. *J. Bact.*, 189(22):8353–8356, NOV 2007.
- [30] K. Sauer, A. K. Camper, G. D. Ehrlich, J. W. Costerton, and D. G. Davies. Pseudomonas aeruginosa displays multiple phenotypes during development as a biofilm. *J. Bact.*, 184(4):1140–1154, Feb 2002.
- [31] J. L. Connell, A. K. Wessel, M. R. Parsek, A. D. Ellington, M. Whiteley, and J. B. Shear. Probing prokaryotic social behaviors with bacterial “lobster traps”. *mBio*, 1(4):e00202–10, SEP-OCT 2010.
- [32] B. L. Bassler and M. B. Miller. Quorum sensing. In E. Rosenberg, E. F. DeLong, S. Lory, E. Stackebrandt, and F. Thompson, editors, *The Prokaryotes: Prokaryotic Communities and Ecophysiology*, chapter 22, pages 495–509. Springer, Berlin, 4th edition, 2013.
- [33] Y. Liu and K. M. Passino. Biomimicry of social foraging bacteria for distributed optimization: Models, principles, and emergent behaviors. *J. Opt. Theor. App.*, 115(3):603–628, Dec 2002.
- [34] I. W. Sutherland. The biofilm matrix – an immobilized but dynamic microbial environment. *Trends Microbiol.*, 9(5):222 – 227, 2001.

- [35] B. R. Boles, M. Thoendel, and P. K. Singh. Self-generated diversity produces “insurance effects” in biofilm communities. *Proc. Natl. Acad. Sci. U.S.A.*, 101(47):16630–16635, Nov 23 2004.
- [36] L. Jost. Entropy and diversity. *Oikos*, 113(2):363–375, 2006.
- [37] W. R. Young, A. J. Roberts, and G. Stuhne. Reproductive pair correlations and the clustering of organisms. *Nature*, 412(6844):328–331, Jul 19 2001.
- [38] B. Houchmandzadeh. The remarkable discreteness of being. *J. Biosci.*, 38:1–10, 2013.
- [39] K. S. Moore, S. Wehrli, H. Roder, M. Rogers, J. N. Forrest, D. Mccrimmon, and M. Zasloff. Squalamine: An aminosterol antibiotic from the shark. *Proc. Natl. Acad. Sci. U.S.A.*, 90:1354–1358, Feb 15 1993.
- [40] S. L. Wehrli, K. S. Moore, H. Roder, S. Durell, and M. Zasloff. Structure of the novel steroidal antibiotic squalamine determined by two-dimensional NMR spectroscopy. *Steroids*, 58:370–378, AUG 1993 1993.
- [41] M. Zasloff, A. P. Adams, B. Beckerman, A. Campbell, Z. Han, E. Luijten, I. Meza, J. Julander, A. Mishra, W. Qu, J. M. Taylor, S. C. Weaver, and G. C. L. Wong. Squalamine as a broad-spectrum systemic antiviral agent with therapeutic potential. *Proc. Natl. Acad. Sci. U.S.A.*, 108:15978–15983, SEP 20 2011.

- [42] T. Yeung, G. E. Gilbert, J. Shi, J. Silvius, A. Kapus, and S. Grinstein. Membrane phosphatidylserine regulates surface charge and protein localization. *Science*, 319:210–213, JAN 11 2008 2008.
- [43] A. Sumioka, D. Yan, and S. Tomita. TARP phosphorylation regulates synaptic AMPA receptors through lipid bilayers. *Neuron*, 66:755–767, JUN 10 2010 2010.
- [44] R. T. Alexander, V. Jaumouille, T. Yeung, W. Furuya, I. Peltekova, A. Boucher, M. Zasloff, J. Orłowski, and S. Grinstein. Membrane surface charge dictates the structure and function of the epithelial  $\text{Na}^+/\text{H}^+$  exchanger. *EMBO*, 30:679–691, FEB 16 2011 2011.
- [45] L. Pelkmans, E. Fava, H. Grabner, M. Hannus, B. Habermann, E. Krausz, and M. Zerial. Genome-wide analysis of human kinases in clathrin- and caveolae/raft-mediated endocytosis. *Nature*, 436:78–86, JUL 7 2005 2005.
- [46] L. Pelkmans and A. Helenius. Insider information: what viruses tell us about endocytosis. *Curr. Opin. Cell Biol.*, 15:414–422, AUG 2003 2003.
- [47] T. Ahola, A. Lampio, P. Auvinen, and L. Kaariainen. Semliki Forest virus mRNA capping enzyme requires association with anionic membrane phospholipids for activity. *EMBO*, 18:3164–3172, JUN 1 1999 1999.

- [48] V. Chukkapalli, I. B. Hogue, V. Boyko, W. Hu, and A. Ono. Interaction between the human immunodeficiency virus type 1 Gag matrix domain and phosphatidylinositol-(4,5)-bisphosphate is essential for efficient Gag membrane binding. *J. Virol.*, 82:2405–2417, MAR 2008 2008.
- [49] V. Chukkapalli, S. J. Oh, and A. Ono. Opposing mechanisms involving RNA and lipids regulate HIV-1 Gag membrane binding through the highly basic region of the matrix domain. *Proc. Natl. Acad. Sci. U.S.A.*, 107:1600–1605, JAN 26 2010 2010.
- [50] E. Stansell, R. Apkarian, S. Haubova, W. E. Diehl, E. M. Tytler, and E. Hunter. Basic residues in the Mason-Pfizer monkey virus gag matrix domain regulate intracellular trafficking and capsid-membrane interactions. *J. Virol.*, 81:8977–8988, SEP 2007 2007.
- [51] A. Agirre, A. Barco, L. Carrasco, and J. L. Nieva. Viroporin-mediated membrane permeabilization: Pore formation by nonstructural poliovirus 2B protein. *J. Biol. Chem.*, 277:40434–40441, OCT 25 2002 2002.
- [52] J. E. Vance and R. Steenbergen. Metabolism and functions of phosphatidylserine. *Prog. Lip. Research*, 44:207–234, JUL 2005 2005.
- [53] I. Borukhov, D. Andelman, and H. Orland. Steric effects in electrolytes: A modified Poisson-Boltzmann equation. *Phys. Rev. Lett.*, 79(3):435–438, JUL 21 1997.
- [54] Y. Burak and D. Andelman. Discrete aqueous solvent effects and possible attractive forces. *J. Chem. Phys.*, 114(7):3271–3283, FEB 15 2001.

- [55] Y. Levin. Electrostatic correlations: from plasma to biology. *Rep. Prog. Phys.*, 65:1577–1632, 2002.
- [56] A. G. Moreira and R. R. Netz. Binding of similarly charged plates with counterions only. *Phys. Rev. Lett.*, 87(7):078301, AUG 13 2001.
- [57] Y. W. Kim, J. Yi, and P. A. Pincus. Attractions between like-charged surfaces with dumbbell-shaped counterions. *Phys. Rev. Lett.*, 101(20):208305, NOV 14 2008.
- [58] S. Plimpton. Fast parallel algorithms for short-range molecular dynamics. *J. Comp. Phys.*, 117(1):1–19, 1995.
- [59] A. J. Ridley, H. F. Paterson, C. L. Johnston, D. Diekmann, and A. Hall. The small GTP-binding protein rac regulates growth-factor induced membrane ruffling. *Cell*, 70:401–410, AUG 7 1992 1992.
- [60] B. Borm, R. P. Reuquardt, V. Herzog, and G. Kirfel. Membrane ruffles in cell migration: Indicators of inefficient lamellipodia adhesion and compartments of actin filament reorganization. *Exp. Cell Research*, 302(1):83–95, Jan 1 2005.
- [61] A. Arkhipov, P. L. Freddolino, and K. Schulten. Stability and dynamics of virus capsids described by coarse-grained modeling. *Structure*, 14(12):1767–1777, 2006.
- [62] A. Arkhipov, Y. Yin, and K. Schulten. Four-scale description of membrane sculpting by BAR domains. *Biophys. J.*, 95(6):2806–2821, SEP 15 2008.

- [63] R. Modha, L. J. Campbell, D. Nietlispach, H. R. Buhecha, D. Owen, and H. R. Mott. The Rac1 polybasic region is required for interaction with its effector PRK1. *J. Biol. Chem.*, 283(3):1492–1500, JAN 18 2008.
- [64] E. R. Jack, J. Madine, L. Lian, and D. A. Middleton. Membrane interactions of peptides representing the polybasic regions of three Rho GTPases are sensitive to the distribution of arginine and lysine residues. *Mol. Mem. Biol.*, 25(1):14–22, 2008.
- [65] R. W. Hockney and J. W. Eastwood. *Computer Simulation Using Particles*. IOP Publishing, Bristol, 1988.
- [66] M. J. Stevens and K. Kremer. The nature of flexible linear polyelectrolytes in salt free solution: A molecular dynamics study. *J. Chem. Phys.*, 103:1669–1690, 1995.
- [67] H. J. C. Berendsen, J. P. M. Postma, W. F. van Gunsteren, A. DiNola, and J. R. Haak. Molecular dynamics with coupling to an external bath. *J. Chem. Phys.*, 81(8):3684–3690, 1984.
- [68] B. Widom. Structure of interfaces from uniformity of the chemical potential. *J. Stat. Phys.*, 19(6):563–574, 1978.
- [69] J. P. Valleau, L. K. Cohen, and D. N. Card. Primitive model electrolytes. II. The symmetrical electrolyte. *J. Chem. Phys.*, 72:5942–5954, 1980.
- [70] C. Guáqueta, L. K. Sanders, G. C. L. Wong, and E. Luijten. The effect of salt on self-assembled actin–lysozyme complexes. *Biophys. J.*, 90:4630–4638, 2006.

- [71] J. G. Kirkwood. Statistical mechanics of fluid mixtures. *J. Chem. Phys.*, 3(5):300–313, MAY 1935.
- [72] M. Mezei. Direct calculation of excess free energy of the dense Lennard-Jones fluid. *Mol. Simul.*, 2(3):201–207, 1989.
- [73] G. J. Rocklin, D. L. Mobley, K. A. Dill, and P. H. Hünenberger. Calculating the binding free energies of charged species based on explicit-solvent simulations employing lattice-sum methods: An accurate correction scheme for electrostatic finite-size effects. *J. Chem. Phys.*, 139:184103, 2013.
- [74] J. J. Kasianowicz, E. Brandin, D. Branton, and D. W. Deamer. Characterization of individual polynucleotide molecules using a membrane channel. *Proc. Natl. Acad. Sci. U.S.A.*, 93(24):13770–13773, 1996.
- [75] C. C. Harrell, Y. Choi, L. P. Horne, L. A. Baker, Z. S. Siwy, and C. R. Martin. Resistive-pulse DNA detection with a conical nanopore sensor. *Langmuir*, 22:10837–10843, 2006.
- [76] B. Hille. *Ion Channels of Excitable Membranes, 3rd Edition*. Sinauer, Sunderland, MA, 2001.
- [77] L. Cheng and L. J. Guo. Nanofluidic diodes. *Chem. Soc. Rev.*, 39(3):923–938, 2010.
- [78] J. Jung, P. Joshi, L. Petrossian, T. J. Thornton, and J. D. Posner. Electromigration current rectification in a cylindrical nanopore due to asymmetric concentration polarization. *Anal. Chem.*, 81:3128–3133, 2009.

- [79] D. Hlushkou, J. M. Perry, S. C. Jacobson, and U. Tallarek. Propagating concentration polarization and ionic current rectification in a nanochannel–nanofunnel device. *Anal. Chem.*, 84:267–274, 2012.
- [80] Z. Siwy, P. Apel, D. Baur, D. D. Dobrev, Y. E. Korchev, R. Neumann, R. Spohr, C. Trautmann, and K. Voss. Preparation of synthetic nanopores with transport properties analogous to biological channels. *Surf. Sci.*, 532–535:1061–1066, 2003.
- [81] R. Karnik, C. Duan, K. Castelino, H. Daiguji, and A. Majumdar. Rectification of ionic current in a nanofluidic diode. *Nano Letters*, 7(3):547–551, 2007.
- [82] L. Cheng and L. J. Guo. Ionic current rectification, breakdown, and switching in heterogeneous oxide nanofluidic devices. *ACS Nano*, 3(3):575–584, 2009.
- [83] J. Gao, A. R. Koltanow, K. Raidongia, B. Beckerman, N. Boon, E. Luijten, M. Olvera de la Cruz, and J. Huang. Kirigami nanofluidics. In preparation.
- [84] C. Yeh, K. Raidongia, J. Shao, Q. Yang, and J. Huang. On the origin of the stability of graphene oxide membranes in water. *Nature Chem.*, 7(2):166–170, 2015.
- [85] K. Raidongia and J. Huang. Nanofluidic ion transport through reconstructed layered materials. *J. Am. Chem. Soc.*, 134(40):16528–16531, 2012.
- [86] M. Miansari, J. R. Friend, P. Banerjee, M. Majumder, and L. Y. Yeo. Graphene-based planar nanofluidic rectifiers. *J. Phys. Chem. C*, 118(38):21856–21865, 2014.

- [87] S. T. Martin, A. Neild, and M. Majumder. Graphene-based ion rectifier using macroscale geometric asymmetry. *APL Mat.*, 2(9):092803, 2014.
- [88] J. Cervera, B. Scheidt, and P. Ramirez. A Poisson/Nernst-Planck model for ionic transport through synthetic conical nanopores. *Europhys. Lett.*, 71(1):35–41, 2005.
- [89] L. Cheng and L. J. Guo. Rectified ion transport through concentration gradient in homogeneous silica nanochannels. *Nano Letters*, 7(10):3165–3171, 2007.
- [90] R. Chein and B. Chung. Numerical study of ionic current rectification through non-uniformly charged micro/nanochannel systems. *J. Appl. Electrochem.*, 43:1197–1206, 2013.
- [91] Y. Green, S. Shloush, and G. Yossifon. Effect of geometry on concentration polarization in realistic heterogeneous permselective systems. *Phys. Rev. E*, 89:043015, 2014.
- [92] Y. Green and G. Yossifon. Time-dependent ion transport in heterogeneous permselective systems. *Phys. Rev. E*, 91:063001, 2015.
- [93] N. Boon and M. Olvera de la Cruz. ‘soft’ amplifier circuits based on field-effect ionic resistors. *Soft Matt.*, 11:4793–4798, 2015.
- [94] M. Tagliazucchi and I. Szleifer. Salt pumping by voltage-gated nanochannels. *J. Phys. Chem. Lett.*, 6:3534–3539, 2015.

- [95] M. Miansari, J. R. Friend, and L. Y. Yeo. Enhanced ion current rectification in 2d graphene-based nanofluidic devices. *Adv. Sci.*, 2(6):1500062, 2015.
- [96] A. Mani, T. A. Zangle, and J. G. Santiago. On the propagation of concentration polarization from microchannel–nanochannel interfaces part I: Analytical model and characteristic analysis. *Langmuir*, 25(6):3898–3908, 2009.
- [97] I. Rubinstein and L. Shtilman. Voltage against current curves of cation exchange membranes. *J. Chem. Soc., Faraday Trans. 2*, 75(2):231–246, 1979.
- [98] F. Maletzki, H. W. Rosler, and E. Staude. Ion transfer across electro dialysis membranes in the overlimiting current range: Stationary voltage current characteristics and current noise power spectra under different conditions of free convection. *J. Mem. Sci.*, 71(1–2):105–115, 1992.
- [99] N. A. Mishchuk, L. L. Lysenko, T. A. Nesmeyanova, and N. O. Barinova. Non-stationary processes in an ion-exchange membranes–diaphragm–ion-exchange resin system. 1. Concentration polarization. *Colloid J.*, 75(6):677–689, 2013.
- [100] I. Rubinstein and B. Zaltzman. Dynamics of extended space charge in concentration polarization. *Phys. Rev. E*, 81:061502, 2010.
- [101] I. Rubinshtein, B. Zaltzman, J. Pretz, and C. Linder. Experimental verification of the electroosmotic mechanism of overlimiting conductance through a cation exchange electro dialysis membrane. *Russian J. Electrochem.*, 38(8):853–863, 2002.

- [102] W. M. Haynes. *CRC Handbook of Chemistry and Physics, 93rd Edition*. CRC Press, Boca Raton, 2012.
- [103] W. S. Hummers, Jr. and R. E. Offeman. Preparation of graphitic oxide. *J. Am. Chem. Soc.*, 80(6):1339, 1958.
- [104] S. Eigler, S. Grimm, M. Enzelberger-Helm, P. Müller, and A. Hirsch. Graphene oxide: Efficiency of reducing agents. *Chem. Commun.*, 49:7391–7393, 2013.
- [105] C. Gómez-Navarro, R. T. Weitz, A. M. Bittner, M. Scolari, A. Mews, M. Burghard, and K. Kern. Electronic transport properties of individual chemically reduced graphene oxide sheets. *Nano Letters*, 7(11):3499–3503, 2007.
- [106] L. Wu, L. Liu, B. Gao, R. Muñoz-Carpena, M. Zhang, H. Chen, Z. Zhou, and H. Wang. Aggregation kinetics of graphene oxides in aqueous solutions: Experiments, mechanisms, and modeling. *Langmuir*, 29(49):15174–15181, 2013.
- [107] I. Chowdhury, N. D. Mansukhani, L. M. Guiney, M. C. Hersam, and D. Bouchard. Aggregation and stability of reduced graphene oxide: Complex roles of divalent cations, pH, and natural organic matter. *Environ. Sci. Tech.*, 49(18):10886–10893, 2015.
- [108] J. Luo, H. D. Jang, T. Sun, L. Xiao, Z. He, A. P. Katsoulidis, M. G. Kanatzidis, J. M. Gibson, and J. Huang. Compression and aggregation-resistant particles of crumpled soft sheets. *ACS Nano*, 5(11):8943–8949, 2011.

- [109] J. Luo, H. D. Jang, and J. Huang. Effect of sheet morphology on the scalability of graphene-based ultracapacitors. *ACS Nano*, 7(2):1464–1471, 2013.
- [110] Y. Jiang, W. N. Wang, D. Liu, Y. Nie, W. Li, J. Wu, F. Zhang, P. Biswas, and J. D. Fortner. Engineered crumpled graphene oxide nanocomposite membrane assemblies for advanced water treatment processes. *Environ. Sci. Tech.*, 49:6846–6854, 2015.
- [111] X. Dou, A. R. Koltonow, X. He, H. D. Jang, Q. Wang, and Y.-W. Chung. Self-dispersed crumpled graphene balls in oil for friction and wear reduction. *Proc. Natl. Acad. Sci. U.S.A.*, 113(6):1528–1533, 2016.
- [112] J. Luo, X. Zhao, J. Wu, H. D. Jang, H. H. Kung, and J. Huang. Crumpled graphene-encapsulated Si nanoparticles for lithium ion battery anodes. *J. Phys. Chem. Lett.*, 3:1824–1829, 2012.
- [113] L. Xiao, J. Damien, J. Luo, H. D. Jang, J. Huang, and Z. He. Crumpled graphene particles for microbial fuel cell electrodes. *J. Pow. Sources*, 208:187–192, 2012.
- [114] X. Wen, C. W. Garland, T. Hwa, M. Kardar, E. Kokufuta, Y. Li, M. Orkisz, and T. Tanaka. Crumpled and collapsed conformations in graphite oxide membranes. *Nature*, 355:426–428, 1991.
- [115] M. S. Spector, E. Naranjo, S. Chirovolu, and J. A. Zasadzinski. Conformations of a tethered membrane: Crumpling in graphitic oxide? *Phys. Rev. Lett.*, 73(21):2867–2870, 1994.

- [116] T. Tallinen, J. A. Åström, P. Kekäläinen, and J. Timonen. Mechanical and thermal stability of adhesive membranes with nonzero bending rigidity. *Phys. Rev. Lett.*, 105:026103, 2010.
- [117] S. J. Knauert, J. F. Douglas, and F. W. Starr. Morphology and transport properties of two-dimensional sheet polymers. *Macromolecules*, 43:3438–3445, 2010.
- [118] A. Laio and M. Parrinello. Escaping free-energy minima. *Proc. Natl. Acad. Sci. U.S.A.*, 99(20):12562–12566, 2002.
- [119] G. Fiorin, M. L. Klein, and J. Hénin. Using collective variables to drive molecular dynamics simulations. *Mol. Phys.*, 111(22–23):3345–3362, 2013.
- [120] H. C. Schniepp, K. N. Kudin, J.-L. Li, R. K. Prud’homme, R. Car, D. A. Saville, and I. A. Aksay. Bending properties of single functionalized graphene sheets probed by atomic force microscopy. *ACS Nano*, 2(12):2577–2584, 2008.
- [121] M. J. McAllister, J.-L. Li, D. H. Adamson, H. C. Schniepp, A. A. Abdala, J. Liu, M. Herrera-Alonso, D. L. Milius, R. Car, R. K. Prud’homme, and I. A. Aksay. Single sheet functionalized graphene by oxidation and thermal expansion of graphite. *Chem. Mater.*, 19:4396–4404, 2007.
- [122] J. Kim, F. Kim, and J. Huang. Seeing graphene-based sheets. *Materials Today*, 13(3):28–38, 2010.

- [123] N. Yoshida, Y. Miyata, K. Doi, Y. Goto, Y. Nagao, R. Tero, and A. Hiraishi. Graphene oxide-dependent growth and self-aggregation into a hydrogel complex of exoelectrogenic bacteria. *Scient. Rep.*, 6:21867, 2016.
- [124] O. Y. Zhong-can and W. Helfrich. Instability and deformation of a spherical vesicle by pressure. *Phys. Rev. Lett.*, 59(21):2486–2488, 1987.
- [125] C. Lee, X. Wei, J. W. Kysar, and J. Hone. Measurement of the elastic properties and intrinsic strength of monolayer graphene. *Science*, 321:385–388, 2008.
- [126] J. W. Suk, R. D. Piner, J An, and R. S. Ruoff. Mechanical properties of monolayer graphene oxide. *ACS Nano*, 4(11):6557–6564, 2010.